

REPORT DOCUMENTATION PAGE			Form Approved OMB NO. 0704-0188		
<p>The public reporting burden for this collection of information is estimated to average 1 hour per response, including the time for reviewing instructions, searching existing data sources, gathering and maintaining the data needed, and completing and reviewing the collection of information. Send comments regarding this burden estimate or any other aspect of this collection of information, including suggestions for reducing this burden, to Washington Headquarters Services, Directorate for Information Operations and Reports, 1215 Jefferson Davis Highway, Suite 1204, Arlington VA, 22202-4302. Respondents should be aware that notwithstanding any other provision of law, no person shall be subject to any penalty for failing to comply with a collection of information if it does not display a currently valid OMB control number.</p> <p>PLEASE DO NOT RETURN YOUR FORM TO THE ABOVE ADDRESS.</p>					
1. REPORT DATE (DD-MM-YYYY) 02-07-2014		2. REPORT TYPE Ph.D. Dissertation		3. DATES COVERED (From - To) -	
4. TITLE AND SUBTITLE PIEZOELECTRIC RESONANCE ENHANCED MICROWAVE AND OPTOELECTRONIC INTERACTIVE DEVICES			5a. CONTRACT NUMBER W911NF-12-1-0082		
			5b. GRANT NUMBER		
			5c. PROGRAM ELEMENT NUMBER 206022		
6. AUTHORS Robert McIntosh			5d. PROJECT NUMBER		
			5e. TASK NUMBER		
			5f. WORK UNIT NUMBER		
7. PERFORMING ORGANIZATION NAMES AND ADDRESSES University of Texas at San Antonio One UTSA Circle San Antonio, TX 78249 -0603			8. PERFORMING ORGANIZATION REPORT NUMBER		
9. SPONSORING/MONITORING AGENCY NAME(S) AND ADDRESS (ES) U.S. Army Research Office P.O. Box 12211 Research Triangle Park, NC 27709-2211			10. SPONSOR/MONITOR'S ACRONYM(S) ARO		
			11. SPONSOR/MONITOR'S REPORT NUMBER(S) 60545-MS-REP.12		
12. DISTRIBUTION AVAILABILITY STATEMENT Approved for public release; distribution is unlimited.					
13. SUPPLEMENTARY NOTES The views, opinions and/or findings contained in this report are those of the author(s) and should not be construed as an official Department of the Army position, policy or decision, unless so designated by other documentation.					
14. ABSTRACT Electro-optic (EO) devices that modulate optical signals by electric fields are an integrative part of the photonics industry and device optimization is an important area of research. As applications move to large bandwidth and higher frequency, low electro-optic effects and the requirement for large dimension [2] become restrictive for microwave-optical devices. Both experimental and computational evaluations indicate that strain and polarization distribution have a significant impact on electromagnetic wave propagation resulting from a					
15. SUBJECT TERMS piezoelectric, microwave, optical, ferroelectric, interactive devices					
16. SECURITY CLASSIFICATION OF:			17. LIMITATION OF ABSTRACT UU	15. NUMBER OF PAGES	19a. NAME OF RESPONSIBLE PERSON Ruyan Guo
a. REPORT UU	b. ABSTRACT UU	c. THIS PAGE UU			19b. TELEPHONE NUMBER 210-458-7057

Report Title

PIEZOELECTRIC RESONANCE ENHANCED MICROWAVE AND OPTOELECTRONIC INTERACTIVE DEVICES

ABSTRACT

Electro-optic (EO) devices that modulate optical signals by electric fields are an integrative part of the photonics industry and device optimization is an important area of research. As applications move to large bandwidth and higher frequency, low electro-optic effects and the requirement for large dimension [2] become restrictive for microwave-optical devices. Both experimental and computational evaluations indicate that strain and polarization distribution have a significant impact on electromagnetic wave propagation resulting from a resonant structure; however, no systematic study or fundamental understandings are available. This dissertation research has been carried out to study and further develop the subject of piezoelectric resonance enhanced electro-acoustic-optic process, in order to improve the sensitivity and efficiency of electro-optic sensors and to explore novel applications. Many finite element models have been constructed for evaluating the mechanisms of the phenomena and the effectiveness of the device structure. The enhancement in transmission is found to be directly related to the strain-coupled local polarization. At piezoelectric resonance oscillating dipoles or local polarizations become periodic in the material and have the greatest impact on transmission. Results suggest that the induced charge distribution by a piezoelectric material at certain resonant frequencies is effective for aiding or impeding the transmission of a propagating wave. The behavior of both piezoelectric-defined (or intrinsic piezoelectric materials) and engineered periodic structures are reported. The piezoelectric response of the surface displacement of samples is investigated using an ultra-high frequency laser Doppler vibrometer. A two dimensional view of the surface is obtained and the surface displacement, velocity and acceleration are compared to the electro-optic response under the resonant condition. A study of the acousto-optic (AO) effect in a family of oxide crystals (including e.g., TiO_2 , ZnO , LiNbO_3 , and ferroelectric perovskites) has been conducted by the finite element analysis method. This study further serves to show the potential of optimizing devices through a consideration of their directional dependent parameters and resonant behavior. The acousto-optic figure of merit (FOM) as a function of the material's refractive index, density, effective AO coefficient and the velocity of the acoustic wave in the material, is also investigated. By examining the directional dependent velocity, acousto-optic coefficients, and refractive index, the acousto-optic FOM can be calculated and plotted in all directions revealing the optimal crystal orientation to maximize coupling between the optical and acoustic waves. A finite element model was developed to corroborate the improved interaction. The model examines the diffraction that occurs on the optical wave as it travels through an acousto-optic medium. The combined information gained from commercially available multiphysics-based modeling platforms is shown to be an effective means of predicating acousto-optic device functionality.

**PIEZOELECTRIC RESONANCE ENHANCED MICROWAVE AND
OPTOELECTRONIC INTERACTIVE DEVICES**

APPROVED BY SUPERVISING COMMITTEE:

Ruyan Guo, Ph.D., Chair

Amar S. Bhalla, Ph.D.

Youngjoong Joo, Ph.D.

Chonglin Chen, Ph.D.

Michael A. Miller, Ph.D.

Accepted: _____
Dean, Graduate School

Copyright 2013 Robert A. McIntosh
All Rights Reserved

DEDICATION

This dissertation is dedicated for my parents Richard and Kathleen McIntosh for their support and encouragement.

**PIEZOELECTRIC RESONANCE ENHANCED MICROWAVE AND
OPTOELECTRONIC INTERACTIVE DEVICES**

by

ROBERT MCINTOSH, M.S.

DISSERTATION
Presented to the Graduate Faculty of
The University of Texas at San Antonio
In Partial Fulfillment
Of the Requirements
For the Degree of

DOCTOR OF PHILOSOPHY IN ELECTRICAL ENGINEERING

THE UNIVERSITY OF TEXAS AT SAN ANTONIO
College of Engineering
Department of Electrical and Computer Engineering
May 2013

UMI Number: 3563204

All rights reserved

INFORMATION TO ALL USERS

The quality of this reproduction is dependent upon the quality of the copy submitted.

In the unlikely event that the author did not send a complete manuscript and there are missing pages, these will be noted. Also, if material had to be removed, a note will indicate the deletion.



UMI 3563204

Published by ProQuest LLC (2013). Copyright in the Dissertation held by the Author.

Microform Edition © ProQuest LLC.

All rights reserved. This work is protected against unauthorized copying under Title 17, United States Code



ProQuest LLC.
789 East Eisenhower Parkway
P.O. Box 1346
Ann Arbor, MI 48106 - 1346

ACKNOWLEDGEMENTS

I would like to thank my advisors Dr. Ruyan Guo and Dr. Amar Bhalla for their guidance and countless hours of patient explanations. I would also like to thank my other committee members Dr. Youngjoong Joo, Dr. Chonglin Chen, and Dr. Michael Miller for their kind assistance.

The following sections of this dissertation are from previously published materials:

- Section 4.2* R. McIntosh, C. Garcia, A. Bhalla, and R. Guo, "Periodically Poled Structure on Microwave Transmissions Evaluated by Scattering Parameters," *Integrated Ferroelectrics*, vol. **131**, pp. 219-29 (2011).
- Section 4.3* R. McIntosh, A. S. Bhalla, and R. Guo, "Simulation of enhanced optical transmission in piezoelectric materials," in *Advances and Applications in Electroceramics II*, John Wiley & Sons, Inc.: 55-64 (2011).
- Section 6* R. McIntosh, A. Bhalla, and R. Guo, "Finite element modeling of acousto-optic effect and optimization of the figure of merit," *Photonic Fiber and Crystal Devices: Advances in Materials and Innovations in Device Applications VI - Proceedings of SPIE*, pp. 849703(pp.12). doi:10.1117/12.956441 (2012).
- Appendix* R. McIntosh, A. Bhalla, and R. Guo, "Dielectric anisotropy of ferroelectric single crystals in microwave C-band by cavity vectorial perturbation method," *Advances in Electroceramic Materials II*, John Wiley & Sons, Inc.: 75-88 (2010).

The section on future work on plasmon interaction is based on discussion and valuable input from Dr. Michael Miller and Dr. Ruyan Guo.

This dissertation research has been financially supported by grants from NSF (ECCS-1002380), DoD-ARMY-ONR (#60545-RT-REP) and ONR (N000140810854).

This Doctoral Dissertation was produced in accordance with guidelines which permit the inclusion as part of the Doctoral Dissertation the text of an original paper, or papers, submitted for publication. The Doctoral Dissertation conforms to all other requirements explained in the "Guide for the Preparation of a Master's Thesis/Recital Document or Doctoral Dissertation at The University of Texas at San Antonio."

It is acceptable for this Doctoral Dissertation to include as chapters authentic copies of papers already published, provided these meet type size, margin, and legibility requirements. In such cases, connecting texts, which provide logical bridges between different manuscripts, are mandatory. Where the student is not the sole author of a manuscript, the student is required to make an explicit statement in the introductory material to that manuscript describing the student's contribution to the work and acknowledging the contribution of the other author(s). The signatures of the Supervising Committee which precede all other material in the Master's Thesis/Recital Document or Doctoral Dissertation attest to the accuracy of this statement.

May 2013

PIEZOELECTRIC RESONANCE ENHANCED MICROWAVE AND OPTOELECTRONIC INTERACTIVE DEVICES

Robert McIntosh, Ph.D.
The University of Texas at San Antonio, 2013

Supervising Professor: Ruyan Guo, Ph.D.

Electro-optic (EO) devices that modulate optical signals by electric fields are an integrative part of the photonics industry and device optimization is an important area of research. As applications move to large bandwidth and higher frequency, low electro-optic effects and the requirement for large dimension [2] become restrictive for microwave-optical devices. Both experimental and computational evaluations indicate that strain and polarization distribution have a significant impact on electromagnetic wave propagation resulting from a resonant structure; however, no systematic study or fundamental understandings are available.

This dissertation research has been carried out to study and further develop the subject of piezoelectric resonance enhanced electro-acoustic-optic process, in order to improve the sensitivity and efficiency of electro-optic sensors and to explore novel applications. Many finite element models have been constructed for evaluating the mechanisms of the phenomena and the effectiveness of the device structure. The enhancement in transmission is found to be directly related to the strain-coupled local polarization. At piezoelectric resonance oscillating dipoles or local polarizations become periodic in the material and have the greatest impact on transmission. Results suggest that the induced charge distribution by a piezoelectric material at certain resonant frequencies is effective for aiding or impeding the transmission of a propagating wave. The behavior of both piezoelectric-defined (or intrinsic piezoelectric materials) and engineered periodic structures are reported. The piezoelectric response of the surface displacement of

samples is investigated using an ultra-high frequency laser Doppler vibrometer. A two dimensional view of the surface is obtained and the surface displacement, velocity and acceleration are compared to the electro-optic response under the resonant condition. A study of the acousto-optic (AO) effect in a family of oxide crystals (including e.g., TiO_2 , ZnO , LiNbO_3 , and ferroelectric perovskites) has been conducted by the finite element analysis method. This study further serves to show the potential of optimizing devices through a consideration of their directional dependent parameters and resonant behavior. The acousto-optic figure of merit (FOM) as a function of the material's refractive index, density, effective AO coefficient and the velocity of the acoustic wave in the material, is also investigated. By examining the directional dependent velocity, acousto-optic coefficients, and refractive index, the acousto-optic FOM can be calculated and plotted in all directions revealing the optimal crystal orientation to maximize coupling between the optical and acoustic waves. A finite element model was developed to corroborate the improved interaction. The model examines the diffraction that occurs on the optical wave as it travels through an acousto-optic medium. The combined information gained from commercially available multiphysics-based modeling platforms is shown to be an effective means of predicating acousto-optic device functionality.

TABLE OF CONTENTS

ACKNOWLEDGEMENTS	iv
ABSTRACT	v
LIST OF TABLES	xi
LIST OF FIGURES	xiii
CHAPTER 1: INTRODUCTION	1
1.1 Significance of the Subject of Study	1
1.2 Scope of Dissertation	3
1.3 Organization of the Dissertation	3
CHAPTER 2: THEORY AND BACKGROUND	7
CHAPTER 3: PIEZORESONANCE EXPERIMENTS	12
3.1 Piezoelectricity	12
3.2 Crystal Optics	17
3.3 Senarmont Compensator Technique	21
3.4 Samples	26
3.5 Admittance Spectrum and Resonant Modes	27
3.6 Electro-optic Measurements	28
3.7 Optical Transmission	33
3.8 Summary	35
CHAPTER 4: PIEZORESONANCE FINITE ELEMENT ANALYSIS	37
4.1 Finite Element Analysis	37
4.2 Microwave Transmission in Periodic Ferroelectric Domain Structure	37
4.2.1 Resonator Surfaces Free From Metallization	42

4.2.2 Comparison of gradient and step polarization, surfaces free from metallization	45
4.2.3 Effect of the sequence of the polarization, surfaces free from metallization.....	47
4.2.4 Dielectric Waveguide with Top and Bottom Metallization	48
4.2.5 Polarization in line with wave propagation, surfaces free from metallization.....	49
4.2.6 Polarization parallel (with) and antiparallel (against) propagation, surfaces free from metallization.....	51
4.2.7 Summary	52
4.3 Frequency Domain Piezoelectric Model.....	53
4.3.1 The Sample	53
4.3.2 The Piezoelectric Model	54
4.3.3 Frequency Domain Optical Model.....	58
4.4 Frequency Domain Piezoelectric Model – High Aspect Ratio	65
4.4.1 Summary	69
4.5 Time Domain Piezoelectric model	70
4.6 Comparison of Bulk EOM's	74
4.6.1 Finite Element Model Comparing Modulator Types.....	76
4.7 Summary	80
CHAPTER 5: MECHANICAL VIBRATION MEASUREMENTS.....	81
5.1 Laser Vibrometry	81
5.2 Measurement Setup.....	86
5.3 Samples and Configuration.....	87
5.4 Surface Plot Results	89
5.5 High Frequency Displacement.....	92

5.6 Velocity and Acceleration	98
5.7 Summary	99
CHAPTER 6: ACOUSTO-OPTIC FIGURE OR MERIT OPTIMIZATION	101
6.1 Introduction.....	101
6.2 Importance	102
6.3 Recent Status	102
6.4 Approach.....	103
6.5 Results and Discussion	109
6.6 Summary	118
CHAPTER 7: FUTURE WORK	119
7.1 Introduction.....	119
7.1 Resonance Enhanced Electro-Optic Coefficient by means of a Microwave Cavity	120
7.3 Acousto-optic Metamaterials	122
7.3.1 Plasmonics	122
7.3.2 Metamaterials and Cloaking	122
7.3.3 Proposed Phonon-Plasmon Meta-Device	124
7.4 Summary	128
CHAPTER 8: CONCLUSION	130
APPENDIX.....	132
A.1 Abstract	132
A.2 Introduction.....	132
A.3 Experimental	135
A.4 Results and Discussion	139

A.4.1 Limitations of the Conventional Perturbation Method	139
A.4.2 Verification of NECVP Using Low Permittivity Materials.....	142
A.4.3 Anisotropic Dielectric Property Evaluation	145
A.4.4 NECVP Method for High Permittivity Ferroelectric Materials.....	150
A.4.5 Effect of Meshing on NECVP Measurement Results	151
A.5 Summary	154
REFERENCES	156
VITA	

LIST OF TABLES

Table 3.1 List of crystal point groups that allow for piezoelectricity	14
Table 3.2 Sample compositions, poling, configuration, and dimensions used in piezoelectric experiments	27
Table 3.3 Sample configurations and Symmetries used in piezoelectric experiments	27
Table 4.1 Electrical and mechanical material parameters of the samples	56
Table 4.2 Optical parameters for PZN-PT	61
Table 4.3 Sample electrical and mechanical material parameters from [20].....	65
Table 4.4 Comparison of the piezoelectric resonate frequencies: calculated using a formula and derived by finite element analysis	67
Table 4.5 Qualitative comparison of half-wave voltage and bandwidth of common electro-optic modulator types	74
Table 6.1 Elasto-optic coefficients – of unitless – Part A.....	103
Table 6.2 Elasto-optic coefficients – of unitless – Part B.....	104
Table 6.3 Elastic coefficients –of units of 10^{11} [N/m ²].....	104
Table 6.4 Piezoelectric coupling coefficients – of units of [C/m ²].....	104
Table 6.5 Relative dielectric permittivity coefficients – of unitless	104
Table 6.6 Refractive index coefficients and density – density of units of [kg/m ³].....	105
Table 6.7 Maxima of Figure of Merit for each material with associated property in the same direction. Theta and phi are in degrees.....	114

Table A.1 Summary of sample dimensions used in microwave measurement.....	137
Table A.2 Alumina complex permittivity measured by NECVP method near 4.01GHz (TE ₁₀₃) and 5.19 (TE ₁₀₅) GHz.....	143
Table A.3 Corning 0080 glass complex permittivity measured by NECVP method near 4.01GHz (TE ₁₀₃) and 5.19 (TE ₁₀₅) GHz	144
Table A.4 Corning 0080 glass complex permittivity measured by post resonant technique.....	144
Table A.5 Fused silica tube complex permittivity measured by NECVP method near 4.01GHz (TE ₁₀₃) and 5.19 (TE ₁₀₅) GHz	144
Table A.6 Complex permittivity of Pyrex glass rod measured by NECVP method near 4.01GHz (TE ₁₀₃) and 5.19 (TE ₁₀₅) GHz	145
Table A.7 Permittivity of Teflon rod measured by NECVP method near 4.01GHz (TE ₁₀₃) and 5.19 (TE ₁₀₅) GHz	145

LIST OF FIGURES

Figure 2.1 Permittivity and electro-optic response of crystals near resonance. Figure from [5]....	7
Figure 2.2 Comparison of experimental results of optical signal, phase angle and admittance for PZN-PT sample under electro-optic modulation	9
Figure 3.1 Admittance frequency spectrum of a typical piezoelectric resonator showing resonance and anti-resonant frequencies	15
Figure 3.2 Common equation simplifications for calculating the electric field induced Birefringence in an electro-optic modulator	21
Figure 3.3 Schematic of experiment based on Senarmont compensator technique.....	22
Figure 3.4 Transmittance curve (in blue) for applied DC field on sample in crossed polarizer configuration and effect of quarter wave plate on optical biasing for ac modulation around the 50% transmittance point	23
Figure 3.5 Orientation of applied field and optical propagation for transverse electro-optic modulator	25
Figure 3.6 Block diagram of electro-optic measurement setup	29
Figure 3.7 Electro-optic test configuration used for quartz samples (shaded areas are electroded)	30
Figure 3.8 Results of quartz electro-optic test showing measured electro-optic coefficient and admittance response	31
Figure 3.9 Quartz electro-optic test (from previous figure) zoomed in on largest resonance	32

Figure 3.10 Results of PMN-30%PT electro-optic test showing measured electro-optic voltage as measured at the photodiode and admittance response.....	33
Figure 3.11 Results of optical transmission test of PMN-30%PT under piezo-resonant ac bias using low fields ($< 50\text{V/cm}$).....	35
Figure 4.1 Periodically polarized antiparallel structure within a piezoelectric sample	40
Figure 4.2 Simulation setup for sample inserted in microwave waveguide showing electromagnetic wave excited on port 1 and travels to port 2 along the x-axis	41
Figure 4.3 Antiparallel step polarization configuration for 1-5 elements in microwave FEA model	42
Figure 4.4 Transmission parameter as function of frequency in 4 periodically polarization-inverted elements.....	43
Figure 4.5 Transmission parameter as function of frequency and the number of periodically polarization-inverted elements.....	44
Figure 4.6 A surface plot of the transversal electric field strength at 20GHz ($P = 0.1 \text{ nC/cm}^2$) that shows how the polarization-inverted sections tend to support transverse electric modes corresponding to the number of the elements.....	45
Figure 4.7 Gradient and step polarization in a 5 element cavity, both with magnitude 0.1 nC/cm^2	46
Figure 4.8 Comparison of sinusoidal and step polarization distribution in a polarization-inverted 5-element waveguide	46

Figure 4.9 FEA model setup showing periodic poling configuration. “P” corresponds to polarization in the positive z direction and “N” in the negative z direction	47
Figure 4.10 Transmission parameter as a function of frequency for 4 polarization-inverted elements while the order of antiparallel polarization can cause a significant shift in the response	48
Figure 4.11 Transmission parameter as a function of frequency for a number of periodically polarization-inverted elements while electrodes and polarization are perpendicular to the microwave propagation direction	49
Figure 4.12 FEA microwave model setup of antiparallel polarization in the direction of propagation (positive x-axis) and against propagation (negative x-axis).....	50
Figure 4.13 Transmission parameter as a function of frequency for a number of periodically polarization-inverted elements while polarization is parallel to the microwave propagation direction.....	50
Figure 4.14 Surface plots of the electric field strength at 20 GHz ($P_r = 0.1 \mu\text{C}/\text{cm}^2$, $P_r//x\text{-axis}$) for the number of polarization-inverted elements from 0 to 5, while polarization is parallel to the microwave propagation direction.	51
Figure 4.15 Transmission parameter as a function of frequency and magnitude of polarization for a single element with polarization parallel or antiparallel to the microwave propagation direction.....	52
Figure 4.16 PMN-30%PT sample, poled in [001] direction. Electroded on top and bottom {001} surfaces of the x by y dimensions	54

Figure 4.17 Simulation of Admittance magnitude $ Y $ in Siemens and the phase angle in degrees over frequency range encompassing the piezoelectric vibrational frequencies below 1 MHz.....	57
Figure 4.18 Comparison of the simulation and experimental results of the admittance frequency spectrum of PMN-30%PT	58
Figure 4.19 Illustration of the finite element optical model that includes two sub models to handle the coupling between piezoelectric and optical interaction	59
Figure 4.20 Simulation results of the optical plane wave propagating in the y direction and a plot of the electric field (E_z) in the transverse z direction.....	62
Figure 4.21 Simulation results of the frequency response of the optical response over a range of low frequency resonant modes showing strong correlation with the slope of the electrical admittance.....	63
Figure 4.22 Current density distribution in the sample; off piezoelectric resonance at 213 KHz (Left) and near piezoelectric resonance at 215 KHz (Right).....	64
Figure 4.23 Admittance frequency spectrum of typical piezoelectric resonator showing resonance and anti-resonance frequencies of fundamental and harmonics.....	66
Figure 4.24 Total displacement of simulated PMN-30%PT k_{31} bar at fundamental resonant frequency 38.750 KHz	67
Figure 4.25 Total displacement of simulated PMN-30%PT k_{31} bar at 2 nd harmonic of resonant frequency 115.250 KHz	68

Figure 4.26 Total displacement of simulated PMN-30%PT k_{31} bar at 3 rd harmonic of resonant frequency 189.750 KHz	69
Figure 5.1 Photo of PolyTec UHF-120 Vibrometer and measurement fixture.....	81
Figure 5.2 Heterodyne Interferometry configuration.....	83
Figure 5.3 Vibrometer measurement configuration.....	87
Figure 5.4 Multipoint measurement for two dimensional representation of sample surface using vibrometer test data.....	88
Figure 5.5 Surface displacement measurement by vibrometer gives amplitude of displacement while actual sample is periodically changing as per the applied sinusoidal field.....	89
Figure 5.6 Quartz (sample #2) comparison of COMSOL Simulation and vibrometer surface displacement	90
Figure 5.7 PMN-30%PT (sample #1) COMSOL simulation and vibrometer surface displacement	91
Figure 5.8 PMN-30%PT displacement plots at major resonant frequencies	92
Figure 5.9 Configuration for PMN-30%PT sample for electro-optic and vibrometer tests	94
Figure 5.10 PMN-30%PT electro-optic and vibrometer tests indicating that electro-optic enhancement persists in to the MHz region where sample strain is minimal	95
Figure 5.11 Full view of PMN-30%PT sample surface displacement.....	97
Figure 5.12 Vibrometer measurement of displacement, velocity, and acceleration of a PMN-30%PT sample	99
Figure 6.1 Conversion scheme of Cartesian coordinate system to spherical coordinates	106

Figure 6.2 Directional dependence of elasto-optic figure of merit M_2 calculated for several example materials representing different crystal systems	111
Figure 6.3 Relative acousto-optic figure of merit of Gallium Arsenide in Z_1 - Z_2 plane and comparison to the literature value reported in the [110] direction.....	113
Figure 6.4 A typical example of an acousto-optic modulator configuration	115
Figure 6.5 The setup of the piezoelectric and electromagnetic domains for the COMSOL FEA acousto-optic model	116
Figure 6.6 COMSOL simulation of the optical propagation from the top section (air) into the material and to the bottom port.....	117
Figure 7.1 Microwave cavity electro-optic measurement technique [44]	121
Figure 7.2 Proposed configuration for achieving piezo-resonance induced optical cloaking	124
Figure 7.3 Proposed surface acoustic wave device to launch wave and induce a periodic polarization	125
Figure 7.4 Proposed experiment setup for Phonon-Plasmon measurement	126
Figure 7.5 Finite Element Analysis setup for 2D SAW model.....	127
Figure 7.6 Simulation of the y dimension surface displacement and resulting polarization in a SAW device excited at 786 MHz.....	128
Figure A.1 Configuration and dimension of the microwave cavity used for the NECVP study	135
Figure A.2 Orientation of samples relative to microwave resonant cavity.....	136
Figure A.3 Finite element simulation of the perturbed cavity electric field (V/m), for TE_{103} mode near $f_c=4.003\text{GHz}$	138

Figure A.4 Comparison of calculated resonance frequency shift as function of dielectric permittivity, by FEA and by Equations (4) and (5).....	140
Figure A.5 Comparison of calculated resonance frequency shift as a function of dielectric permittivity, by FEA and by Equ. (9.4) and (9.5). The bar-shaped sample (2.7x2.96x4.69 mm ³) is PE positioned and with dimension shorter than the height of the cavity	141
Figure A.6 Perturbed electric field intensity profile in the microwave cavity of TE ₁₀₃ mode as a function of the real part of the permittivity for a PE center positioned sample (2.7x2.96x4.69 mm ³).....	142
Figure A.7 Schematics of the rotation fixture.....	147
Figure A.8 Actual configuration of the cavity perturbation setup with sample rotation	148
Figure A.9 Resonance frequency shift $(f_c - f_s)/f_s$ as function of rotation angle for a rectangular shaped alumina ceramic sample. Arrows indicate electric field directions	149
Figure A.10 Derived permittivity as a function of rotation angle for a rectangular shaped alumina ceramic bar, after correction of the dimensional variation	150
Figure A.11 Simulation result on the normalized shift of resonance frequency as function of $\log \epsilon'_r$. The relative permittivity of the prepoled PMN-30PT crystal in [110] direction was derived by comparing the measured value with the simulated frequency shift, using the NECVP method.....	152
Figure A.12 Simulation result on the normalized shift of resonance frequency as function of $\log \epsilon'_r$. The relative permittivity of the PZT-5H ceramic was derived by comparing the measured value with the simulated frequency shift, using the NECVP method ...	153

Figure A.13 Effect of Meshing, Mesh 1 being the finest.....	154
---	-----

CHAPTER 1: INTRODUCTION

1.1 Significance of the Subject of Study

This dissertation focuses on experimental determination of methods and systems for the enhancement of optical transmission by way of periodic structures. Both numerical simulation and theoretical explanation are incorporated to better guide the experimental setup and give improved understanding to resultant data. The outcome of this research could improve the overall efficiency of electro-optic (EO) devices. Higher EO coefficient at RF and microwave frequencies can lead to much better performance with reduced device size. Greater modulation depth also results in electro-optic modulators (EOM) with larger deflection angles. High EO coefficient means EOM's would require less power to perform the same function, more compact and more linear operation. While EOMs do not require much power individually, it is desirable, if not imperative, to reduce the energy consumption of devices for large-scale implementation. Additionally an emerging technology in the computer world is new processors which use optics; power efficiency is a great concern here especially when heat dissipation of new processors is a limiting factor. The knowledge gained through this dissertation research will help determine best design practices for better coupling of the EO effect and electromagnetic (EM) transmission. Additionally a better understanding will be gained on why resonance improves transmission and coupling, when it will occur, and how to control it. Finally this research will contribute to our understanding of effective experimental and modeling practices underlying multiphysics numerical methods.

There has been much work on acousto-optics and electro-optics but little on acousto-electro-optics [1]. There are few papers [1, 3, 4] addressing the enhanced EO coupling that occurs at resonance. There are very few examples of simulation/modeling of spontaneous

polarization in materials and, even more sparse, are examples of complex multiphysics models dealing with interactions between acoustics, piezoelectric, RF, EM wave and induced periodic polarization changes. An effort to model multi-physics interactions such as this might be considered in itself a significant research topic; the powerful combination of multiphysics modeling and advanced experiments has yet to be explored. There has been much work on imaging the surface of materials using techniques like profilometry and atomic force microscopy and some on imaging vibrating materials using vibrometry, but little work has been done imaging the surface while monitoring the optical transmission.

The interaction between light and piezoelectric materials is very important for optical communications. All transparent piezoelectric materials are also electro-optic and photoelastic. Photoelasticity can be expressed in terms of piezo-optic or elasto-optic effects. It has long been observed that the electro-optic output is strongly influenced by low frequency (kHz) vibrations due to natural piezoelectric resonate frequencies [5]. Typically electro-optic modulators are not operated in the region of resonance vibration to avoid non-monotonic responses; however it has been shown that operation at these frequencies and at harmonics can actually be advantageous to improve electro-optic response [4]. The response of the electro-optical signal tends to follow the slope of the magnitude of the electrical admittance as a function of frequency, this is fairly unsurprising as the largest mechanical vibrations occur at resonance (typically between the resonant and anti-resonant frequencies) and in turn cause a large change in refractive index. Further results by Guo *et al.* [1] have shown that certain resonance modes with vibrations mostly in the direction transverse to optical propagation have a larger influence on response because they are parallel to the optical polarization. Given that the spurious response of these crystals little attention has been made to the detailed study of their response in conjunction with the

optical field around resonance, leaving it an open and promising area of research for further optimization of electro-optic devices.

1.2 Scope of Dissertation

The goal of this dissertation research was to study and further develop the subject of piezoelectric resonance enhanced electro-acoustic-optic processes in order to improve the sensitivity and efficiency of electro-optic sensors and to explore novel applications. Both experimental study and numerical simulations are essential approaches to accomplish the goal.

1.3 Organization of the Dissertation

Following a comprehensive but selective review on the background of the research summarized in Chapter 2, electro-optic and electrical experiments performed to confirm the enhancement reported by previous researchers and to investigate its limits are described in Chapter 3. The standard method of crossed polarizers with a quarter wave plate for biasing (the Senarmont compensator technique) was used to measure the linear electro-optic Pockels effect in the test samples. The results confirmed a very large spike in the response close to the resonance that loosely correlates with the slope of the Admittance as discussed in [4].

To better understand this effect, how to control it, when it occurs, how to maximize it and to extend our ability to quickly test under different conditions, several models were constructed using Finite Element Analysis. The details of these models are discussed in Chapter 4. Section 4.2 describes in detail a model of the transmission of a microwave EM signal through a ferroelectric, periodically-poled sample. Several poling configurations are used to adjust the amplitude of the polarization as well as the number and direction of the domains. It is observed that there is a polarization threshold of about $1 \times 10^{-12} \text{ C/cm}^2$ needed to affect any change in transmission (in present simulation) and after that the polarization amplitude can have a

significant effect on transmission. The number of polarization elements can be adjusted to tune the transmission magnitude provided that the polarization directions are transverse to wave propagation. Longitudinal polarization in the same direction as the propagating wave does not show any significant influence on transmission which corroborates with [4]. A separate model was also developed to mimic the behavior of our experimental electro-optic tests. This model contains two sub models; the piezoelectric one and the optical one, both were examined with a time-harmonic (frequency domain) approach. The piezoelectric model is used to examine the resonant behaviors of a piezoelectric sample and the results from this model are coupled into the optical model. The optical model is used to test the amount of signal transmitted through the device during resonance. This model has been shown to accurately predict the increased transmission possible near resonance that is consistent with experimental methods. Additionally the model used a special coupling between the 3D piezoelectric and 2D optical portions to reduce the required computational power and made possible the simultaneous evaluation of a millimeter sized device with a propagating micrometer EM wave. This kind of multiphysics study is nearly impossible without the method derived and is rarely attempted. This model is also a useful tool for portraying the displacive current distribution near resonance. As proposed in [4] displacive current forms a complete circuit near resonance and leads to enhancement of the optical signal – the model has served to confirm this theory. In section 4.4 another model discussed and used to examine the experimental technique used by Johnson et al. [4, 6] using a dual signal approach with ac biasing near piezo-resonance. This model was simulated in the time domain rather than the frequency domain model discussed previously; this is because the time-harmonic solver only allows for a single excitation frequency. Using the time domain solver two signals can easily be added. This model does not examine the optical response but instead

calculates the piezoelectric response and the effect on the refractive index. The index change is appropriate for this study because it is proportional to the induced phase change in the optical signal. This model accurately shows a wide bandwidth enhancement of the index change when the ac biasing is set to a frequency near the material's piezo-resonant frequency. There have been many qualitative statements about the relative differences in half wave voltage that can be achieved with resonance and non-resonant electro-optic modulators, yet few examples offered a quantitative comparison. A finite element model is discussed in section 4.5 that compares a resonator's half wave voltage over a range of visible wavelengths. This type of comparison is used as it is more familiar to optical researchers. It was demonstrated that piezo-resonant modulators are significantly more efficient than even resonators assembled using an electrically resonant circuit. Furthermore piezo-resonators, as predicted by the model offer a half wave voltage that can be as much as 1000 times less than that of non-resonant modulators.

To better understand the transversal lattice strain associated with piezoelectric resonance modes that enhance the propagating optical signal several samples were studied in Chapter 5 with an ultra-high frequency Laser Doppler Vibrometer. This system enables high resolution measurements of the displacement, velocity, and acceleration of the vibrating sample at a given point. An array of tests were conducted over the surface of the sample to build up a full view of the modes on a given surface. Comparing these results to the optical response indicates that even in the megahertz regime where the sample becomes constrained and strain is minimal there are still spikes in the electro-optic response which is further evidence that enhancement is driven by more than high strains but perhaps a result of the periodically induced polarization that can still respond at those frequencies.

Chapter 6 extends the study to acousto-optic optimization in detail. This dissertation is about more than just piezo-resonance, it is in a more general sense about improved sensitivity of electro-optic devices. While electro-optic effect is predominant in the materials studied vibrations of lattices near resonance result in high strains that in turn affect the birefringence of a crystal through the acousto-optic effect. The best orientation for applying a field for a large index change was evaluated using the acousto-optic figure of merit resulting from a full set of data including the density, refractive index, piezoelectric constants, and elasticity of the material. Several common materials were evaluated and it was observed that the best orientation is not always along the principal axes.

The work discussed in and the knowledge gained through this dissertation has a broad range of potential applications and opened up possibilities for many new areas of research. Chapter 7 discusses proposed future research and the attempt to design a few possible experiments that may be used to investigate new applications for piezoelectric resonance enhancement. The main interest described is for an acoustic metamaterial for RF and microwave “cloaking”. Due to the fact that resonance can influence the EM transmission in a material it may be possible to make an opaque object, transparent (or vice versa). Because resonance can be excited, or turned on/off with the applied signal it may be uniquely suited for making a dynamically adjustable “cloak”. This chapter discusses a proposed research path to realize such a device. An Overall conclusion is given in Chapter 8 highlighting the main scientific and technical advancements this dissertation has been able to achieve. Additionally the Appendix contains a great deal of information on using Finite Element Analysis to calibrate a microwave waveguide; this technique can be useful for electro-optic evaluation and frequencies where lumped methods are no longer valid.

CHAPTER 2: THEORY AND BACKGROUND

One of the earliest examples of a significant change in the electro-optic coefficient was reported by Pisarevski *et al.* [5]. The two samples used in the experiment showed a drop in permittivity around 10 kHz. This drop in permittivity corresponds to a large increase and sudden decrease in the electro-optic coefficient in both crystals measured (See Figure 2.1).

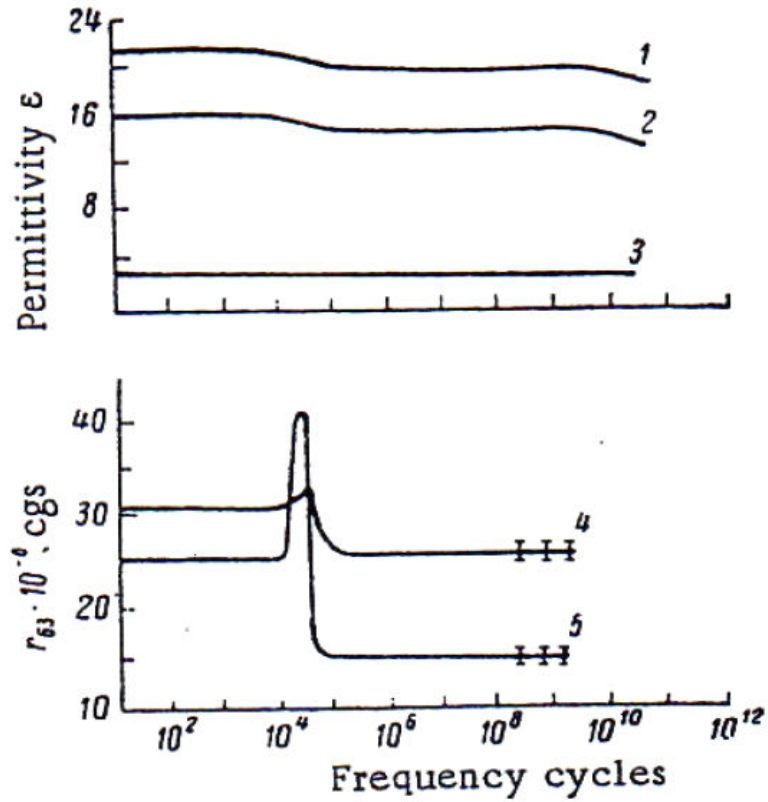


Figure 2.1 Permittivity and electro-optic response of crystals near resonance.
Figure from [5]

As examined by Johnson *et al.* [4, 6] the EO effect can be enhanced not only at resonance but continuously between resonance and several harmonics through a method of frequency mixing. Experiments were carried out at frequencies below the low MHz region using the Senarmont compensator technique. Two signals simultaneously applied to the sample, one at the

fundamental resonance mode of the sample and the other which is swept from well below resonance to well above it. The results which are given in terms of optical transmission (voltage monitored at the photodetector) show that certain resonance modes have enhanced optical transmission and furthermore that transmission is enhanced over a range of frequencies out to even the 5th harmonic of resonance. It is cited that though enhancement decreases after this point, it is likely due to the frequency limitations of the measurement devices; specifically, the lock-in amplifier.

It is not surprising that Johnson's experiment gave more optical transmission output as two signals used simultaneously, and presumably these signals used in phase such that, when equal, there was constructive interference and then, as the frequencies parted, there would be periodic constructive and destructive interference. But this interestingly was not what was measured by Johnson at the photodetector. In experiments that involve one signal of constant amplitude and changing frequency the electro-optic coefficient is certainly proportional to the optical transmission at the photodetector. However, due to the frequency mixing technique used by Johnson, this is no longer the case. It would be more appropriate to monitor both the rms signal at the sample and at the photodetector and take the ratio of the two which will then be proportional to the EO coefficient. It is likely that the results will still show an improved EO coupling at the piezoresonance harmonics, but perhaps not as profound an enhancement as previously reported.

The most recent study on enhanced piezoresonance optical transmission by Guo *et. al.* [1] was done on PZN-8PT crystal. This study was done on the fundamental resonant modes d_{33} , d_{31} , d_{32} and it was found that the optical transmission increased near the d_{33} and d_{31} modes where the strain is transverse to the propagation of light (See Figure 2.2). The d_{32} mode did not produce

transmission as its strain was parallel to optical transmission. The authors cite that the effective EO coefficient is largest when there is a large change in electrical admittance with frequency.

$$r_{eff}(\omega) \propto \frac{dY(\omega)}{d\omega} \quad (2.1)$$

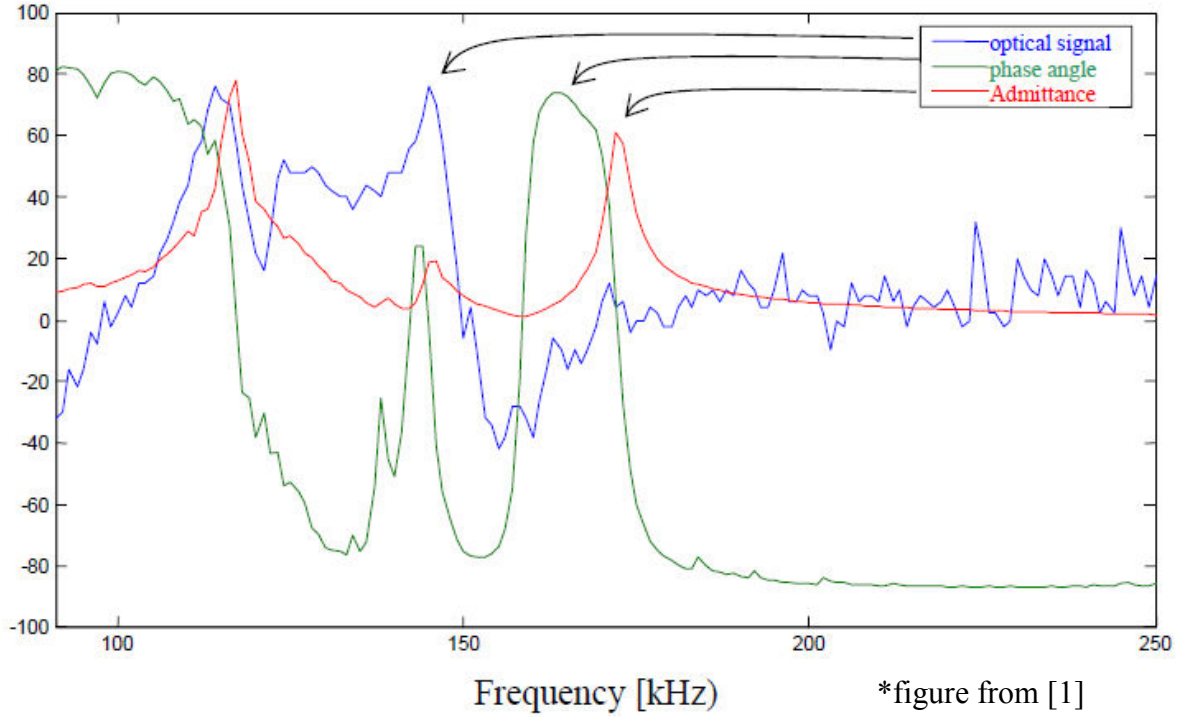


Figure 2.2 Comparison of experimental results of optical signal, phase angle and admittance for PZN-PT sample under electro-optic modulation

They also note that there is no apparent correlation between the admittance magnitudes with the enhanced optical transmission. Using this information another experiment was performed at the frequency corresponding to the d_{33} mode varying the amplitude of the applied signal and observing the optical transmission. Results showed that the signal strength at the photo diode (in volts) was linearly proportional to the square of the applied voltage. This is significant because

under DC conditions the optical signal corresponds linearly with the applied voltage. The authors give the refractive index change of the crystal for each fundamental resonance mode as:

$$d_{33}: \Delta \left(\frac{1}{n^2} \right)_{11}^a = \Delta \left(\frac{1}{n^2} \right)_{33}^a = (p_{1133} + p_{3333})x_{33} \quad (2.2)$$

$$d_{31}: \Delta \left(\frac{1}{n^2} \right)_{11}^a = \Delta \left(\frac{1}{n^2} \right)_{33}^a = (p_{1111} + p_{3311})x_{11} \quad (2.3)$$

$$d_{32}: \Delta \left(\frac{1}{n^2} \right)_{11}^a = \Delta \left(\frac{1}{n^2} \right)_{33}^a = (p_{1122} + p_{3311})x_{22} \quad (2.4)$$

The piezoelectric d coefficients indicate a coupling between the applied electric field in the 3 direction and induced strain in the 1, 2 or 3 directions respectively for d_{31} , d_{32} , d_{33} . The photoelastic p coefficients show the coupling between the strain and refractive index. It was also suggested that enhancement of d_{31} may be larger because p_{1111} and p_{3311} are of the same sign and thus additive corresponding to a larger index change, while p_{1122} and p_{3311} are of a different sign leading to a smaller index change for d_{32} .

In an experiment similar to that of Shikik Johnson, the Naval Research Laboratory found that the electro-optic effect could be enhanced in a Lithium niobate crystal through piezoresonance [3]. The Senarmont compensator technique was used to measure the EO coefficient of the crystal at frequencies up to 700 KHz. At the piezoresonance of the sample the photo elastic effect dominates. The sample was tested under two different field configurations. First, a sinusoidal signal was used to show that the EO effect is enhanced at the resonant modes. It was also shown that the enhancement can be applied at frequencies far higher than just the resonant frequencies. Rather than a sinusoidal input at 1nS, a long pulse was applied with a repetition rate equal to the resonant frequency. The authors provide the following explanation for their results: “Our modeling of the data suggests that the sensitivity enhancements are produced

by the interplay between photo elastic shifts in the refractive indices and the physical vibration modes of the crystals.” The research group that produced this paper has made some investigation on dielectric enhancing of EO [7] but has not yet produced any follow up papers specifically on resonance enhancement.

CHAPTER 3: PIEZORESONANCE EXPERIMENTS

3.1 Piezoelectricity

Piezoelectricity is a property found in certain materials that results in an electrical charge as a result of mechanical stress. It is widely used in many devices. Piezoelectricity only occurs in non-centric materials. When a stress is applied to a piezoelectric material the atoms arrange so there is a net charge. Piezoelectric resonators are used for timing pieces in digital clocks. Piezoelectric motors can be used for optical zoom in cameras. Piezoelectric materials are used for detecting underwater sound vibrations in submarines and it is also a common method of producing a spark in lighters.

There are two equivalent types of piezoelectricity, the direct effect that couples stress X_{kl} with electric polarization P_j and the converse effect that the electric field E_k causes a change in strain x_{ij} . The coefficient for the direct form is [C/N] and for the converse form [m/V].

$$P_j = d_{jkl}X_{kl} \quad \text{Direct} \quad (3.1)$$

$$x_{ij} = d_{ijk}E_k \quad \text{Converse} \quad (3.2)$$

The equations above demonstrate the tensor form of the basic piezoelectric coupling relations. A more detailed view of factors involved can be seen in the piezoelectric constitutive equations (in matrix form) for which there are two equivalent types; the Stress-Charge and Strain-Charge forms.

The Stress-Charge defines the total stress X as a function of the elastic stiffness c_E , the induced and initial strain $(x - x_i)$, the transpose of the piezoelectric coupling matrix e^T , the electric field E , and the initial stress X_i . The electric displacement D is a function of the

piezoelectric coupling e , the induced and initial strain $(x - x_i)$, the free space permittivity ϵ_0 , the relative permittivity ϵ_{rS} , and the remnant electrical displacement D_r .

Stress-Charge form:

$$X = c_E(x - x_i) - e^T E + X_i \quad (3.3)$$

$$D = e(x - x_i) - \epsilon_0 \epsilon_{rS} E + D_r \quad (3.4)$$

The Strain-Charge defines the Total strain x as a function of the elastic compliance s_E , the induced and initial stress $(X - X_i)$, the transpose of the piezoelectric coupling matrix d^T , the electric field E , and the initial strain x_i . The electric displacement D is a function of the piezoelectric coupling d , the induced and initial stress $(X - X_i)$, the free space permittivity ϵ_0 , the relative permittivity at constant temperature ϵ_{rT} , and the remnant electrical displacement.

Strain-Charge form:

$$x = s_E(X - X_i) - d^T E + x_i \quad (3.5)$$

$$D = d(X - X_i) - \epsilon_0 \epsilon_{rT} E + D_r \quad (3.6)$$

Piezoelectricity is a third rank tensor property, meaning that it can only occur in non-centrosymmetric materials (materials with no center of symmetry). There are 32 crystal classes, 11 possess a center of symmetry and thus are not piezoelectric. One class, point group 432, though it is non centrosymmtric, still does not exhibit the piezoelectric effect because the charge along the $\langle 111 \rangle$ direction cancels itself out [8]. This leaves 20 point groups with piezoelectricity which are listed below. The polar point groups may have a spontaneous polarization that occurs even without an applied electric field and are also pyroelectric. There are also non-

crystallographic point groups, called Curie groups that can also be piezoelectric but are not listed here.

Table 3.1 List of crystal point groups that allow for piezoelectricity

Polar	1, 2, 3, 4, 6, m , $mm2$, $3m$, $4mm$, $6mm$
Non-polar	222 , $\bar{4}$, 422 , $\bar{4}2m$, 32 , $\bar{6}$, $\bar{6}m2$, 622 , $\bar{4}3m$, 23

Piezoelectric materials experience a resonant state when an electrical signal is applied at certain frequencies as determined by the density and elastic parameters of the material and the dimension and geometry of the sample. The resonant frequency (f_r) is the point where the admittance is maximum and the anti-resonance (f_a) is where the admittance is at a minimum (See Figure 3.1).

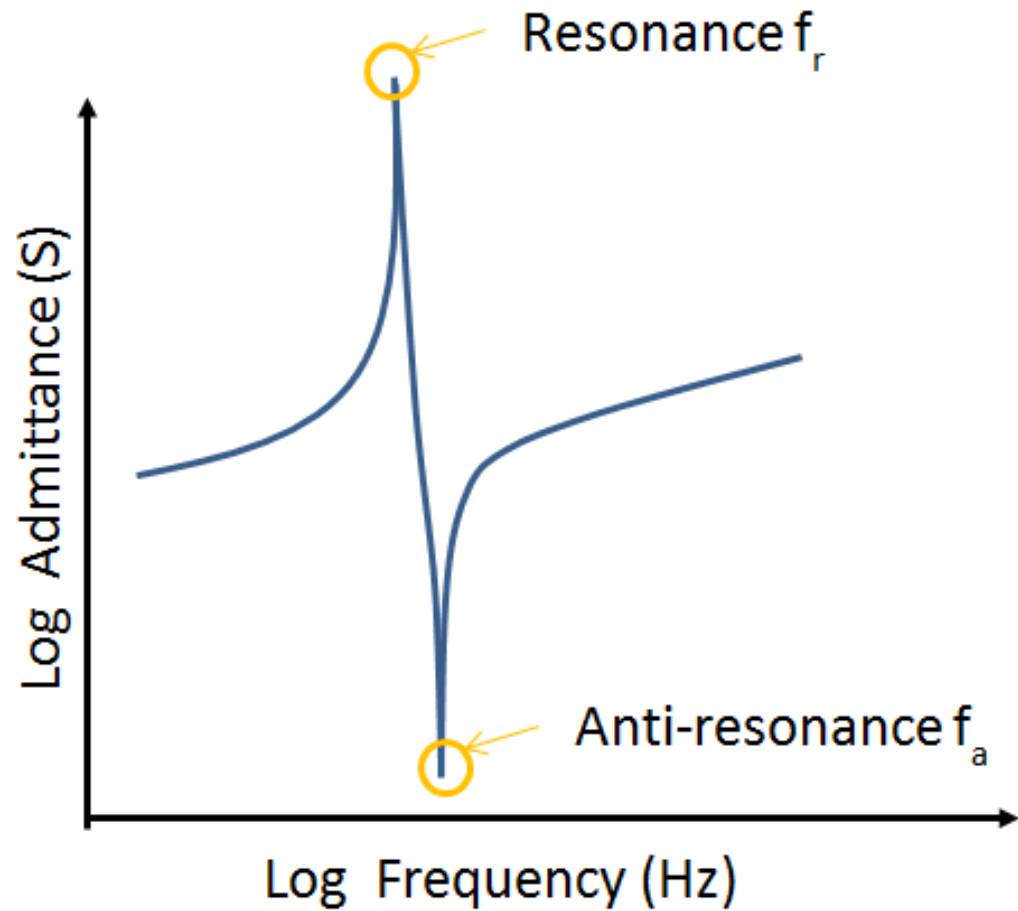


Figure 3.1 Admittance frequency spectrum of a typical piezoelectric resonator showing resonance and anti-resonant frequencies

At f_r the admittance is at maximum (thus an impedance minimum). If the voltage is kept constant (constant amplitude sinusoidal signal), there will be an influx of current into the device. The constant shape change of the device causes motional capacitance.

The resonant frequency f_r is often denoted as f_m referring to the frequency on minimum impedance and the anti-resonant frequency f_a denoted as f_n is the frequency of maximum impedance. The electromechanical coupling factor k is a measure of how well a piezoelectric element can convert electrical energy into mechanical energy. There are several types of

coupling factors that are dependent on the geometry and application direction of the electric field. The effective coupling coefficient which applies to any geometry can be calculated from Equation (3.9). The coefficient k_{31} is applied to plates where the induced strain is perpendicular to the polarization. Conversely the coefficient k_{33} is used for rods where the induced strain is parallel to the polarization. For both the k_{31} and k_{33} coupling the applied electric field must be in the same direction as the polarization.

$$(K_{eff})^2 = \frac{f_n^2 - f_m^2}{f_n^2} \quad (3.7)$$

$$(k_{31})^2 = \frac{(d_{31})^2}{s_{11}^E \epsilon_{33}^T} = \frac{\frac{\pi}{2} \frac{f_n}{f_m} \tan \left[\frac{\pi}{2} \left(\frac{f_n - f_m}{f_n} \right) \right]}{1 + \frac{\pi}{2} \frac{f_n}{f_m} \tan \left[\frac{\pi}{2} \left(\frac{f_n - f_m}{f_n} \right) \right]} \quad (3.8)$$

$$(k_{33})^2 = \frac{(d_{33})^2}{s_{33}^E \epsilon_{33}^T} = \frac{\pi}{2} \frac{f_n}{f_m} \tan \left[\frac{\pi}{2} \left(\frac{f_n - f_m}{f_n} \right) \right] \quad (3.9)$$

Resonance in a piezoelectric vibrator occurs with useful effects in the kilohertz region for most materials and sample configurations. As the frequencies of agitation is increased the sample cannot respond fast enough to the applied signal to keep up; the result of this is that the crystal becomes more constrained as frequency increases, this is the constant strain state. There are two main options around this issue, one is use very small samples that may respond faster and the other is to induce vibrations on the air-dielectric interface; the latter is the bases of surface acoustic waves (SAW). SAW devices typically use interdigitized coplanar electrodes to launch acoustic wave along the surface of a piezoelectric material. The wave stays along the surface and only a few wavelengths actually propagate into the material. SAW devices often are operated at

hundreds of megahertz; they are widely used as electrical filters for cell phones, satellites communicators and other RF devices.

3.2 Crystal Optics

There are three main contributions to refractive index changes relevant to this thesis, the photoelastic effect, optical Pockels and Kerr effects. In each of these effects the refractive index change is often expressed in terms of the impermeability tensor B , defined as:

$$\frac{1}{\Delta n_{ij}^2} = \Delta B_{ij} \quad (3.10)$$

This impermeability is the difference between the inverse of the square of the natural material index and the inverse of the square of the induced index. The fourth rank tensor photoelastic effect has two forms, piezo-optic defined in terms of stress (X) and the elasto-optic defined in terms of strain (x). We can convert piezo-optic to elasto-optic by the matrix formula $p_{mn} = \pi_{mp} c_{pn}$ making use of the elastic coupling c .

$$\Delta B_{ij} = \pi_{ijkl} X_{kl} \text{ piezo-optic} \quad (3.11)$$

$$\Delta B_{ij} = p_{ijkl} x_{kl} \text{ elasto-optic} \quad (3.12)$$

The electro-optic effect comes in two forms, the linear Pockels effect (3rd rank tensor r_{ijk}) and the quadratic Kerr effect (4th rank tensor R_{ijkl}). Both effects can occur in ferroelectric crystals; however the Pockels effect tends to be far more dominant for low field conditions.

$$\Delta B_{ij} = r_{ijk}^x E_k \text{ Pockels} \quad (3.13)$$

$$\Delta B_{ij} = R_{ijkl} E_k E_l \text{ Kerr} \quad (3.14)$$

When the modulating frequency is low there are two contributions to the linear electro-optic effect. This is a combination of photoelasticity and the Pockels effect. The true or primary

EO is considered to be under a constant stress condition (r_{ijk}^x), but because materials with the Pockels effect are also piezoelectric there is a physical deformation that must also be considered and can be described in terms of the elasto-optic and piezoelectric coefficients which is known as the secondary EO contribution. Adding these two terms gives the total electro-optic effect in terms of constant stress.

Reported linear refractive index coefficients are in either constant strain, (r_{ijk}^x) clamped condition above acoustic resonance or constant stress, (r_{ijk}^x) low frequency below acoustic resonance [9]. The electro-optic constant stress tensor is actually a combination of the constant strain tensor, the elasto-optic coefficient (p_{ijlm}) and piezoelectric (d_{jkl}) coefficient.

$$r_{ijk}^x = r_{ijk}^x + p_{ijlm}d_{jkl} \quad (3.15)$$

These effects are related to the impermeability tensor through the electric field and there is also a small contribution from the non-linear electro-optic effect (R_{ijkl}^x). Combining all these effects we have:

$$\Delta B_{ij} = r_{ijk}^x E_k + R_{ijkl}^x E_k E_l \quad (3.16)$$

$$\Delta B_{ij} = r_{ijk}^x E_k + p_{ijkl}x_{kl} + R_{ijkl}^x E_k E_l \quad (3.17)$$

The COMSOL multiphysics platform [10] is a useful tool for modeling the effects discussed in this dissertation. There is no native support for electro-optic and photoelastic effects in COMSOL. However, these equations can easily be programed into the interface and modeled with this software. These calculations typically start with the undeformed optical indicatrix which relates the three principle Z_n axes and the refractive indices n_n .

$$\frac{Z_1^2}{n_1^2} + \frac{Z_2^2}{n_2^2} + \frac{Z_3^2}{n_3^2} = 1 \quad (3.18)$$

Including linear electro-optic effects for the most general (Triclinic) crystal symmetry group yield the expanded equation.

$$\begin{aligned} & \left(\frac{1}{n_1^2} + r_{11}E_1 + r_{12}E_2 + r_{13}E_3 \right) Z_1^2 + \left(\frac{1}{n_2^2} + r_{21}E_1 + r_{22}E_2 + r_{23}E_3 \right) Z_2^2 \\ & + \left(\frac{1}{n_3^2} + r_{31}E_1 + r_{32}E_2 + r_{33}E_3 \right) Z_3^2 \\ & + 2(r_{41}E_1 + r_{42}E_2 + r_{43}E_3)Z_2Z_3 + 2(r_{51}E_1 + r_{52}E_2 + r_{53}E_3)Z_1Z_3 \\ & + 2(r_{61}E_1 + r_{62}E_2 + r_{63}E_3)Z_1Z_2 = 1 \end{aligned} \quad (3.19)$$

For electro-optic materials of 3m symmetry.

$$\begin{bmatrix} 0 & -r_{22} & r_{13} \\ 0 & r_{22} & r_{13} \\ 0 & 0 & r_{33} \\ 0 & r_{51} & 0 \\ r_{51} & 0 & 0 \\ -r_{22} & 0 & 0 \end{bmatrix} \quad (3.20)$$

$$\begin{aligned} & \left(\frac{1}{n_1^2} - r_{22}E_2 + r_{13}E_3 \right) Z_1^2 + \left(\frac{1}{n_2^2} + r_{22}E_2 + r_{13}E_3 \right) Z_2^2 + \left(\frac{1}{n_3^2} + r_{33}E_3 \right) Z_3^2 + \\ & 2(r_{51}E_2)Z_2Z_3 + 2(r_{51}E_1)Z_1Z_3 + 2(-r_{22}E_1)Z_1Z_2 = 1 \end{aligned} \quad (3.21)$$

If the electric field is only applied along the Z direction then the equation reduces to:

$$\left(\frac{1}{n_1^2} + r_{13}E_3 \right) Z_1^2 + \left(\frac{1}{n_2^2} + r_{13}E_3 \right) Z_2^2 + \left(\frac{1}{n_3^2} + r_{33}E_3 \right) Z_3^2 = 1 \quad (3.22)$$

Because there are no cross-coupling terms then the indicatrix does not rotate due to the electric field and because $n_1 = n_2$ the index change can be described in two equations (where optical propagation is along the y axis). The ordinary refractive index n_o is parallel to the Z_1 direction while the extraordinary refractive index n_e is parallel to the Z_3 direction.

$$n'_x = \frac{1}{\sqrt{\frac{1}{n_o^2} + r_{13}E_z}} \quad (3.23)$$

$$n'_z = \frac{1}{\sqrt{\frac{1}{n_e^2} + r_{33}E_z}} \quad (3.24)$$

These equations are often further simplified:

$$n_x'^2 = \frac{1}{\frac{1}{n_o^2} + r_{13}E_z} = \left(\frac{n_o^2}{n_o^2}\right) \frac{1}{\frac{1}{n_o^2} + r_{13}E_z} = n_o^2 \left(\frac{1}{1 + n_o^2 r_{13}E_z} \right) \quad (3.25)$$

The equation can be simplified by considering Figure 3.2 (a). The function $f1[x]=1/(1+x)$ matches $f2[x]=1-x$ very well for very small values of x . Thus if the product of $n_o^2 r_{13}E_z$ is sufficiently small the equation becomes [11]:

$$n_x'^2 \approx n_o^2(1 - n_o^2 r_{13}E_z) \quad (3.26)$$

And once again if $n_o^2 r_{13}E_z$ is sufficiently small the term under the radical can be simplified from $f3[x]=\sqrt{1-x}$ to $f4[x]=1 - \frac{1}{2}x$.

$$n'_x \approx n_o \left(1 - \frac{1}{2} n_o^2 r_{13}E_z \right) \quad (3.27)$$

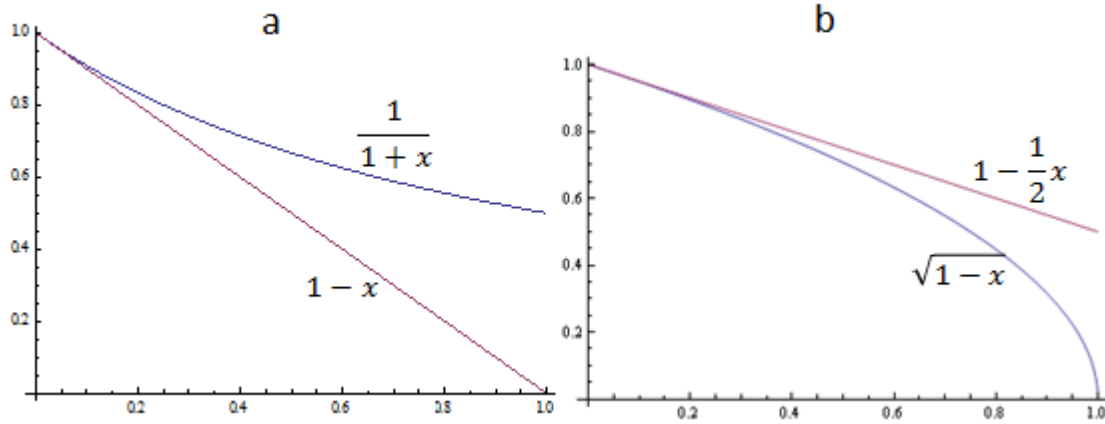


Figure 3.2 Common equation simplifications for calculating the electric field induced Birefringence in an electro-optic modulator

This simple method can be used for the Z direction index and is summarized below for both.

$$n'_x = n'_y \approx n_o - \frac{1}{2} n_o^3 r_{13}^x E_z \quad (3.28)$$

$$n'_z \approx n_e - \frac{1}{2} n_e^3 r_{33}^x E_z \quad (3.29)$$

3.3 Senarmont Compensator Technique

The Senarmont compensator technique is a method used for determining the low frequency (Max 500MHz) electro-optical coupling of a crystal. Electro-optic crystals usually require high fields to produce an induce Birefringence large enough to measure, which makes them difficult to test at higher frequencies with standard signal generators. This technique overcomes this issue and allows for accurate testing. A typical setup is shown in the figure below [11].

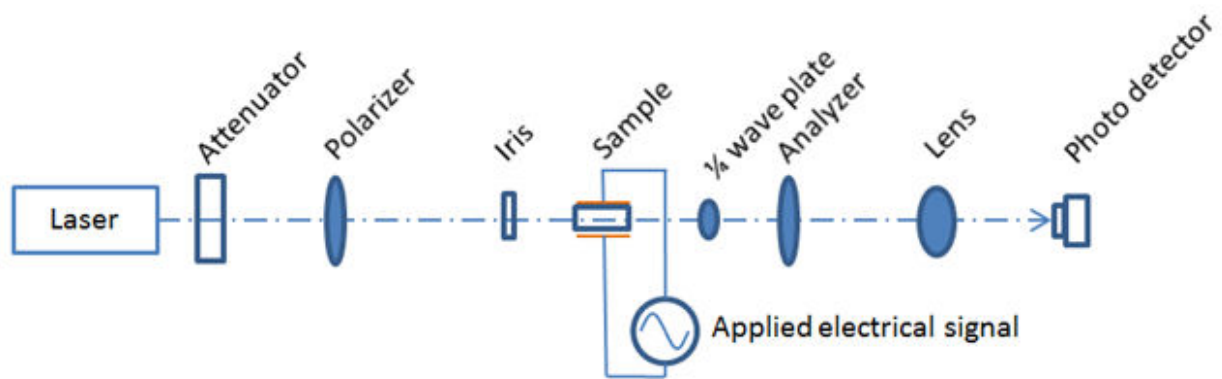


Figure 3.3 Schematic of experiment based on Senarmont compensator technique

The setup always starts with a coherent/monochromatic light source which is most commonly a laser. The intensity of the laser light is controlled by an attenuator to bring the power down to a safer but adequate few milliwatts of power. The light is incident on the sample under test by way of crossed polarizers on either side known as the polarizer and analyzer – though they are identical parts. The polarizer allows only light with a certain alignment to pass through it typically at 45° from the vertical, while the analyzer is set to -45° from the vertical. Under this condition all light is blocked if the light is propagating along the optical axis or if it is isotropic. When the sample is introduced between these devices its natural birefringence causes a small rotation of the polarized light which in turn results in light output at the analyzer. This birefringence can be controlled by applying a modulating signal to the sample. So application of an electric field causes an amplitude change of the light which reaches the photodetector. The quarter wave plate is used to turn elliptically polarized light into linearly polarized light, the angle of which is dependent on the crystal birefringence; this effectively adds an optical bias of $\pi/4$ to the modulator. The figure below represents the maximum optical output possible in the crystal. An ac signal applied to the linear portion of the transmittance sine response can give a

minimally distorted optical output. This allows us to use a dc type test for small signal ac analysis.

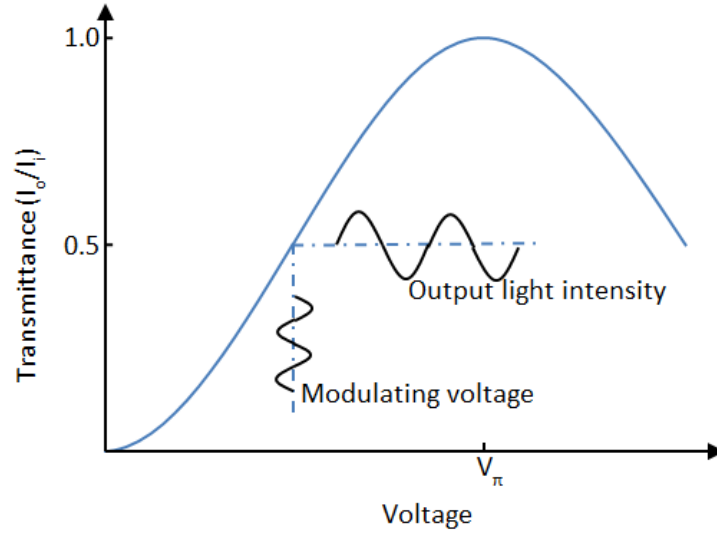


Figure 3.4 Transmittance curve (in blue) for applied DC field on sample in crossed polarizer configuration and effect of quarter wave plate on optical biasing for ac modulation around the 50% transmittance point

The transmission curve in Figure 3.4 has been derived in many sources [12, 13] and is shown here. Considering first the more simple case of just the polarizer, sample and analyzer the output intensity (Equation 3.30) is a function of the field amplitude A and phase retardation δ . This can be reduced to a more simple form in Equation (3.32).

$$I_o = \left| \frac{A}{\sqrt{2}} (e^{-i\delta} - 1) \right|^2 = \frac{A^2}{2} (e^{-i\delta} - 1)(e^{i\delta} - 1) \quad (3.30)$$

$$I_o = \frac{A^2}{2} (2 - (e^{i\delta} + e^{-i\delta})) = \frac{A^2}{2} \left(2 - 2 \left(\frac{e^{i\delta} + e^{-i\delta}}{2} \right) \right) \quad (3.31)$$

$$I_o = \frac{A^2}{2} (2 - 2 \cos \delta) \quad (3.32)$$

Using the relation from the trigometric half angle formulas.

$$\sin^2 \frac{B}{2} = \frac{1}{2}(1 - \cos B) \quad (3.33)$$

$$I_o = \frac{A^2}{2} 2(1 - (\cos \delta)) = 2A^2 \sin^2 \left(\frac{1}{2} \delta \right) \quad (3.34)$$

$2A^2$ is proportional to the input light intensity. The modulating signal and offset is given by $V = V_0 + V_m \sin \omega t$. When V_0 is set to $\frac{V_\pi}{2}$ (V_π gives the peak transmittance) this makes an offset equivalent to what a quartz wave plate adds, resulting in a transmission that is biased around the more linear $\frac{V_\pi}{2}$ point. This is key to the measurement as very large modulation signals or bias points may result in harmonics. The normalized transmittance on a scale of zero to one is a ratio of the output intensity I_o to the input Intensity I_i .

$$\frac{I_o}{I_i} = \sin^2 \left(\frac{1}{2} \delta \right) = \sin^2 \left(\frac{\pi V}{2V_\pi} \right) = \sin^2 \left(\frac{\pi}{2V_\pi} (V_0 + V_m \sin \omega t) \right) \quad (3.35)$$

$$V_0 = \frac{V_\pi}{2} \quad (3.36)$$

$$\frac{I_o}{I_i} = \sin^2 \left(\frac{\pi}{2V_\pi} \left(\frac{V_\pi}{2} + V_m \sin \omega t \right) \right) = \sin^2 \left(\frac{\pi}{4} + \frac{\pi V_m}{2V_\pi} \sin \omega t \right) \quad (3.37)$$

Equation (3.37) can be further simplified by applying the identities in Equations (3.38) and (3.39).

$$\sin^2 (u) = \frac{1}{2}(1 - \cos(2u)) \quad (3.38)$$

$$\cos \left(u + \frac{\pi}{2} \right) = -\sin(u) \quad (3.39)$$

$$\frac{I_o}{I_i} = \frac{1}{2} \left(1 - \cos \left(\frac{\pi}{2} + \frac{\pi V_m}{V_\pi} \sin \omega t \right) \right) = \frac{1}{2} \left(1 + \sin \left(\frac{\pi V_m}{V_\pi} \sin \omega t \right) \right) \quad (3.40)$$

If $\frac{\pi V_m}{V_\pi} \ll 1$ then the equation can be reduced to

$$\frac{I_o}{I_i} \approx \frac{1}{2} \left(1 + \frac{\pi V_m}{V_\pi} \sin \omega t \right) \quad (3.41)$$

So a modulating voltage V_m will linearly change the intensity of the signal at the photodetector. The typical setup for this configuration is a bulk transverse electro-optic modulator as shown in Figure 3.5. The sample consists of an electrode on the a-b faces so that an electric field can be applied in the c direction. The laser light travels in the b direction and the Birefringence caused by the 3 and 1 components of the refractive index induce a phase change in the polarization components. Figure 3.5 is an explanatory arrangement, but other orientations can also be used.

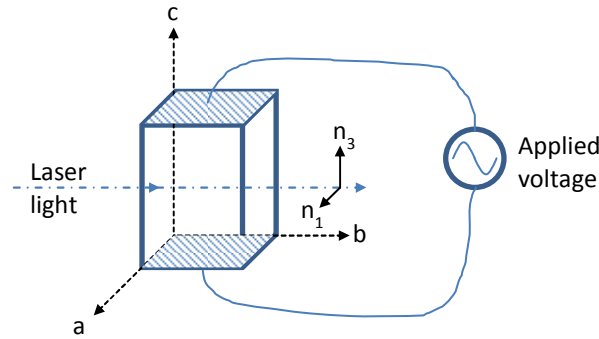


Figure 3.5 Orientation of applied field and optical propagation for transverse electro-optic modulator

The modulated signal can be expressed simply in terms of the photodiode signal or as the actual electro-optic r coefficient. There are several r coefficients depending on the type of material and configuration. This dissertation mostly studies Perovskite materials which have three electro-optic coefficients r_{13} , r_{33} and r_{51} . The configuration described above can measure a

combination of the r_{13} and r_{33} coefficients directly, this is the effective r_c coefficient in Equation (3.42).

$$r_c = r_{33} + \left(\frac{n_o}{n_e}\right)^3 r_{13} \quad (3.42)$$

The r_c coefficient can be calculated from the thickness, t of the sample, the length of the sample in the light propagation direction, l_o , the wavelength of the laser, λ , and the extraordinary refractive index n_e . The coefficient also requires three experimental parameters; the amplitude V_{app} of the modulating voltage, the measured voltage, V_{out} at the photodiode (after the transimpedance amplifier), and the voltage V_{pp} . V_{pp} is obtained by rotating the quarter wave plate and monitoring the voltage at the photodiode. As the plate is rotated the voltage will vary sinusoidally; it is the peak-to-peak voltage from this measurement that is used to find V_{pp} in Equation (3.43).

$$r_c = \frac{2\lambda}{n_e^3} \left(\frac{t}{l_o}\right) \left(\frac{V_{out}}{V_{pp} \cdot V_{app}}\right) \quad (3.43)$$

3.4 Samples

Three different samples were used for experimental measurements in this section; PMN-30%PT; quartz; and PZN-4.5%PT. Both PMTPT and PZNPT are rhombohedral at room temperature but macroscopically tetragonal 4mm after poling and are ferroelectric. Quartz is crystal class 32, it is piezoelectric but does not have reversible polarization thus it is not ferroelectric. The dimension and configuration of the samples is summarized below.

Table 3.2 Sample compositions, poling, configuration, and dimensions used in piezoelectric experiments

Sample	Composition	Poling	dimension [mm]		
			x	y	z
1	PMN-30%PT	[001]	1.25	3.00	2.25
2	Quartz	None	5.64	2.48	18.49
3	PZN-4.5%PT	[001]	2.2	2.46	2.0

Table 3.3 Sample configurations and Symmetries used in piezoelectric experiments

Sample	Electroded face	Area [mm ²]	Thickness [mm]	Symmetry @ R.T.
1	xy		2.25	4mm
2	yz		5.64	32
3	xy	5.412	2.0	4mm

3.5 Admittance Spectrum and Resonant Modes

The admittance spectrum of the samples was examined with the HP 4194A to determine the resonant frequencies. The admittance spectrum is used to determine the resonant frequencies of the sample. When the magnitude of the admittance reaches a maximum this is the resonant frequency and when minimum this is the anti-resonance. The resonant frequencies indicate where there is large electrical-mechanical coupling in the sample and where the sample physical displacement and strain is very high. These parameters are very important to the study of resonant enhancement of the optical transmission. The resonant frequencies f_r of the extension modes of a rectangular rod can be calculated with the formula below from IEEE standards on Piezoelectricity [14]. Where l is the sample length, v is the acoustic velocity, ρ is the density and S is the elastic compliance. The parameter n is a positive odd integer used to calculate the harmonics.

$$f_r(n) = \frac{n}{2l} v^2 = \frac{n}{2l} \sqrt{\frac{1}{\rho S_{11}}} \quad n = 1, 3, 5, \dots \quad (3.44)$$

For the quartz sample

$$\rho = 2651 \left[\frac{kg}{m^3} \right] \quad (3.45)$$

$$S_{11}^E = 1.277 \times 10^{-11} [1/Pa] \quad (3.46)$$

$$f_r(n) = \frac{n}{2 * 18.49[mm]} \sqrt{\frac{1}{2651 \left[\frac{kg}{m^3} \right] 1.277 \times 10^{-11} [1/Pa]}} \quad n = 1, 3, 5, \dots \quad (3.47)$$

$$f_r(1) = 146.971 \text{ KHz}$$

$$f_r(3) = 440.914 \text{ KHz}$$

$$f_r(5) = 734.857 \text{ KHz}$$

$$f_r(7) = 1.0288 \text{ MHz}$$

(3.48)

The PMN-PT and PZN-PT sample's resonance frequencies are not easily identified using the above formula due to their low dimensional aspect, to identify these frequencies finite element simulations are used in the next chapter.

3.6 Electro-optic Measurements

The above samples were measured using a crossed polarizer technique to determine the electro-optic effect. The lock-in amplifier (Stanford Research Model SR830) was used to measure the signal in the low frequency range from 1 mHz to 102 KHz and the higher frequency range from 25 KHz to 200 MHz was tested with a Model SR844 (Stanford Research). The high frequency limiting factor of this measurement is the transimpedance amplifier used to amplify the photodiode current output to a voltage which has a bandwidth limitation that is dependent on the amplifier gain.

The PMN-PT and PZN-PT samples are ferroelectric and have a reversible polarization while Quartz is on piezoelectric and the polarization cannot be reversed. Measurements of quartz were done to determine if electro-optic transmission enhancement exists in piezoelectric materials. The figure below shows the measurement configuration for these tests; additional detail on the optical setup is given in the Senarmont compensator technique section of this dissertation.

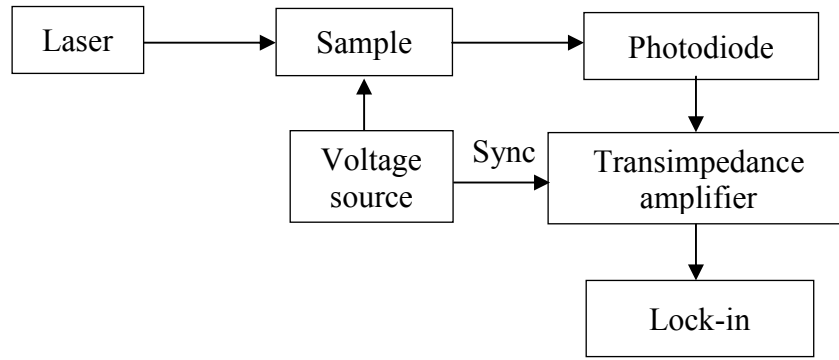


Figure 3.6 Block diagram of electro-optic measurement setup

The electro-optic coefficients of PMN-PT and PZN-PT are not well reported on in the literature and are only really available for a few compositions. Nevertheless, the actual coefficients are likely very similar to that of known samples with similar concentrations of PT. The electro-optic coefficients of PZN-12%PT are reported to be $r_{13}=7$ [pm/V], $r_{33}=134$ [pm/V] and $r_{51}=462$ [pm/V] as reported in [15]. The electro-optic coefficients of PMN-38%PT are reported to be $r_{13}=25$ [pm/V], $r_{33}=70$ [pm/V] and $r_{51}=558$ [pm/V] as reported in [16]. The electro-optic coefficients of Quartz (SiO_2) are reported to be $r_{11}= -0.47$ [pm/V], $r_{41}=0.20$ [pm/V] for the wavelength range of 409 to 605 nm as reported in [9]. The electro-optic matrices for the two crystal classes are shown in Equation 3.49 below. These matrices relate the electric field E_1 , E_2 and E_3 to the six components of the impermeability ΔB_n (where n is an integer from 1 to 6).

$$4\text{mm} \begin{pmatrix} 0 & 0 & r_{13} \\ 0 & 0 & r_{13} \\ 0 & 0 & r_{33} \\ 0 & r_{51} & 0 \\ r_{51} & 0 & 0 \\ 0 & 0 & 0 \end{pmatrix} \quad 32 \begin{pmatrix} r_{11} & 0 & 0 \\ -r_{11} & 0 & 0 \\ 0 & 0 & 0 \\ r_{41} & 0 & 0 \\ 0 & -r_{41} & 0 \\ 0 & -r_{11} & 0 \end{pmatrix} \quad (3.49)$$

The sample was measured in two different configurations; i.e., with the optical propagation along the long dimension (18.49 mm) of the sample and the other along the shortest dimension (2.48 mm) (See Figure 3.7).

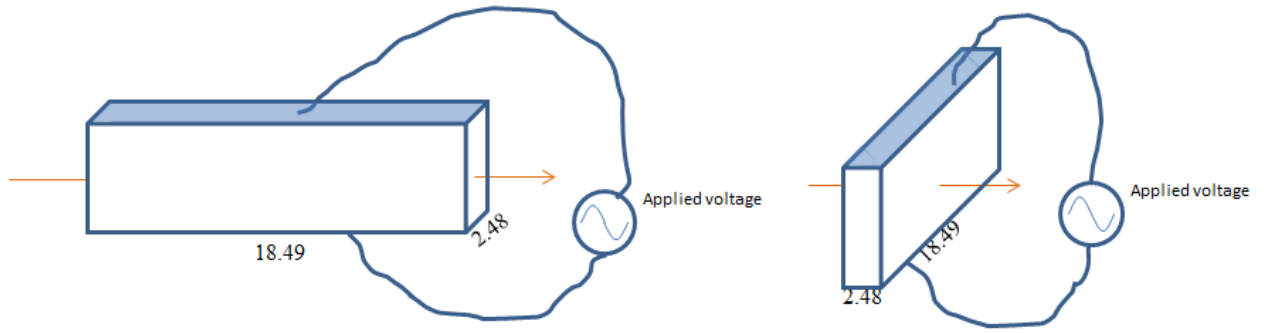


Figure 3.7 Electro-optic test configuration used for quartz samples (shaded areas are electroded)

The electro-optic response of the quartz sample (Sample #2) is shown in Figure 3.8. The r_{11} coefficient was calculated using Equation 3.43 to be approximately 1 [pm/V] which is much higher than the reported value of 0.47 [pm/V] which is actually the low frequency (constant stress) response. Both of these configurations will test the r_{11} coefficient, differences in the two are partly the result of measurement error and partly from the resonant nature of the material. One configuration may show higher values than the other based on the main direction of strain at that particular mode. Also shown in the plot is the admittance spectrum of the sample (blue trace). The resonant modes tend to be very small because of the small piezoelectric coupling

found in quartz, however the electro-optic response is very complex, clearly showing a complex response due to resonance. Figure 3.9 displays the same results of Figure 3.8 but zoomed in on the strongest resonance. The electro-optic response correlates well with the admittance response and in this case the peak electro-optic enhancement seems to line up with the mid-way point between the resonance and anti-resonance. This is the point of maximum admittance slope and is consistent with Equation 2.25 as proposed in [1].

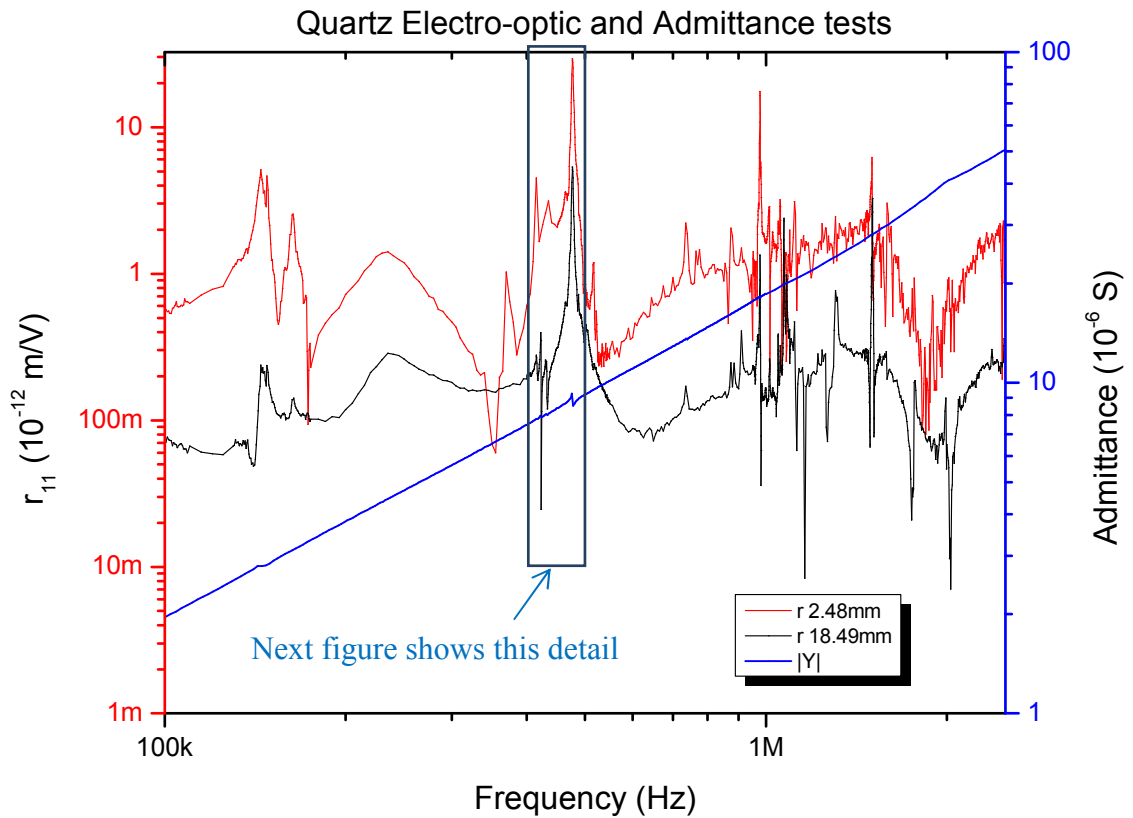


Figure 3.8 Results of quartz electro-optic test showing measured electro-optic coefficient and admittance response

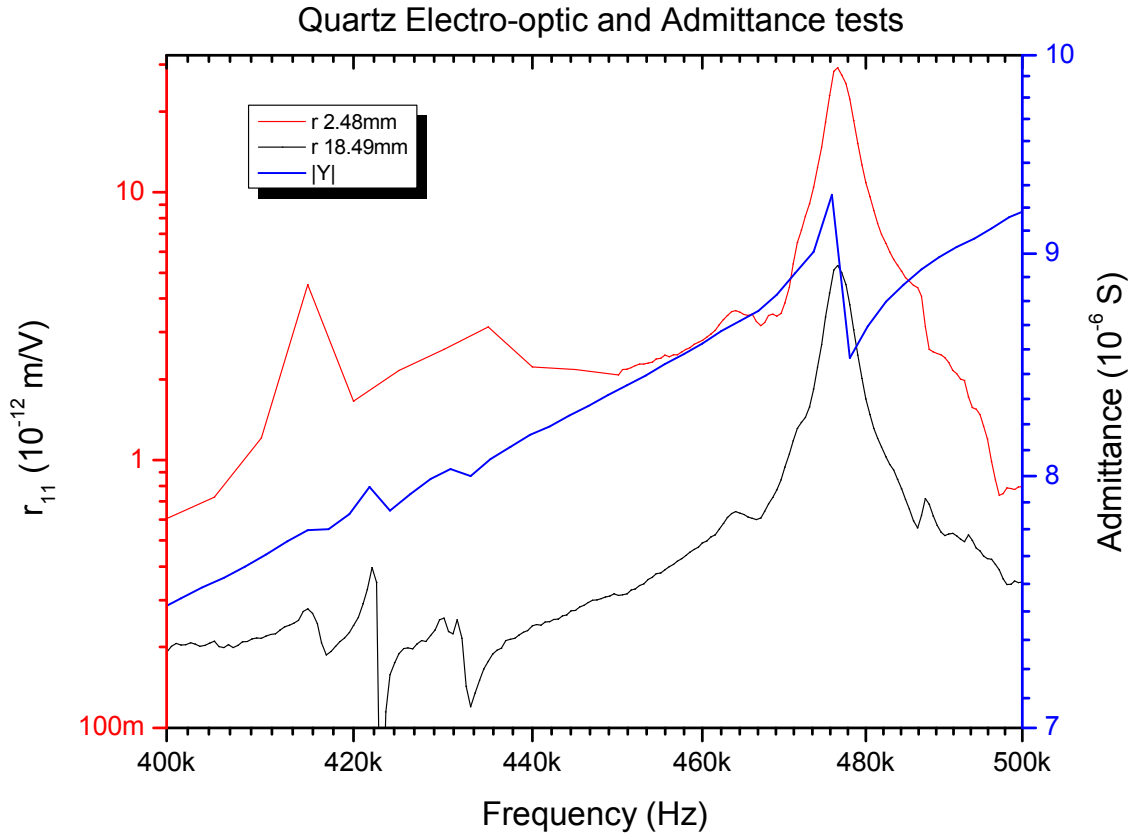


Figure 3.9 Quartz electro-optic test (from previous figure) zoomed in on largest resonance

The electro-optic and admittance spectrum of PMN-30%PT (Sample #1) is shown in Figure 3.10. Below 1Mz there is a strong signal from the admittance indicating strong vibration of the sample and the EO response is likewise strong; above 1MHz the sample becomes clamped but clearly the large EO response continues as indicated by several significant peaks. This demonstrates that the optical signal enhancement may be large even without high strain.

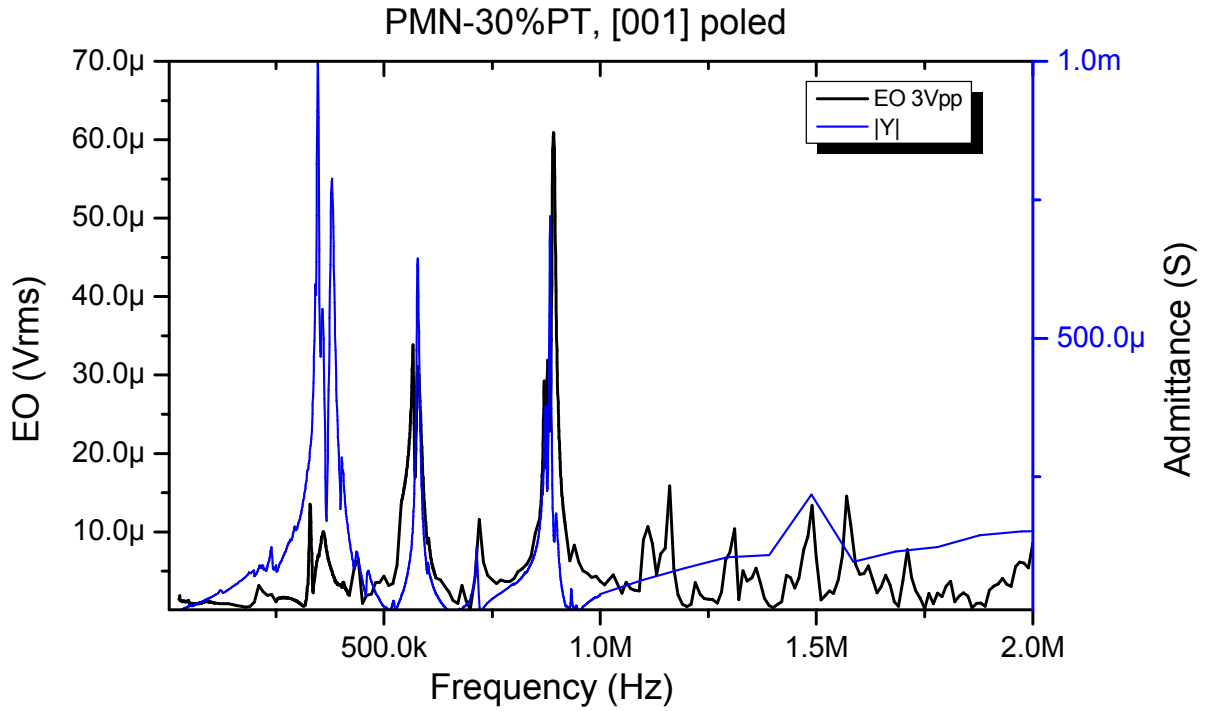


Figure 3.10 Results of PMN-30%PT electro-optic test showing measured electro-optic voltage as measured at the photodiode and admittance response

3.7 Optical Transmission

The transmission of the electro-optic signal is known to increase near resonance when using the Senarmont compensator technique. This technique is a measure of the electric and optical coupling but there has been little work examining a resonating electro-optic crystal with a simple light transmission measurement.

During sample preparation ferroelectric samples become more optically transparent to visible light due to the poling process. Under high electric field the dipoles in the sample orient in the direction of the applied field and the distance between domains becomes smaller resulting in increased optical transparency. This is particularly true in samples such as PMN-PT which is not a typical single crystal sample. The transparency of single crystals are governed primarily by

the intrinsic band gap of the material, but PMN-PT has many domains which typically causes low transparency. However, because of the very small distance between domains the overall result is transparency.

There has been some work in the area of biased transmission measurement [17] though the tests were not done specifically at the piezoelectric resonant frequencies. The researchers modulated the samples with high field and observed the transmission. The tests were done from DC to 150 KHz and it was found that this modulation increased transmission and that higher modulation frequencies resulted in higher transmission. The applied electric field needed a threshold of about 100 V/mm to improve transmission. It is believed that the response of the sample transparency is similar to what occurs during the poling process, the difference being a lower field with modulation that allows the crystal domains to arrange for greater transparency. It may be possible to test the transmission in the same way and determine if resonance can improve the transmission, perhaps with a lower operating field.

The increased transmission under electro-optic testing using crossed polarizers has been well demonstrated in the previous section however, there is still a question as to whether AC biasing may have an impact on the optical transmission, reflection, or absorption of the material. The PMN-30%PT sample (Sample #1) was tested from 500 nm to 900 nm in an optical spectrometer (See Figure 3.11). The sample was tested under both normal conditions (no bias) and under resonance. The strongest resonance for this sample is ~338.8 kHz, however the results show no measurable change in the response at this frequency or at frequencies close to it. A few conditions were retested to verify repeatability. The first non-biased condition shows a slightly larger response at its peak but further measurements verified there is no repeatable or measurable change due to resonance.

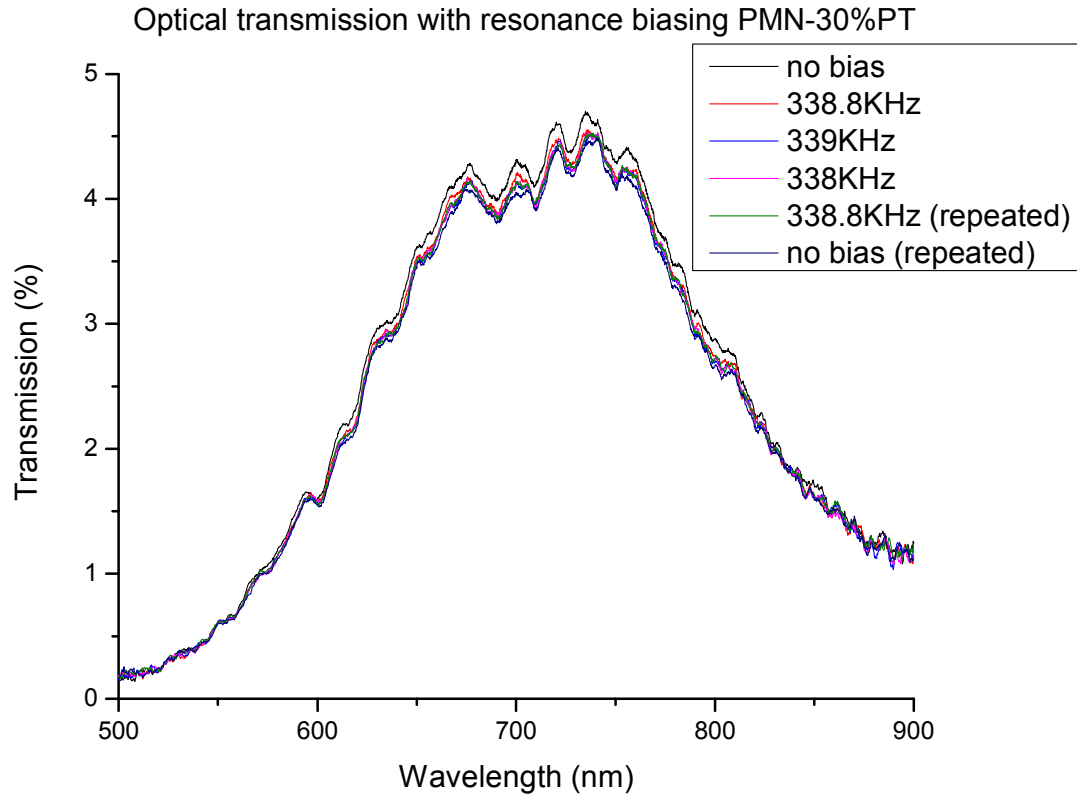


Figure 3.11 Results of optical transmission test of PMN-30%PT under piezo-resonant ac bias using low fields ($< 50\text{V/cm}$)

Although this test did not produce measurable difference due to resonance it may still be possible to observe increased transmission at resonance. The results of work by the previous author [17] as mentioned above showed that the ac bias field must be at least 100 V/mm (1000 V/cm); this is of course much higher than the 50 V/cm used in Figure 3.11. Larger fields were not used in this test because of the lack of suitable test equipment.

3.8 Summary

Optical and dielectric measurements have been performed to characterize the samples. The admittance measurements show the resonant and anti-resonant frequencies of the samples. Strong fundamental resonant response is clear in the 100 kHz to 1MHz region for all the samples

and harmonics continue into the low megahertz region. Samples with low aspect ratio dimensions tend to have resonant modes that are not pure; that is, there is mixing between the modes leading to a very complex admittance spectrum. Mode mixing becomes more pronounced for resonant harmonics such that individual modes are no longer distinguishable. Enhancement of the electro-optic effect was observed near the resonant modes of most samples, especially near modes where strain is transverse to the direction of light propagation. Anti-resonant modes do not seem to contribute to enhancement; this is likely due to an impedance maximum at anti-resonance resulting in minimum current in the device. When analyzing the transmission versus optical wavelength spectrum, sample resonance was not shown to improve transmission. These experiments were performed with a low electric field of less than 50 V/cm; it may be that a higher field will reveal enhancement near resonance.

CHAPTER 4: PIEZORESONANCE FINITE ELEMENT ANALYSIS

Section 4.2 McIntosh, R., C. Garcia, et al. (2011). "Periodically Poled Structure on Microwave Transmissions Evaluated by Scattering Parameters." *Integrated Ferroelectrics* 131(1): 219-229.

Section 4.3 McIntosh, R., A. S. Bhalla, et al. (2012). Simulation of Enhanced Optical Transmission in Piezoelectric Materials. *Advances and Applications in Electroceramics II*, John Wiley & Sons, Inc.: 55-64.

4.1 Finite Element Analysis

Finite element analysis (FEA) is a computational method of solving real world physics problems described by partial differential equations (PDE). Typically models based on FEA consist of at least one domain and a PDE for that domain. There are also boundary conditions defined on the outer surface of the domain or where one domain meets another. Once these three primary conditions are met the domain(s) are divided up into a discrete number of pieces called a mesh. These mesh elements are typically triangular or quadrilateral in shape and are smaller near areas of greater flux or areas of the domain that are smaller. FEA solves the PDE on each element and then recombines them all by way of superposition to solve the problem on the entire geometry.

4.2 Microwave Transmission in Periodic Ferroelectric Domain Structure

A combined experimental and numerical investigation has been conducted to study piezoelectric resonance process in relation to the strain gradient, the local polarization, and the displacement current in a piezoelectric crystal-resonator. Experimental discoveries showed that at certain sub-wavelengths of the fundamental piezoelectric resonant frequencies of a given resonator, electro-optic coefficients and also the optical transmission in an otherwise opaque configuration are greatly enhanced. This paper reports preliminary study by finite element analysis modeling on microwave transmission behavior when the piezoelectric material is

modulated by periodic polarization distribution defined by piezoelectric resonance or generated by periodic poling. Transmission parameters are simulated in wide frequency range to characterize wave propagation behavior of the material in various local polarization conditions related to piezoelectric transverse or longitudinal resonance modes.

It was reported that piezoelectric resonance can have a significant effect on the electro-optic (EO) response of a material [1, 3, 4, 6]. In the resonant condition an improved coupling is observed (by way of a dual frequency scanning) at frequencies well above the fundamental resonant frequency. In a previous experiment an electro-optic crystal (PZN-PT) was measured using the Senarmont compensator technique for analyzing the electro-optic r coefficient at radio frequencies ($<500\text{MHz}$). By applying a signal at one of the piezoelectric resonant frequencies of the material while measuring the EO coefficient at various frequencies below, at, and above resonance, improved optical transmission was obtained near the fundamental and at several harmonics above the piezoelectric resonant frequencies.

The precise reason for this improved coupling is not completely known; however it is believed to be a result of increased coupling of the optical photons and acoustic phonons brought on by the periodic electric displacement associated with the modulation of local polarization. The displacement is the most pronounced while the sample is under piezoelectric resonance. At constant temperature in a piezoelectric material the electric displacement (D) or polarization (P) is a function of the permittivity ($\epsilon_0\epsilon_r$), electric field (E), remnant polarization (P_{r0}), and additionally a strain (x) coupled piezoelectric component.

A sample at resonance due to low frequency excitation induces a strain in the material and results in a change in the displacement. When this resonance is defined by one of the resonant modes of the sample leading to a strong periodic electric displacement in the sample the

electro-mechanical coupling can be very effective. Due to this effect the transmission of an electromagnetic wave may be increased (or decreased) by the induced local polarization modulation (or alternatively by a periodically polarization-inverted structure). Under resonance the sample deforms in response to the applied signal. The polarization of the material will periodically change in magnitude and direction in a sinusoidal manner as shown in the top portion of Figure 4.1. Similarly in a ferroelectric material where a high field is used to pole the sample the polarization can be reversed in a uniform fashion with ideally positive and negative polarizations of the same magnitude.

In this chapter, we report finite element COMSOL multiphysics modeling to simulate the situation that a periodically poled ferroelectric material inserted into a two port transmission line. One of the scattering parameters or the transmission parameters S_{21} , defined as the forward transmission gain with the output port terminated in a matched load (expressed in decibels $S_{21}(dB) = 20 \cdot \log_{10}(|S_{21}|)$), is used to examine broadband solutions of the system in order to characterize the behavior of the material with various local polarization conditions, especially the conditions that are associated with piezoelectric resonance modes.

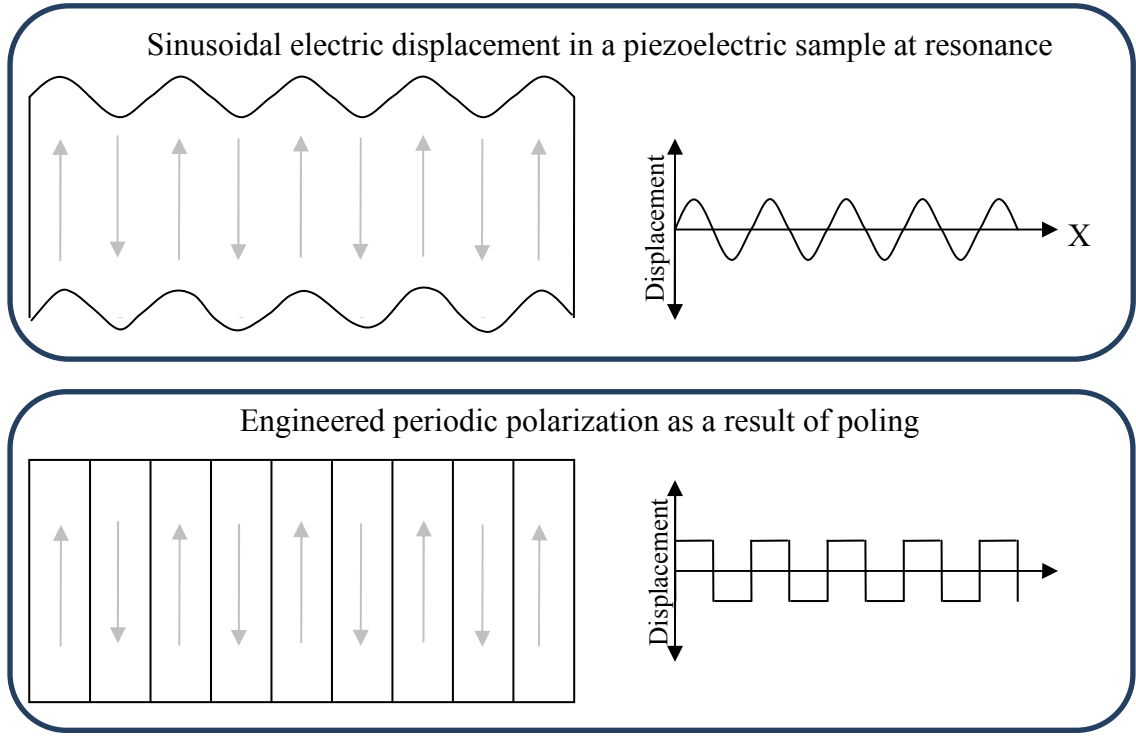


Figure 4.1 Periodically polarized antiparallel structure within a piezoelectric sample

COMSOL, a finite element analysis solver and simulation software, is used to study the effect of a periodically poled structure on the scattering parameters of a rectangular waveguide. In COMSOL, when using the RF module and harmonic propagation application mode the polarization cannot be defined negatively, thus a few modifications were made to the governing equations. This modeling method has been carried out based on charge balance assumptions and typically polarization values are resultant of piezo-resonant activity. The displacement field can be described in terms of permittivity and electric field $D_i = \epsilon_{ij}E_j$. We are concerned particularly with the displacement in the transverse (z or 3) direction $D_3 = \epsilon_{3j}E_j$. The remnant displacement that remains after a ferroelectric sample is poled and the field has been removed provides an offset to the displacement field. Including the polarization offset (P_{3r0}) we have the formula as

$$D_3 = \epsilon_{3j}E_j + P_{3r0}.$$

The basic waveguide structure is shown in Figure 4.2. The length, width, and height of the guide were assumed at $2 \times 1 \times 1 \text{ cm}^3$. The wave propagates in the x direction and the transverse electric field is along the z direction. This structure uses 2 ports, the wave is excited on the yz face farthest to the left (port 1) and the other port is the yz face farthest to the right (port 2), the other 4 external surfaces are configured (with or without metallization) accordingly for each simulation.

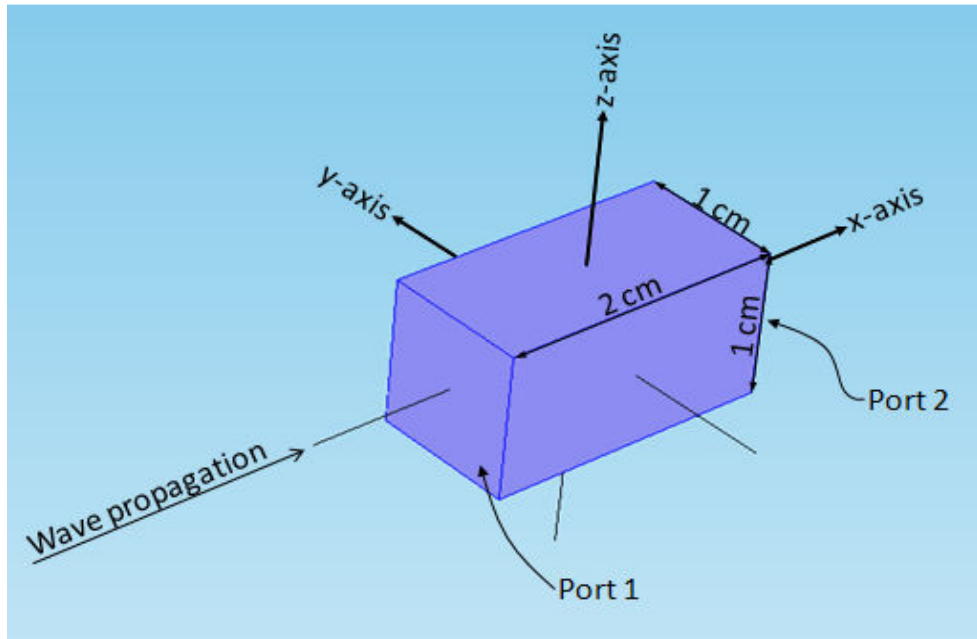


Figure 4.2 Simulation setup for sample inserted in microwave waveguide showing electromagnetic wave excited on port 1 and travels to port 2 along the x-axis

Figure 4.3 illustrates five polarization conditions considered when the direction of the polarization is parallel to the z-axis. Each polarization-uniform area is referred as an element. The waveguide dimensions are the same regardless of the number of elements. The two shades distinguish the polarization in the positive or negative z-directions; all conditions studied started with a polarization in +z-direction. The piezoelectric material is assumed to have zero field impedance Z_0 and a zero field permittivity $\epsilon_r(0)$.

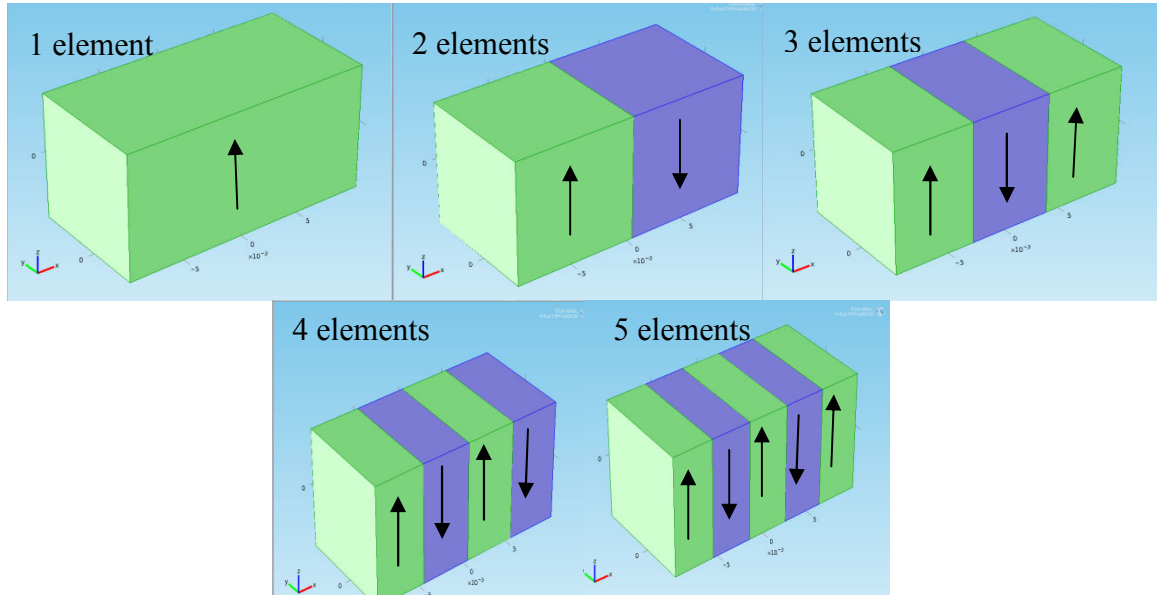


Figure 4.3 Antiparallel step polarization configuration for 1-5 elements in microwave FEA model

The transmission parameter S_{21} in dB is simulated for transmitted signal in a frequency range of 0.1 to 40 GHz in steps of 0.25GHz. The effects of the number of polarized elements, magnitude of the polarization and length of the waveguide on the transmitted signal are studied.

4.2.1 Resonator Surfaces Free From Metallization

All surfaces of the y- and z- direction of the material, refer to Figure 4.2, are free from any metallization in this simulation. The four surfaces are scattering boundaries while the other two faces (\parallel x-axis) are wave ports. This configuration is equivalent to that in which the metallization is removed after the sample is (periodically) poled along the z-direction. Antiparallel step polarization configuration with one to five elements are considered, as depict in Figure 4.3.

In Figure 4.4 we can see the S_{21} response in a four element configuration over a broad frequency range from 1 to 40 GHz as a function of polarization strength. The waveguide cutoff frequency

is at about 7.5 GHz for all conditions, attributed to the dimension and the impedance of the sample. A drop in transmission is observed at ~32 GHz for this sample of four polarization-inverted elements. Other than that, an increased polarization amplitude causes an amplification of the transmission; however the overall shape of the response as function of frequencies remains the same for all polarization levels above 0.1 pC/cm².

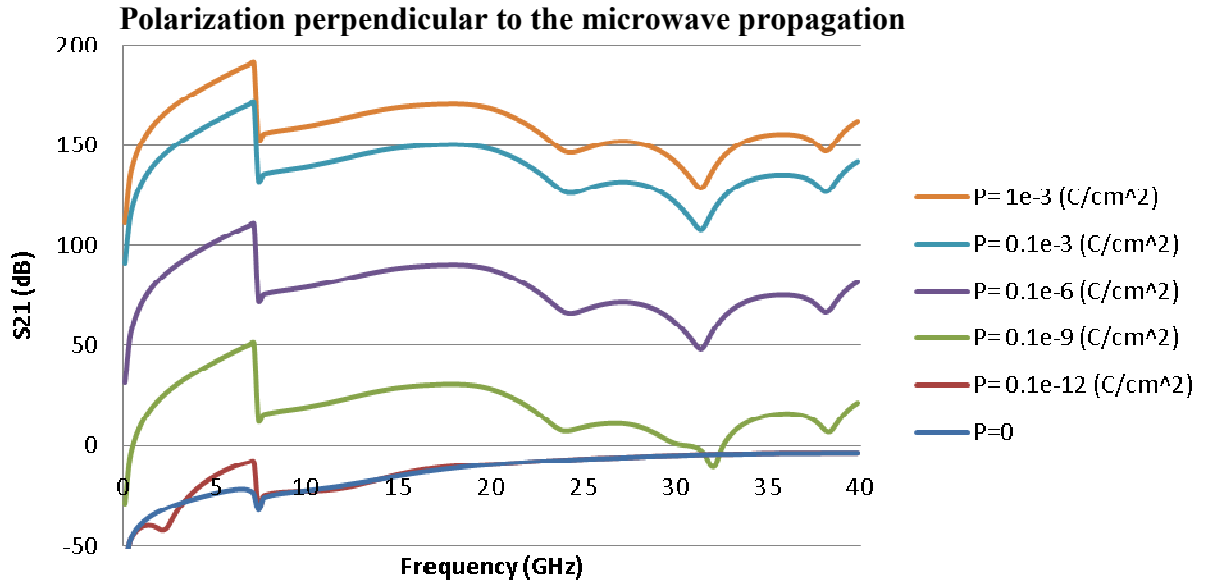


Figure 4.4 Transmission parameter as function of frequency in 4 periodically polarization-inverted elements

Figure 4.5 shows the polarization at 0.1 pC/cm² up to an artificially high value 1 C/cm² and how the response changes by varying the number of inverted polarization elements. When the polarization level is 0.1 pC/cm² even and odd number of elements show two groups of transmission behavior at below the 7.5 GHz cutoff frequency. When the polarization level is 0.1 nC/cm² different number of polarization-inverted elements has a significant change in response. The shape of the S₂₁ for the polarization level from 0.1 μC/cm² to 1 C/cm² are similar indicating the mechanisms are stable at the polarization level. Using 5 elements one obtains a large

transmitted wave response from 18 to 25GHz – indicating that transmission amplification over certain bands can be achieved by selecting the proper number of elements.

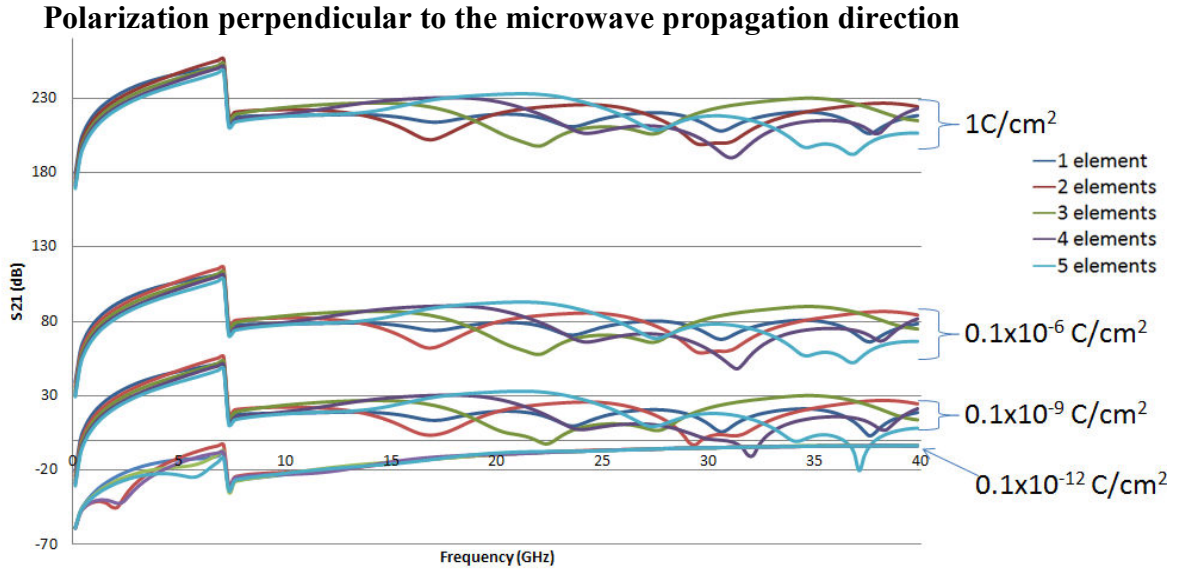


Figure 4.5 Transmission parameter as function of frequency and the number of periodically polarization-inverted elements

Figure 4.6 is a visual representation of the transverse component of the electric field on each boundary at 20GHz when the polarization is 0.1 nC/cm^2 (refer to Figure 4.3). In a dielectric waveguide the number of transverse electric modes along the z direction will increase with frequency but is in general dependent on the dimension, permittivity, and boundary conditions. However in the figure the only difference is the polarization with all other conditions being equal. The number of modes supported in the propagation direction tends to be the same as the number of polarization-inverted elements. The unpolarized waveguide has approximately four or five modes at 20 GHz so that modes close to this are more readily supported, that is the case for three, four, and five elements.

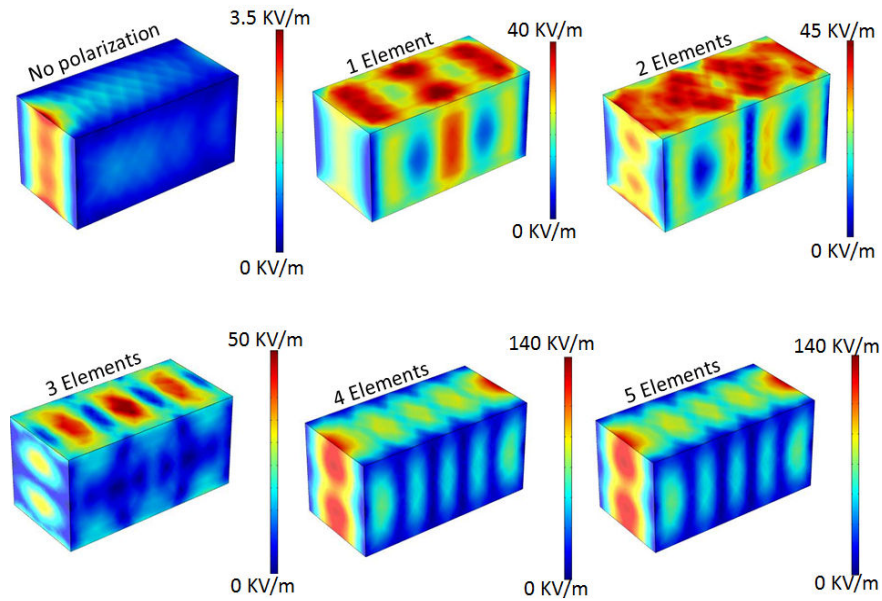


Figure 4.6 A surface plot of the transversal electric field strength at 20GHz ($P=0.1 \text{ nC/cm}^2$) that shows how the polarization-inverted sections tend to support transverse electric modes corresponding to the number of the elements

4.2.2 Comparison of gradient and step polarization, surfaces free from metallization

Most of our simulations used a periodically inverted polarization which simply changes direction but with the same magnitude throughout (like a square wave); however in the case of piezoresonance the periodic polarization change would be more sinusoidal in nature. For this reason we compare a periodical step polarization with a sinusoidal gradient polarization, both of which share the same maximum amplitude (yet the step polarization has an RMS polarization value 0.1 nC/cm^2 and the sinusoidal is 0.0707 nC/cm^2). From Figure 4.8 it is clear that below about 25GHz gradient polarization distribution is more effective in transmission amplification and the opposite is true above 25GHz; particularly at about 37 GHz gradient polarization can be seen with improved transmission

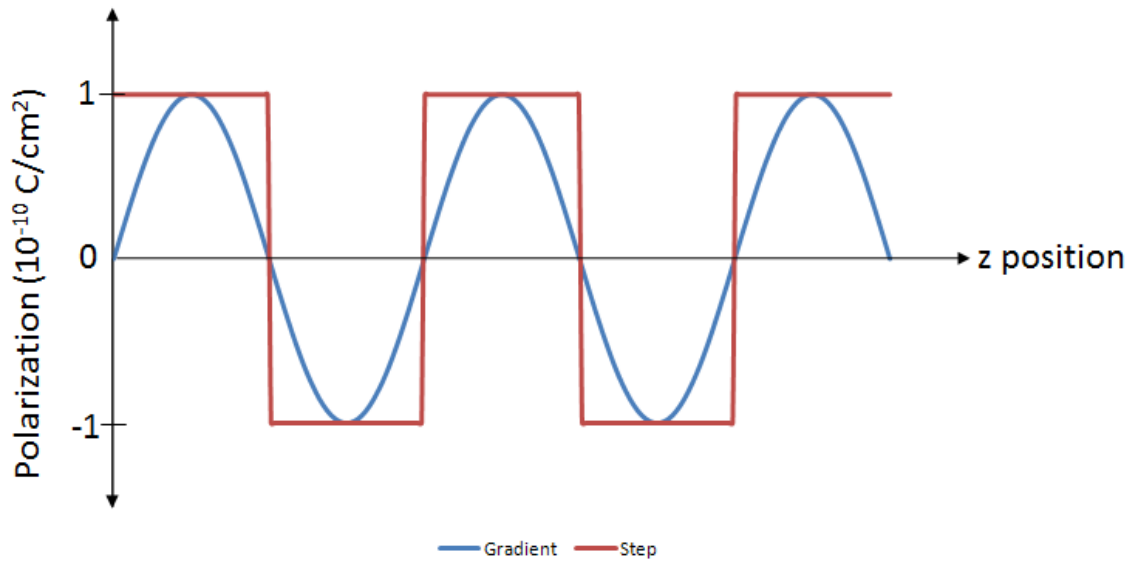


Figure 4.7 Gradient and step polarization in a 5 element cavity, both with magnitude 0.1 nC/cm^2

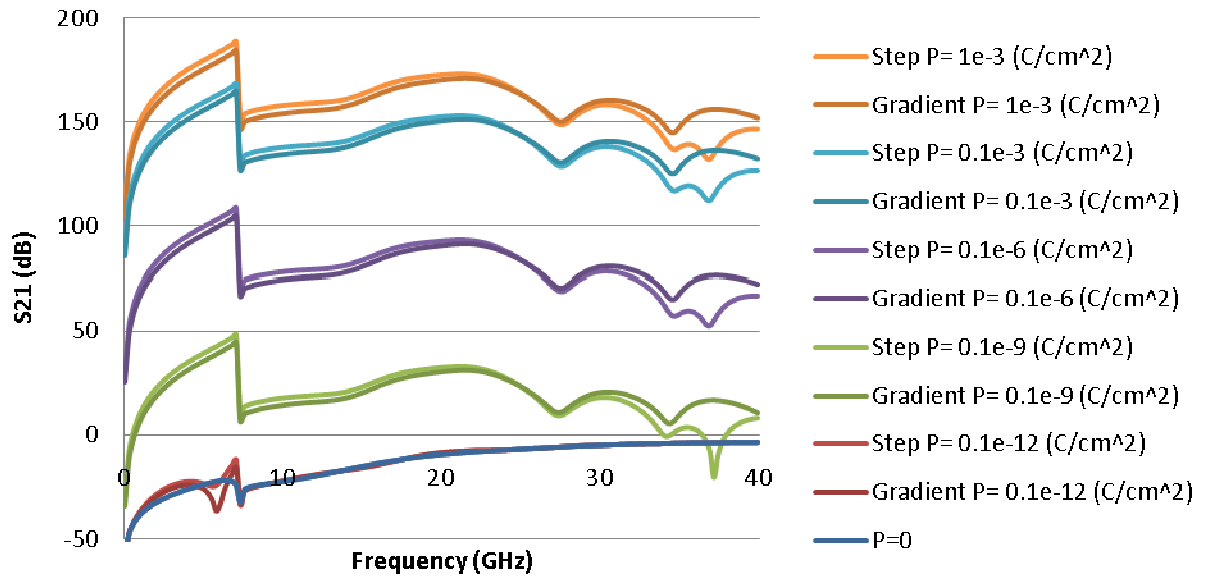


Figure 4.8 Comparison of sinusoidal and step polarization distribution in a polarization-inverted 5-element waveguide

4.2.3 Effect of the sequence of the polarization, surfaces free from metallization

Although unexpected, by changing the order of the +/- z-direction polarization the response does change slightly within the resolution of the simulation. The configuration is defined in Figure 4.9 using four elements. The sequence of the polarization makes almost no difference for large polarization (greater than or equal to $0.1 \mu\text{C}/\text{cm}^2$) at high frequencies; however at lower polarization the order can affect the low frequency response, as illustrated in Figure 4.10.

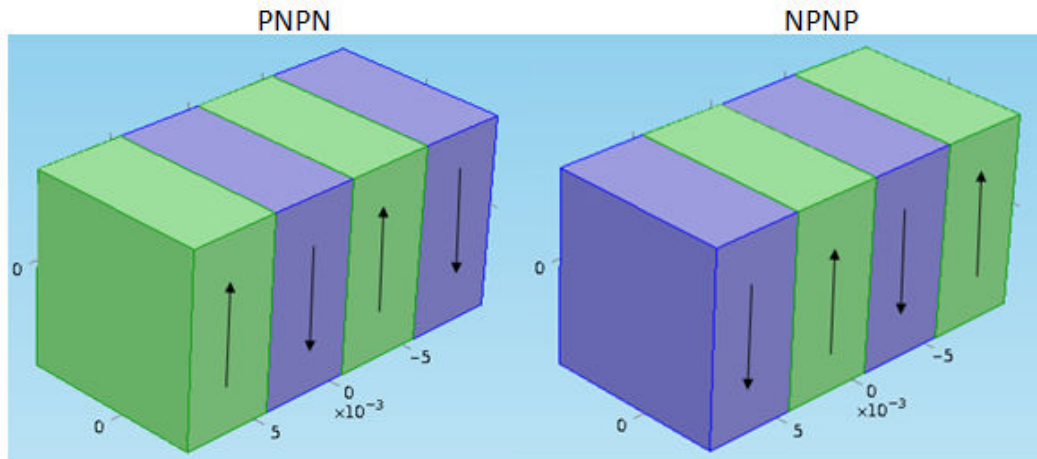


Figure 4.9 FEA model setup showing periodic poling configuration. “P” corresponds to polarization in the positive z direction and “N” in the negative z direction

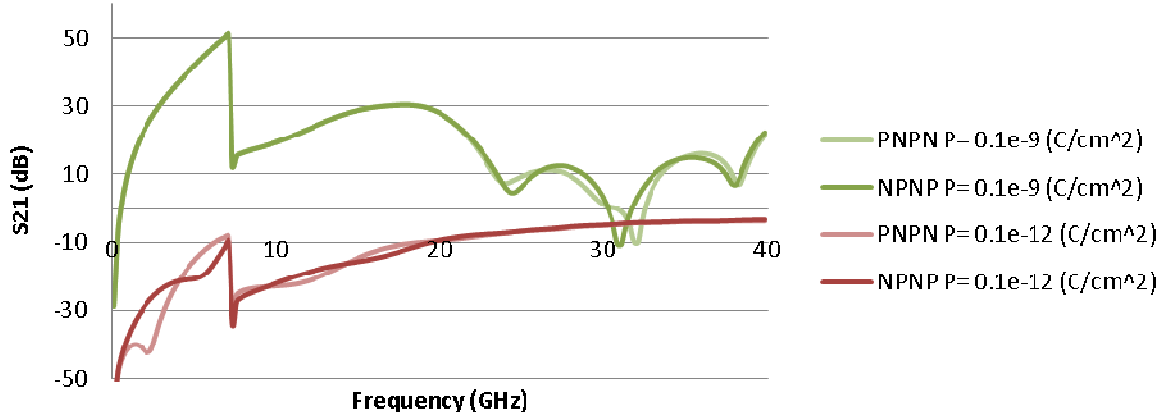


Figure 4.10 Transmission parameter as a function of frequency for 4 polarization-inverted elements while the order of antiparallel polarization can cause a significant shift in the response

4.2.4 Dielectric Waveguide with Top and Bottom Metallization

Piezoelectric resonators are typically electroded to allow the application of electrical signals. Simulation result with top and bottom boundaries of the waveguide as perfect electrical conductors (PECs) and the other two sides as scattering boundaries is shown in Figure 4.11. When the polarization is $\leq 0.1 \text{ pC/cm}^2$ the most significant changes in response due to periodically polarization-inverted elements is seen at below the cutoff frequency. When the polarization is 0.1 nC/cm^2 or higher the response is strongly dependent on the number of elements. The overall response of this condition is similar to the simulation results of metallization-free conditions, which indicates that the metallization does not screen the polarization effect under the given conditions. These results are consistent with results reported earlier [1, 3, 4, 6] where samples electroded in a similar manner displayed wave enhancement due to an induced periodic polarization.

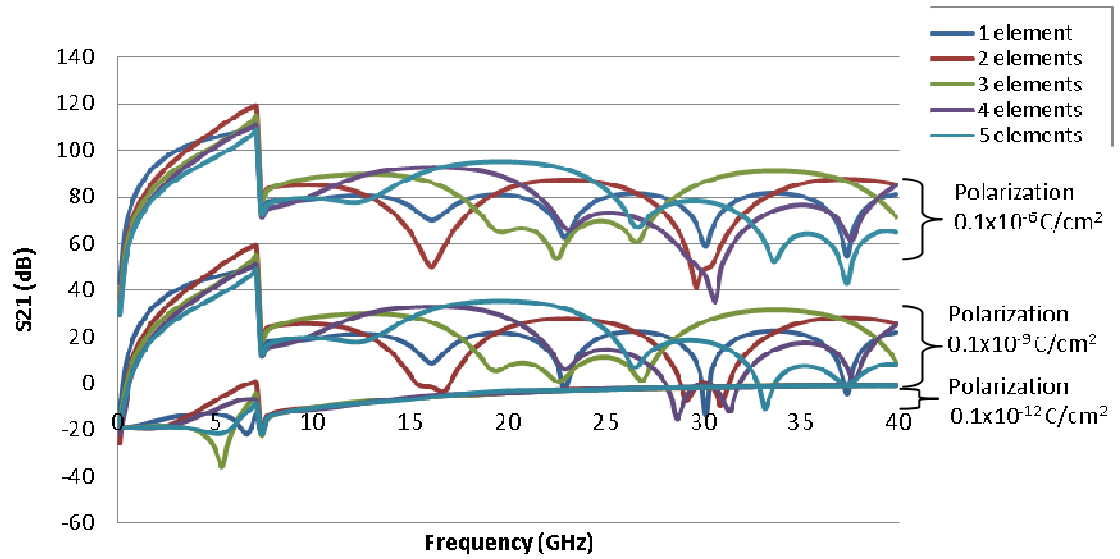


Figure 4.11 Transmission parameter as a function of frequency for a number of periodically polarization-inverted elements while electrodes and polarization are perpendicular to the microwave propagation direction

4.2.5 Polarization in line with wave propagation, surfaces free from metallization

Considered here is the effect of the polarization along the axis of wave propagation (Figure 4.12). When polarization is small it has little to no effect on the response – thus it is not shown here. As seen in Figure 4.13, little effect is seen when polarization is $<0.1 \text{ nC/cm}^2$ while it causes significant changes on low frequency response. Polarization of $0.1 \text{ } \mu\text{C/cm}^2$ and higher increases transmission significantly over a broad range (with exception at frequency near $\sim 16 \text{ GHz}$); however S_{21} is in general much lower compared to the situation where polarization is perpendicular to the wave propagation direction.

Figure 4.14 shows surface plots of the electric field strength at 20 GHz ($P_r = 0.1 \text{ } \mu\text{C/cm}^2$, $P_r/x\text{-axis}$) for the number of polarization-inverted elements from 0 to 5, while polarization is parallel to the microwave propagation direction. It appears that co-linear polarization both with

and against the microwave propagation has the effect of confining the guided microwave thus increases the transmission.

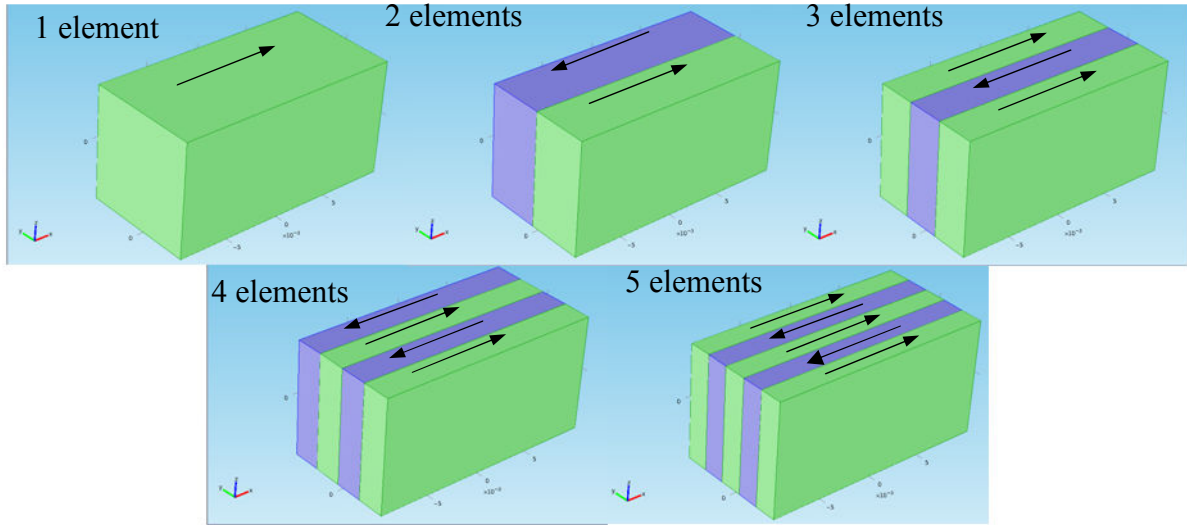


Figure 4.12 FEA microwave model setup of antiparallel polarization in the direction of propagation (positive x-axis) and against propagation (negative x-axis)

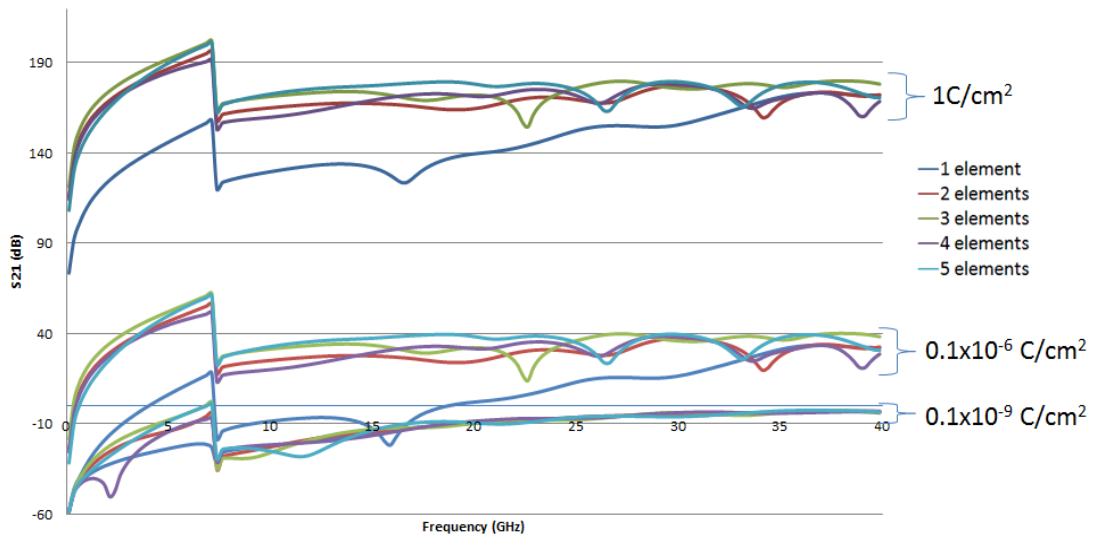


Figure 4.13 Transmission parameter as a function of frequency for a number of periodically polarization-inverted elements while polarization is parallel to the microwave propagation direction

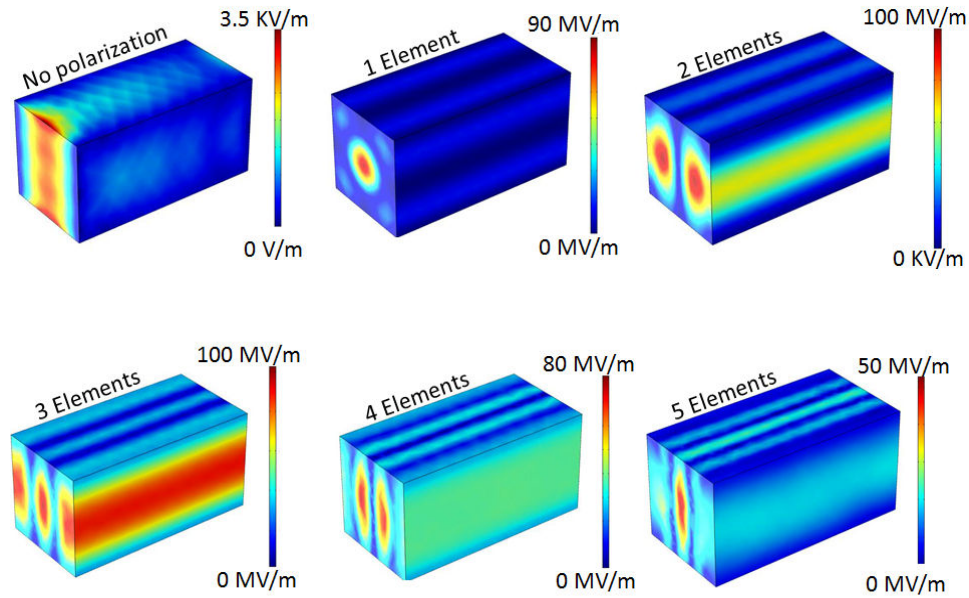


Figure 4.14 Surface plots of the electric field strength at 20 GHz ($\text{Pr}=0.1$ $\mu\text{C}/\text{cm}^2$, Pr/x -axis) for the number of polarization-inverted elements from 0 to 5, while polarization is parallel to the microwave propagation direction.

4.2.6 Polarization parallel (with) and antiparallel (against) propagation, surfaces free from metallization

Using one element and once again the effect of polarization with (parallel) and against (antiparallel) propagation is considered. The direction of polarization does affect the transmission parameter however the effect is appreciable in certain range of polarization magnitude (as seen in Figure 4.15, $1 \text{ nC}/\text{cm}^2$ to $1 \mu\text{C}/\text{cm}^2$). Respective plots of parallel and antiparallel polarizations $>1 \mu\text{C}/\text{cm}^2$ are on top of each other, indicating that above a certain threshold the polarization direction does not impede or enhance the transmission of the microwave.

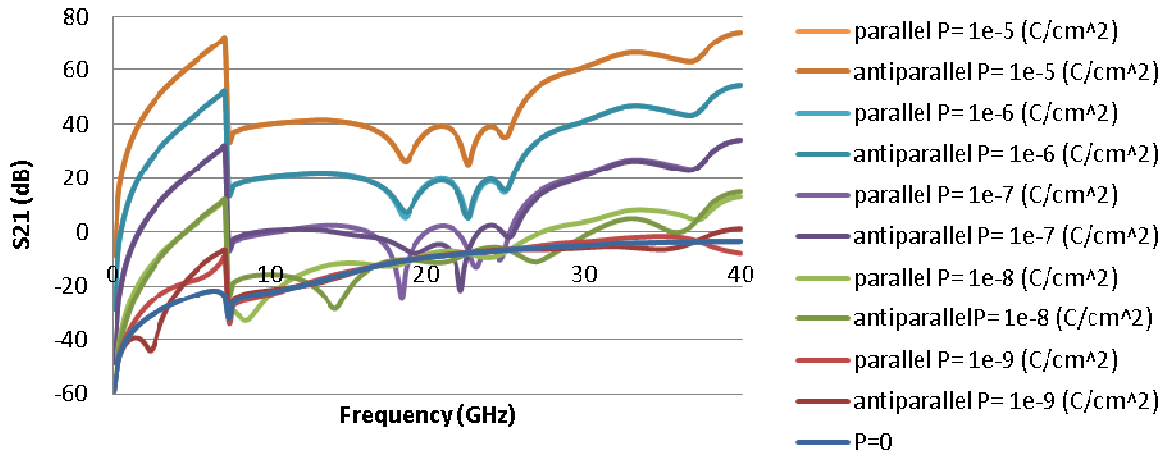


Figure 4.15 Transmission parameter as a function of frequency and magnitude of polarization for a single element with polarization parallel or antiparallel to the microwave propagation direction

4.2.7 Summary

Finite element analysis method is used to simulate microwave propagation behavior in terms of transmission parameter S_{21} , in a ferroelectric waveguide with periodic polarizations. The periodic polarization-inverted sections (elements) are generated either dynamically at given piezoelectric resonance frequencies or formed by patterned poling. Analytical solution for such nonlinear polarization-dependent system is not available and numerical method permits detailed study. The simulation is conducted for 1-40 GHz and for periodic polarization in transverse or longitudinal of the wave propagation directions. Model ferroelectric waveguides containing up to five polarization-inverted sections were simulated. It is verified that periodically poled structure in ferroelectric waveguide can contribute to a significantly enhanced transmission of microwave. At a given polarization magnitude, transmission amplification over certain bands can be achieved by selecting the proper number of elements. Metallization in transverse direction was found insignificant in screening the polarization effect; the simulated transmission

enhancement is much stronger for polarization in transverse, than in longitudinal, directions of the propagation wave.

It is noted that the simulation results are consistent with previous experimental results that apparent electro-optic coefficients or optical transmission are enhanced at frequencies related to piezoelectric resonance of certain modes. Further study will be useful to extend the simulation to optical wavelength and to include nonlinearity of dielectric properties in the simulation model.

4.3 Frequency Domain Piezoelectric Model

4.3.1 The Sample

The material used was $(1-x)\text{Pb}(\text{Zn}_{1/3}\text{Nb}_{2/3})\text{O}_3-(x)\text{PbTiO}_3$ where $x = 0.045$ (PZN-4.5%PT) which is a single crystal poled along $\langle 001 \rangle$. At room temperature this composition is rhombohedral, however after poling it is known to be pseudo-tetragonal (4mm symmetry)[18]. The sample is electrode on its (001) faces (Figure 4.16). The electrode area = $3.21 \text{ mm} \times 2.83 \text{ mm} = 9.0843 \times 10^{-6} \text{ m}^2$, thickness = $6.3 \times 10^{-3} \text{ m}$. The incident optical signal propagates along the y axis.

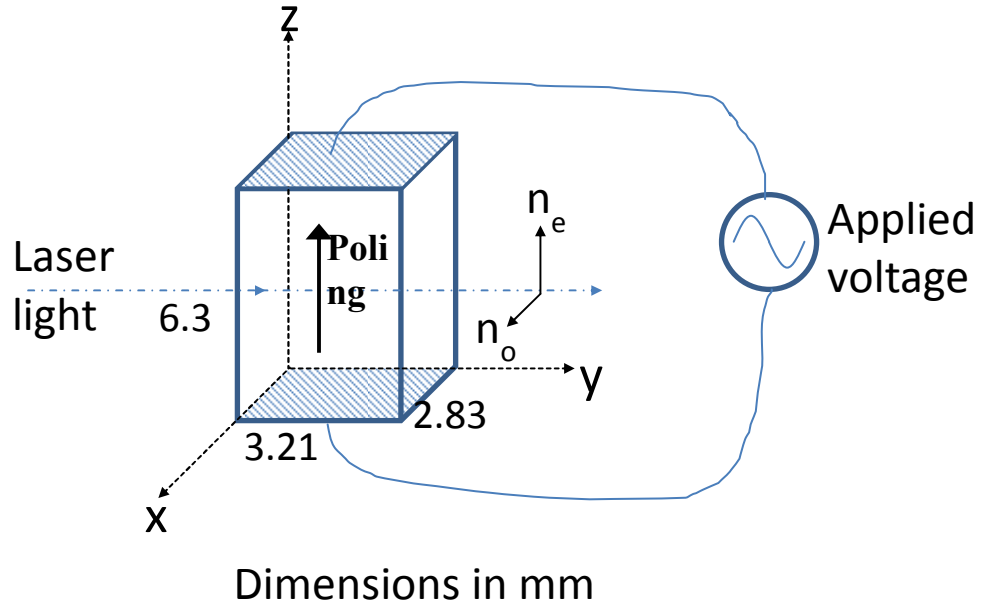


Figure 4.16 PMN-30%PT sample, poled in [001] direction. Electroded on top and bottom {001} surfaces of the x by y dimensions

4.3.2 The Piezoelectric Model

The piezoelectric model is used to identify the primary resonant modes of the sample and eventually when applied to the optical model to calculate the refractive index changes. Equation (1) is the partial differential equation used to describe the relationship between the density (ρ), angular frequency (ω), mechanical displacement (u) and stress (X) in the piezoelectric domain (for a time harmonic solver). Additionally in the domain, the divergence of the electric displacement (D) field is equal to the charge density (ρ_v). The electric field is equal to the gradient of the negated voltage and the strain (χ) is related to the mechanical displacement.

$$-\rho\omega^2u - \nabla \cdot X = F_v e^{j\phi} \quad (4.1)$$

$$\nabla \cdot D = \rho_v \quad (4.2)$$

$$E = -\nabla V \quad (4.3)$$

$$x = \frac{1}{2} \left[(\nabla u)^T + \nabla u \right] \quad (4.4)$$

This simulation uses the converse piezoelectric effect, meaning an applied electric field causes a change in the strain. In this case in equations (4.5) and (4.6) the Stress-charge form is used. Respectively the terms $X, c_E, \mathbf{x}, e, \epsilon_0, \epsilon_{rS}, \mathbf{D}_r$ are the stress, elasticity matrix, strain, coupling matrix, vacuum permittivity, relative permittivity, and remanent displacement field. The \mathbf{x}_i term is the initial stress in the material and is assume to be zero.

Stress-Charge form:

$$X = c_E (x - x_i) - e^T E + X \quad (4.5)$$

$$D = e(x - x_i) - \epsilon_0 \epsilon_{rS} E + D_r \quad (4.6)$$

The pertinent material parameters for a piezoelectric material with 4mm symmetry are shown in Equation (4.7). The symmetry is applied to the elasticity matrix (c_{ij}), the piezoelectric coupling matrix (e_{ij}) and the permittivity matrix (ϵ_{ij}).

Table 4.1 Shows the material parameters used in the piezoelectric simulation. Literature values are from Zhang *et al.*[19]

$$c_{ij} = \begin{bmatrix} c_{11} & c_{12} & c_{13} & 0 & 0 & 0 \\ c_{12} & c_{11} & c_{13} & 0 & 0 & 0 \\ c_{13} & c_{13} & c_{33} & 0 & 0 & 0 \\ 0 & 0 & 0 & c_{44} & 0 & 0 \\ 0 & 0 & 0 & 0 & c_{44} & 0 \\ 0 & 0 & 0 & 0 & 0 & c_{66} \end{bmatrix} \quad e_{ij} = \begin{bmatrix} 0 & 0 & 0 & 0 & e_{15} & 0 \\ 0 & 0 & 0 & e_{15} & 0 & 0 \\ e_{31} & e_{31} & e_{33} & 0 & 0 & 0 \end{bmatrix} \quad \epsilon_{ij} = \begin{bmatrix} \epsilon'_{11} - j\epsilon'' & 0 & 0 \\ 0 & \epsilon'_{11} - j\epsilon'' & 0 \\ 0 & 0 & \epsilon'_{33} - j\epsilon'' \end{bmatrix} \quad (4.7)$$

Table 4.1 Electrical and mechanical material parameters of the samples

Elasticity (@ constant E-field) [N/m ²]*	Coupling matrix [C/m ²]*	Permittivity (@ constant temperature)*	Density [kg/m ³]*
c ₁₁ =11.7x10 ¹⁰	e ₁₅ =13.6	ε' ₁₁ = 3307	8038.4
c ₁₂ =10.3x10 ¹⁰	e ₃₁ =-2.4	ε' ₃₃ = 1242	
c ₁₃ =10.1x10 ¹⁰	e ₃₃ =27.1		
c ₃₃ =10.8x10 ¹⁰		ε'' = 1	
c ₄₄ =7.1x10 ¹⁰			
c ₆₆ =6.6x10 ¹⁰			
*Reported values for the Elasticity, coupling, real permittivity, and density are from Zhang <i>et al.</i> The imaginary permittivity is a measured values for this sample.			

A 0.5 volt AC source is used to excite the sample and the bottom domain is grounded. The remaining four boundaries are all under zero charge condition. The crystal is completely unconstrained on all boundaries, edges and points. In order to calculate the response of the electrical conductivity the real (I_r) and imaginary (I_i) parts of the current were integrated over the surface of the top boundary (the boundary of the electrode). Using these values and combining with the applied AC voltage (V_{app}=0.5) gives the conductance (G) in equation (4.8) and susceptance in (B) equation (9). Then the Magnitude of the admittance can easily be calculated in equation (10) and the phase angle in equation (4.11)

$$G = I_r / V_{app} \quad (4.8)$$

$$B = I_i / V_{app} \quad (4.9)$$

$$|Y| = \sqrt{G^2 + B^2} \quad (4.10)$$

$$Phase = \tan^{-1}(B/G) \quad (4.11)$$

The results of the admittance calculation are shown in Figure 4.17, resonance frequencies are indicated by peaks in the $|Y|$ and minimums indicate anti resonate frequencies. Additionally the sample was also tested experimentally and a comparison is show in Figure 4.18. The response does not line up well however the amplitudes are on a comparable scale and tests/simulations on similar compositions of higher dimensional aspect ratio have shown extremely close agreement.

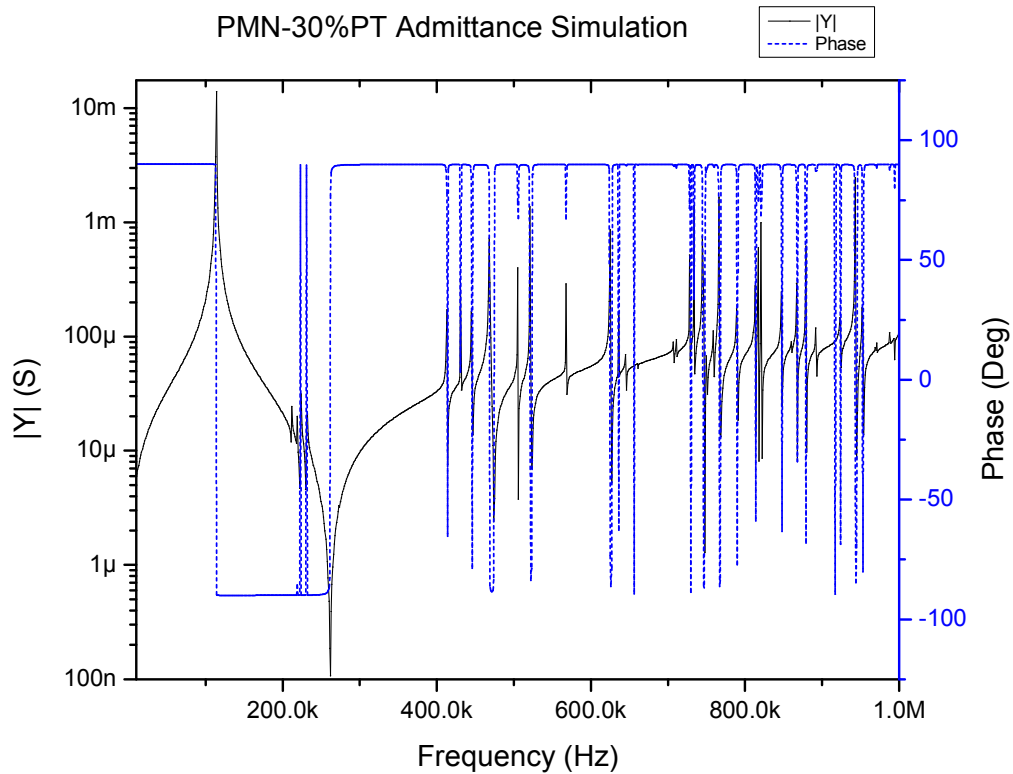


Figure 4.17 Simulation of Admittance magnitude $|Y|$ in Siemens and the phase angle in degrees over frequency range encompassing the piezoelectric vibrational frequencies below 1 MHz

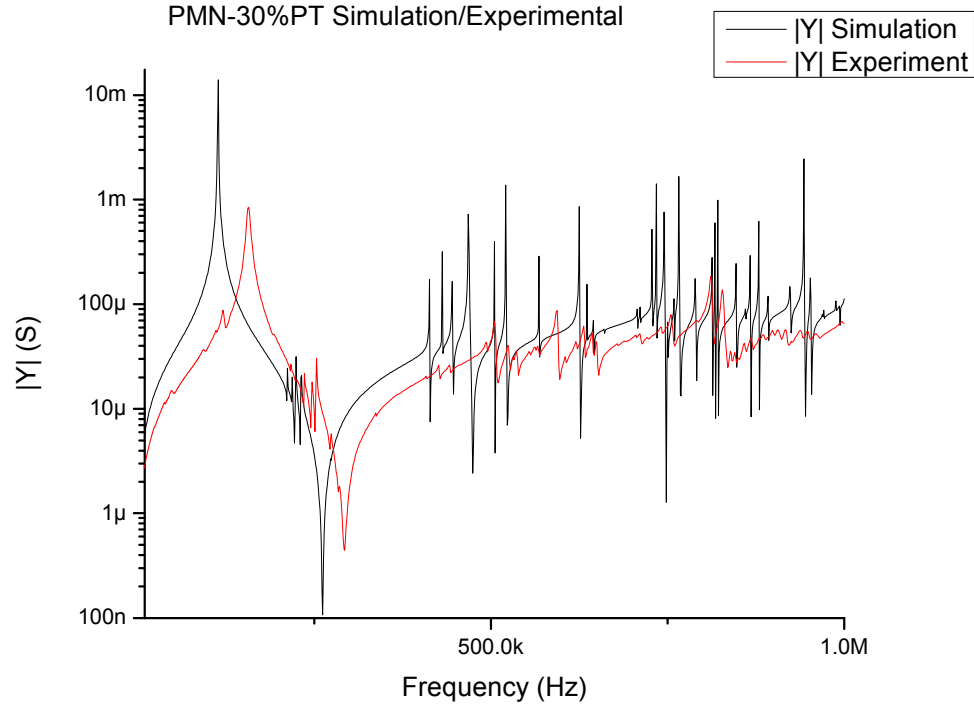


Figure 4.18 Comparison of the simulation and experimental results of the admittance frequency spectrum of PMN-30%PT

4.3.3 Frequency Domain Optical Model

The optical model consists of two parts one being a three dimensional model identical to the piezoelectric model described above and the other being a two dimensional model used to compute the transmission parameters of the optical transmission through the center of the piezoelectric crystal (See Figure 4.19). Linear extrusion coupling variables are used to map the refractive index changes from the 3D to the 2D model

This model uses a slightly different sample, with electrode area of 2.26 mm x 2.52 mm=5.6952 x10⁻⁶ m², and thickness=2.05x10⁻³ m. This sample is PZN-4.5%PT and possesses the same pseudo tetragonal 4mm symmetry as the previous sample but with higher opacity lending itself well to optical testing.

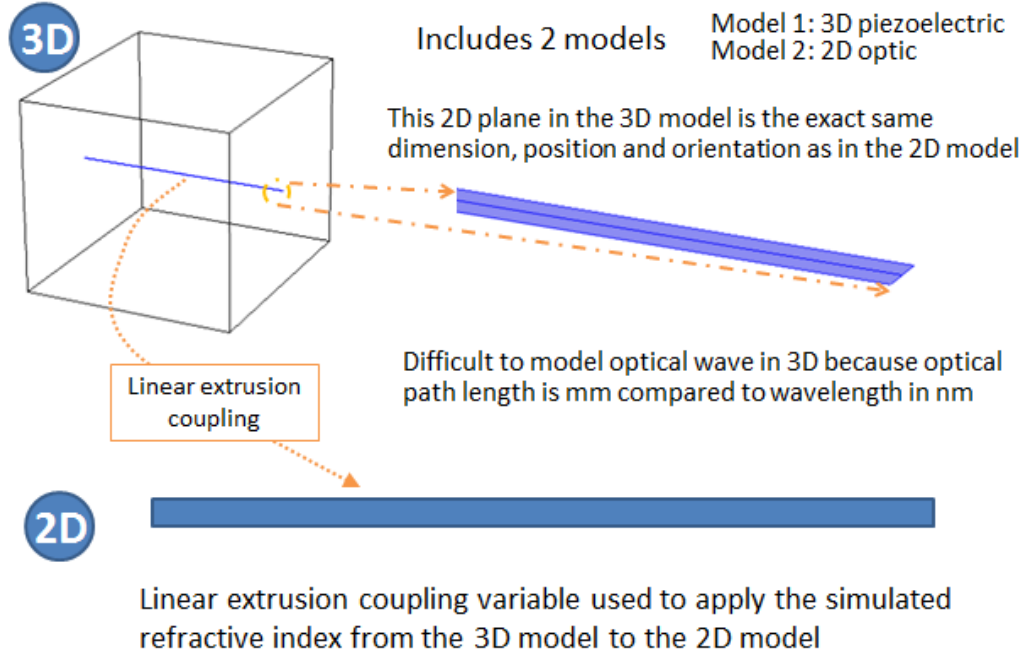


Figure 4.19 Illustration of the finite element optical model that includes two sub models to handle the coupling between piezoelectric and optical interaction

The Optical model is rectangular with the longer dimensions being the direction of wave propagation (y-axis). The side boundaries are perfect magnetic conductors allowing plain wave propagation. The end boundaries are ports, one port is the output and the other is used to launch a 5mW wave polarized in the x and z directions (transverse to propagation). The Propagation constant is $\beta = (2\pi) / (3 \times 10^8 [\text{m/s}] / 2.857 \times 10^{14} [\text{Hz}])$, where $2.857 \times 10^{14} \text{ Hz}$ is the frequency of a 1050 nm wave in free space. The partial differential equation applied to the domain is:

$$\nabla \times \mu_r^{-1} (\nabla \times E) - k_0^2 \left(\epsilon_r - \frac{j\sigma}{\omega\epsilon_0} \right) E = 0 \quad (4.12)$$

Where μ_r , ϵ_r , ϵ_0 , k_0 , σ , ω , E are respectively the vacuum permeability, relative permittivity, vacuum permittivity, free space wave number, conductivity, angular frequency and the electric field. The refractive index changes due to the applied electric field and the shape changes of the piezoelectric sample are modeled by way of the electro-optic and elasto-optic

effects respectively. The electro-optic effect is the change of the refractive index due to an applied electric field (E) and at constant strain (the clamped condition) is represented by r^x the elasto-optic effect is the change in refractive index due to a strain (x) and is represented by p. Combining these effects and defining in tensor form the impermeability tensor B_{ij} is:

$$\Delta B_{ij} = r_{ijk}^x E_k + p_{ijkl} x_{kl} \quad (4.13)$$

ΔB_{ij} can be defined in terms of the refractive index with zero applied field and zero stress (n_{ij}) and the new refractive index n'_{ij}

$$\Delta B_{ij} = \Delta \left(\frac{1}{n_{ij}^2} \right) = \left(\frac{1}{n'_{ij}} \right)^2 - \left(\frac{1}{n_{ij}} \right)^2 \quad (4.14)$$

By combining equations (4.13) and (4.14), converting to matrix form and applying 4mm symmetry the matrix for the six independent refractive indices is:

$$\begin{bmatrix} \left(\frac{1}{n'_{11}} \right)^2 \\ \left(\frac{1}{n'_{22}} \right)^2 \\ \left(\frac{1}{n'_{33}} \right)^2 \\ \left(\frac{1}{n'_{23}} \right)^2 \\ \left(\frac{1}{n'_{31}} \right)^2 \\ \left(\frac{1}{n'_{12}} \right)^2 \end{bmatrix} = \begin{bmatrix} \left(\frac{1}{n_{11}} \right)^2 \\ \left(\frac{1}{n_{22}} \right)^2 \\ \left(\frac{1}{n_{33}} \right)^2 \\ \left(\frac{1}{n_{23}} \right)^2 \\ \left(\frac{1}{n_{31}} \right)^2 \\ \left(\frac{1}{n_{12}} \right)^2 \end{bmatrix} + \begin{bmatrix} 0 & 0 & r_{13} \\ 0 & 0 & r_{13} \\ 0 & 0 & r_{33} \\ 0 & r_{51} & 0 \\ r_{51} & 0 & 0 \\ 0 & 0 & 0 \end{bmatrix} \begin{bmatrix} E_1 \\ E_2 \\ E_3 \end{bmatrix} + \begin{bmatrix} p_{11} & p_{12} & p_{13} & 0 & 0 & 0 \\ p_{12} & p_{11} & p_{13} & 0 & 0 & 0 \\ p_{31} & p_{31} & p_{33} & 0 & 0 & 0 \\ 0 & 0 & 0 & p_{44} & 0 & 0 \\ 0 & 0 & 0 & 0 & p_{44} & 0 \\ 0 & 0 & 0 & 0 & 0 & p_{66} \end{bmatrix} \begin{bmatrix} x_{11} \\ x_{22} \\ x_{33} \\ x_{23} \\ x_{31} \\ x_{12} \end{bmatrix} \quad (4.15)$$

Simplifying gives the following equation which is applied to the COMSOL model to fully describe the coupling of the refractive index values between the piezoelectric to the optical models.

$$\begin{aligned}
n'_{11} &= 1 / \sqrt{\frac{1}{n_{11}^2} + r_{13}E_3 + p_{11}x_{11} + p_{12}x_{22} + p_{13}x_{33}} \\
n'_{22} &= 1 / \sqrt{\frac{1}{n_{22}^2} + r_{13}E_3 + p_{12}x_{11} + p_{11}x_{22} + p_{13}x_{33}} \\
n'_{33} &= 1 / \sqrt{\frac{1}{n_{33}^2} + r_{33}E_3 + p_{31}x_{11} + p_{31}x_{22} + p_{33}x_{33}} \\
n'_{23} &= 1 / \sqrt{r_{51}E_2 + p_{44}x_{23}} \\
n'_{31} &= 1 / \sqrt{r_{51}E_1 + p_{44}x_{31}} \\
n'_{12} &= 1 / \sqrt{p_{66}x_{12}}
\end{aligned} \tag{4.16}$$

The elasto-optic, electro-optic and refractive indices for the material were taken from the literature and are listed in Table 4.2. The refractive indices and elcto optic coefficients are actually for a similar composition (PZN-12%PT). The elasto optic coefficients are for PZN-PT and where actually converted from the piezo optic coefficients in the literature with the equation

$$p_{mn} = \pi_{mp} c_{pn}.$$

Table 4.2 Optical parameters for PZN-PT

Refractive indices*		Elasto optic coefficients [#]	
ne	2.57	p ₁₁	0.0888
no	2.46	p ₁₂	0.0816
		p ₁₃	0.0808
Electro-optic coefficients*		p ₃₁	-1.032
r ₁₃	7 pm/V	P ₃₃	1.911
r ₃₃	134 pm/V	p ₄₄	0
r ₅₁	462 pm/V	p ₆₆	0

* from Lu *et al.* [16]

[#] from Lu *et al.* [15]

The results of the optical field simulation can be seen in Figure 4.20 below. The plane wave propagates along the entire length of the sample domain. The launched wave is 1050 nm in free space but for a refractive index of about 2.5 the wave is 420 nm in the material – this confirms that the meshing on the domain is dense enough to represent the wave.

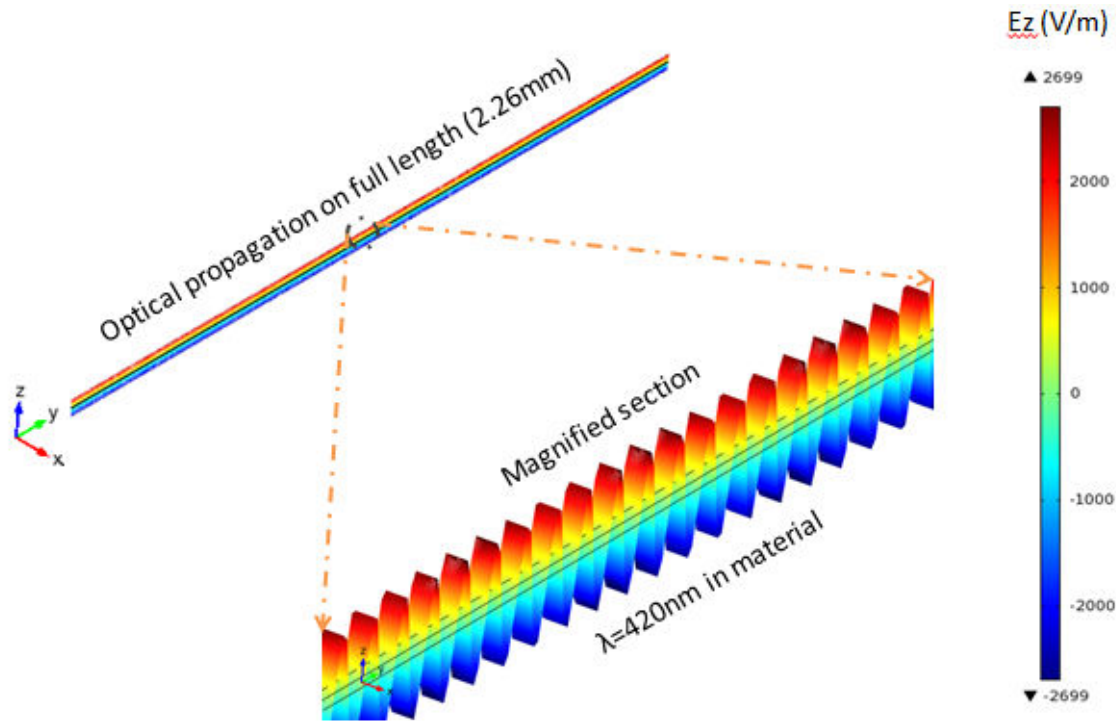


Figure 4.20 Simulation results of the optical plane wave propagating in the y direction and a plot of the electric field (E_z) in the transverse z direction

In Figure 4.21 the transmission of the optical signal using the transmission parameter S_{21} is shown with the admittance simulation. The figure clearly shows an increase the transmission near the resonant frequencies, typically the transmission follows the slope of the admittance magnitude and is quite consistent with typical experimental results for a sample near the resonant frequencies[1].

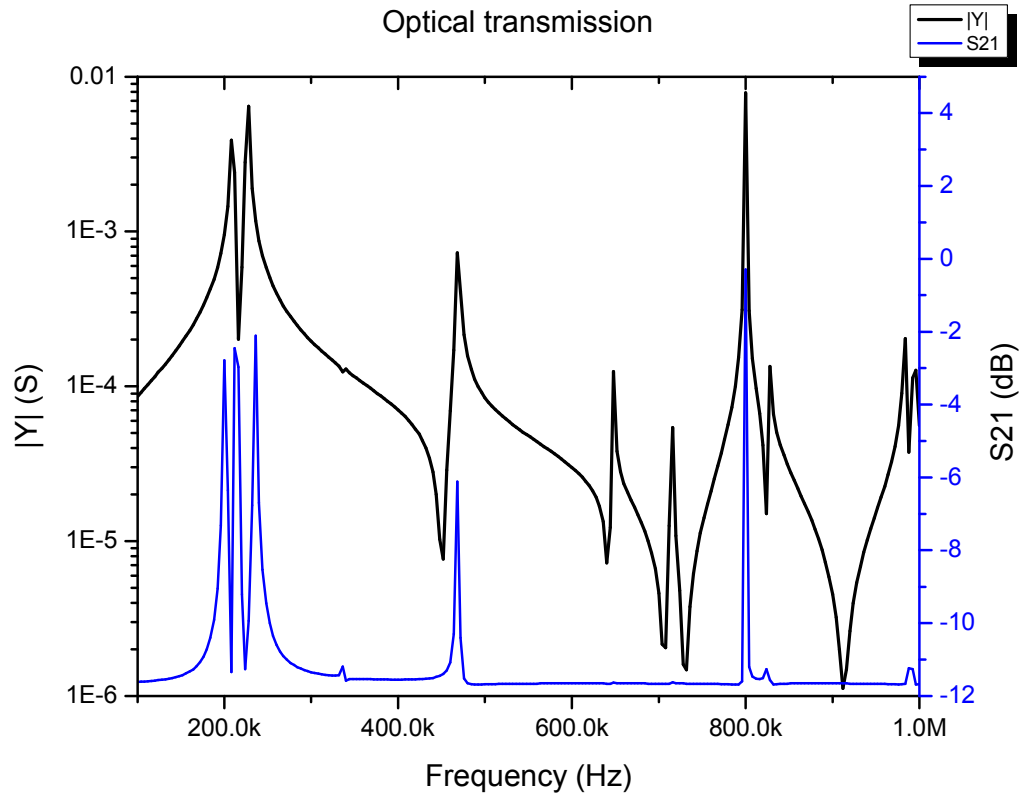


Figure 4.21 Simulation results of the frequency response of the optical response over a range of low frequency resonant modes showing strong correlation with the slope of the electrical admittance

At resonance the current field inside the material becomes periodic and leads to an induced polarization change inside the sample at integer multiples of the fundamental resonate modes. As proposed by Johnson *et al.* [4] it is this periodically changing field that has a large influence on the transmission and our model of the combined influence of the electro-optic and elasto-optic shows these effects. As illustrated in Figure 4.22 the current under certain resonant modes (in this case at 215 kHz) promotes a refractive index gradient that is sufficient to cause a large increase in transmission magnitude. Both acoustic and optical phonons can exist in the crystal. Polarization is present in the transverse optical phonons (TO) which couples with the displacive

current. When at resonance the TO modes become periodic and result in a complete circuit of current flow in the local field.

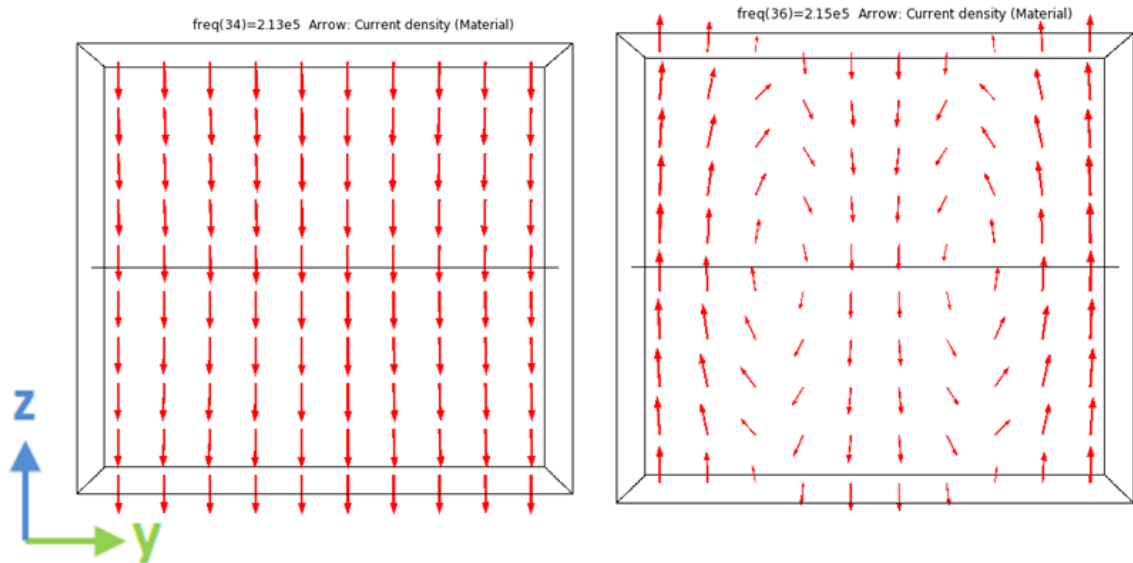


Figure 4.22 Current density distribution in the sample; off piezoelectric resonance at 213 KHz (Left) and near piezoelectric resonance at 215 KHz (Right).

At certain resonance modes the current becomes periodic and leads to an induced changing charge distribution. At resonance more of the current is co-propagating with the optical wave and enhancement is observed. The y-axis is the direction of propagation and z-axis the wave polarization direction

It has been shown that under certain conditions of piezoelectric resonance the optical response of the material can be tuned. Experimental results on electro optic crystals show high correlation between crystal vibrational modes and electro optical transmission signal. A COMSOL model was developed to describe the low frequency crystal admittance response, the combined effects of electro-optic and elasto-optics and transmission of an optical wavelength plane wave. The COMSOL model is in good agreement with experimental results for both vibration modes and optical response. Previously proposed models used to explain the influence

of bound charge distribution on wave transmission have been given further credence by multiphysics modeling of the electric displacement current influence on the propagating optical wave.

At resonance by definition the impedance of the sample is at a minimum, meaning with when using a voltage source there is a large influx of current at resonance and conversely a large impedance at anti-resonance gives a very low current.

4.4 Frequency Domain Piezoelectric Model – High Aspect Ratio

Section 4.3 modeled a real piezoelectric sample that had a geometry similar to a cube. Due to this low aspect ratio between the dimensions individual vibrating modes are not pure. To observe these modes a high aspect ratio bar of PMN-30%PT was modeled. The sample was configured with its x and y dimension electroded giving it an area of 20 x 2 mm² and a thickness of 0.5mm. This is a typical configuration for a k_{31} bar. The sample parameters are listed in the table below.

Table 4.3 Sample electrical and mechanical material parameters from [20]

Compliance (@ constant E-filed) 10 ⁻¹² [m ^{2/N}]	Coupling matrix 10 ⁻¹² [CN]*	Permittivity (@ constant temperature)	Density [kg/m ³]
$s_{11}= 52$	$d_{15}= 190$	$\varepsilon'_{11} = 3600$	8040
$s_{12}= -18.9$	$d_{31}= -921$	$\varepsilon'_{33} = 7800$	
$s_{13}= -31.1$	$d_{33}= 1918$		
$s_{33}= 67.7$			
$s_{44}= 14.0$			
$s_{66}= 15.2$			

The approximate resonate frequency and harmonics of the bar can be calculated from equation (3.1), they are summarized in Table 4.4. Figure 4.23 shows the response of the admittance magnitude and phase angle frequency spectrum. The figure shows the fundamental resonance at 38.750 KHz and harmonics at 115.250, 189.750 KHz. The harmonics are easily

identified because they are successive odd multiples of the fundamental i.e. $38.75 \text{ KHz} * 3 = 116.25 \text{ KHz}$, $38.75 \text{ KHz} * 5 = 193.75 \text{ KHz}$, $38.75 \text{ KHz} * 7 = 271.25 \text{ KHz}$. The slight deviation from this trend is due to a mixing of resonance mode vibration with other vibration directions. As compared in Table 4.4 the simulation and calculated values agree well. There are also anti-resonance frequencies associated with each resonance that are a slightly higher in frequency. By using the fundamental resonant frequency as $f_m = 38.75 \text{ KHz}$ and anti-resonance at $f_n = 43.0 \text{ KHz}$ the coupling coefficient k_{31} can be calculated from Equation (3.8) Using these values $k_{31} = 0.482$ and calculating directly from the material parameters gives $k_{31} = 0.486$ which matches very well.

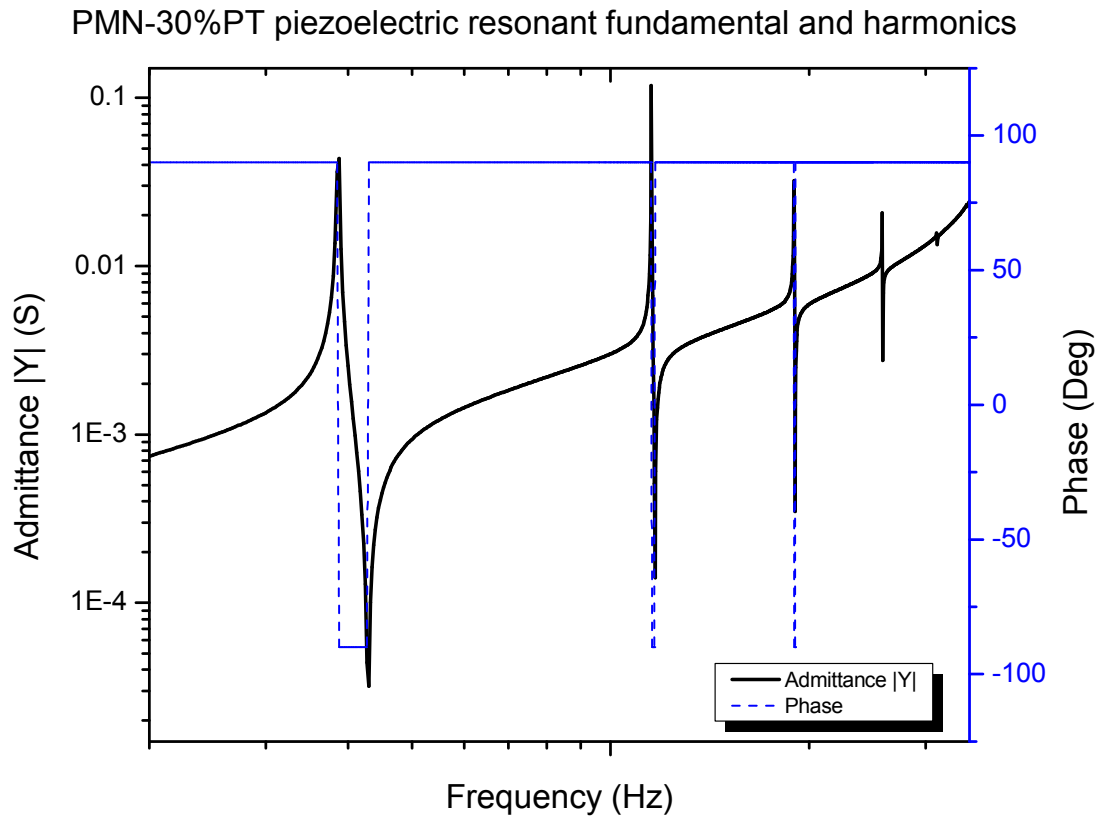


Figure 4.23 Admittance frequency spectrum of typical piezoelectric resonator showing resonance and anti-resonance frequencies of fundamental and harmonics

Table 4.4 Comparison of the piezoelectric resonate frequencies: calculated using a formula and derived by finite element analysis

n	Formula (KHz)	COMSOL FEA (KHz)
1	38.664	38.750
3	115.993	115.250
5	193.322	189.750

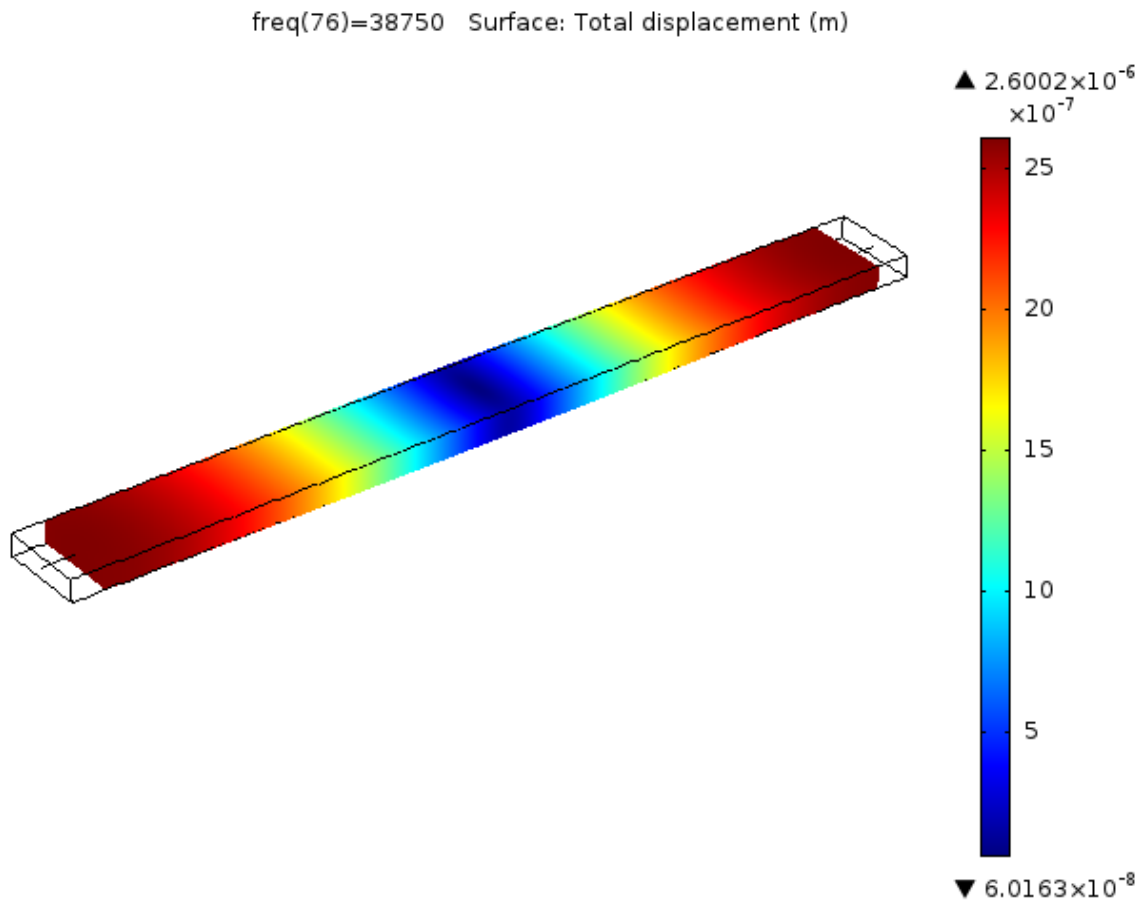


Figure 4.24 Total displacement of simulated PMN-30%PT k_{31} bar at fundamental resonant frequency 38.750 KHz

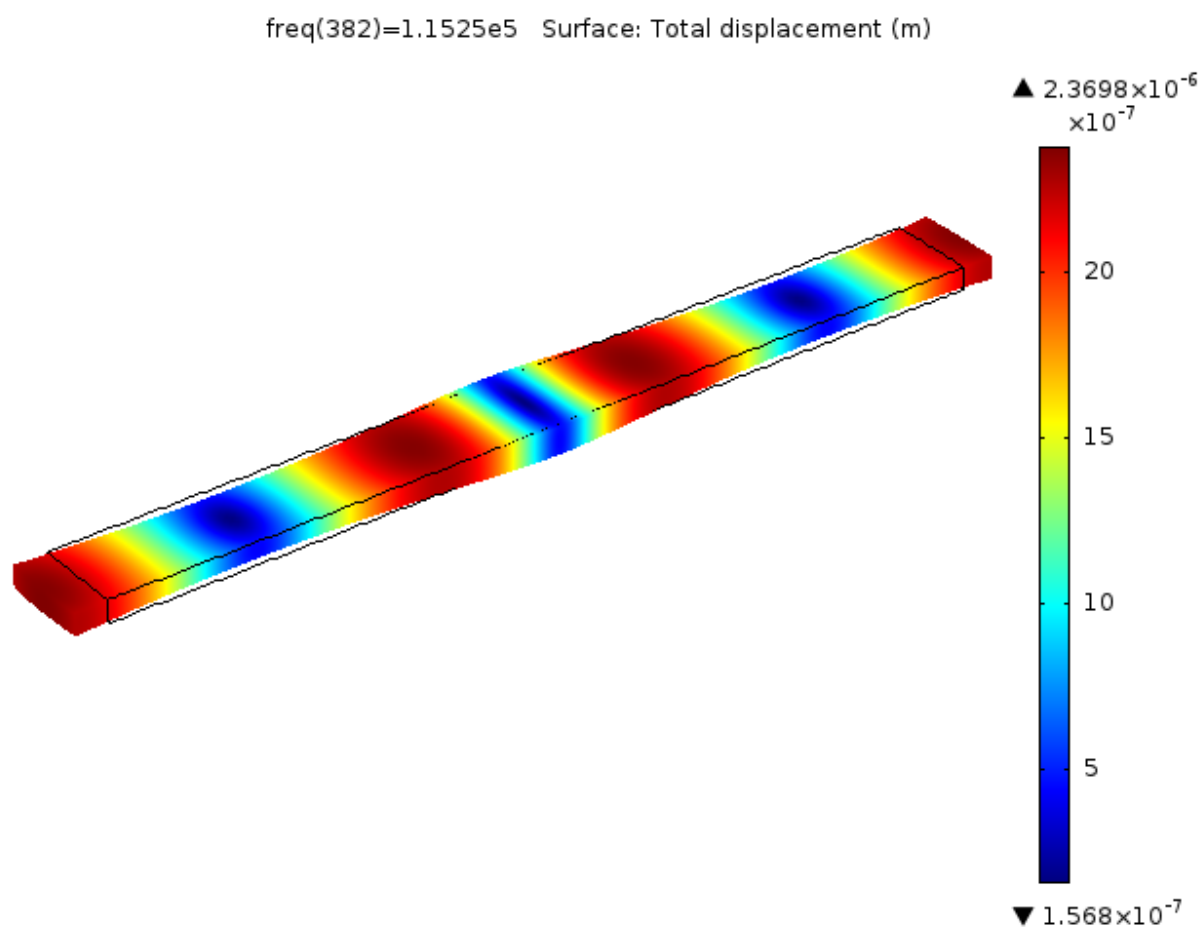


Figure 4.25 Total displacement of simulated PMN-30%PT k_{31} bar at 2nd harmonic of resonant frequency 115.250 KHz

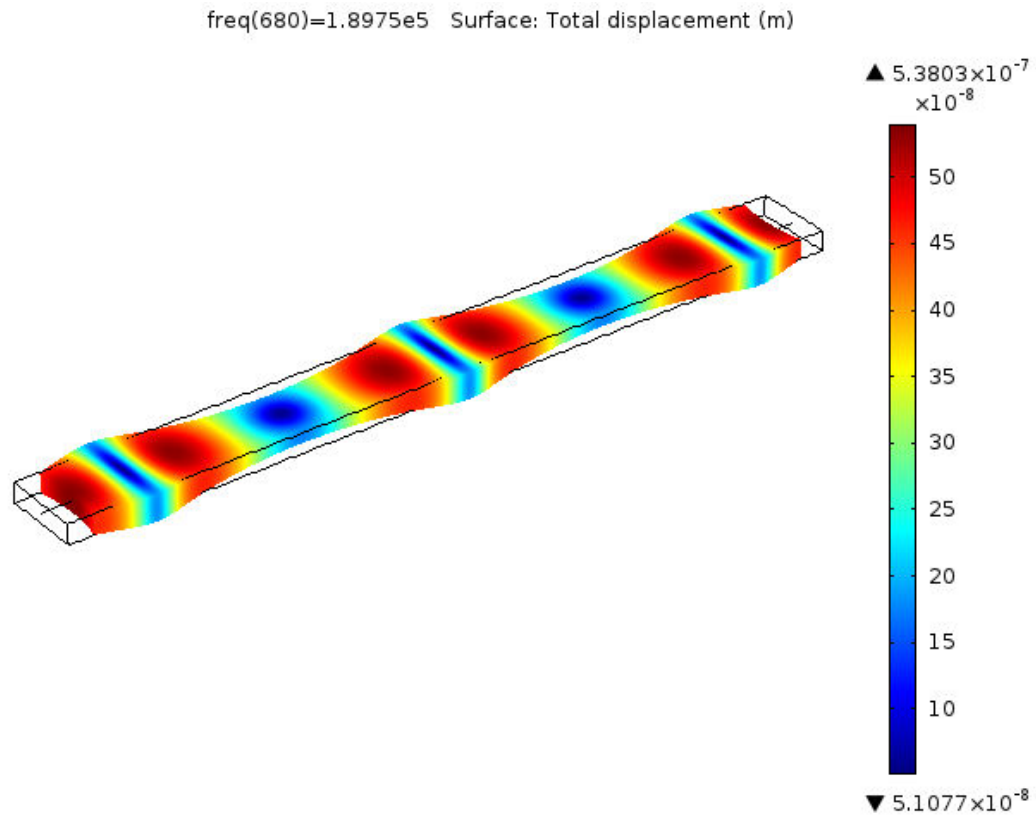


Figure 4.26 Total displacement of simulated PMN-30%PT k_{31} bar at 3rd harmonic of resonant frequency 189.750 KHz

4.4.1 Summary

The plots in Figure 4.24, Figure 4.25, and Figure 4.26 are each dual graphs of the physical shape change and the total displacement. The physical shape is an exaggerated representation of the sample geometry under sinusoidal modulation at the specified frequency. The total displacement is indicated the by the color on the color legend and is in meters. The total displacement is the distance from any given point on the non-modulated sample to the new point with the applied signal. It is clear from the figures that the modes are longitudinal and that higher frequencies will increase the nodal points. Using this model in COMSOL multiphysics results in reliable prediction of the resonate modes.

4.5 Time Domain Piezoelectric model

In order to model AC biasing of the EOM and get a full view of its response it is necessary to model the system in the time domain which brings its own set of challenges. This model uses only the COMSOL piezoelectric application mode to determine the phase shift due to the induced Birefringence of the device. The optical propagation through the device is not modeled here because of the extremely large computational cost. The model is setup as illustrated in the below figure. The sample modeled in PZN-4.5%PT with electroded on the xy faces with the assumed optical path along the y axis. Two sinusoidal voltage sources are used. V_{signal} is swept over a range of frequencies but V_{bias} is set to one constant frequency.

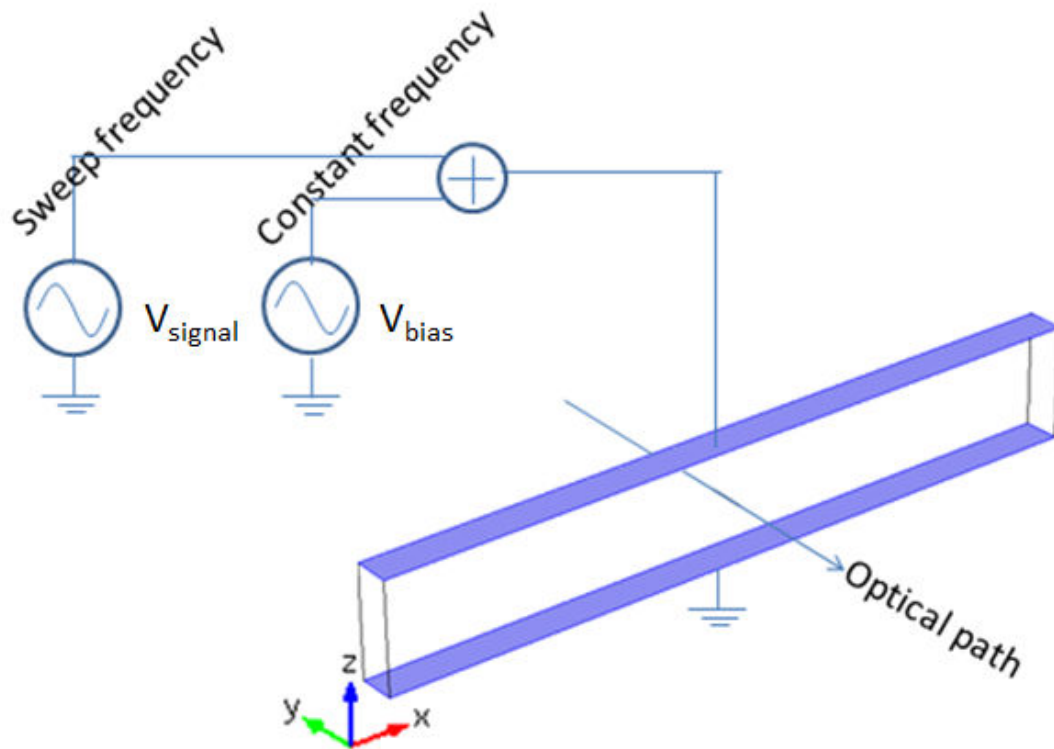


Figure 4.15 Schematic setup of dual frequency (piezo-resonant ac biased) electro-optic modulator simulation

The refractive index changes are calculated in the same manner as the frequency domain. The phase change due to the induced birefringence is calculated by first finding the average refractive index in the z direction along the optical path through the very center of the sample. This average index value can then be compared to the results with no applied voltage to find the induced phase shift.

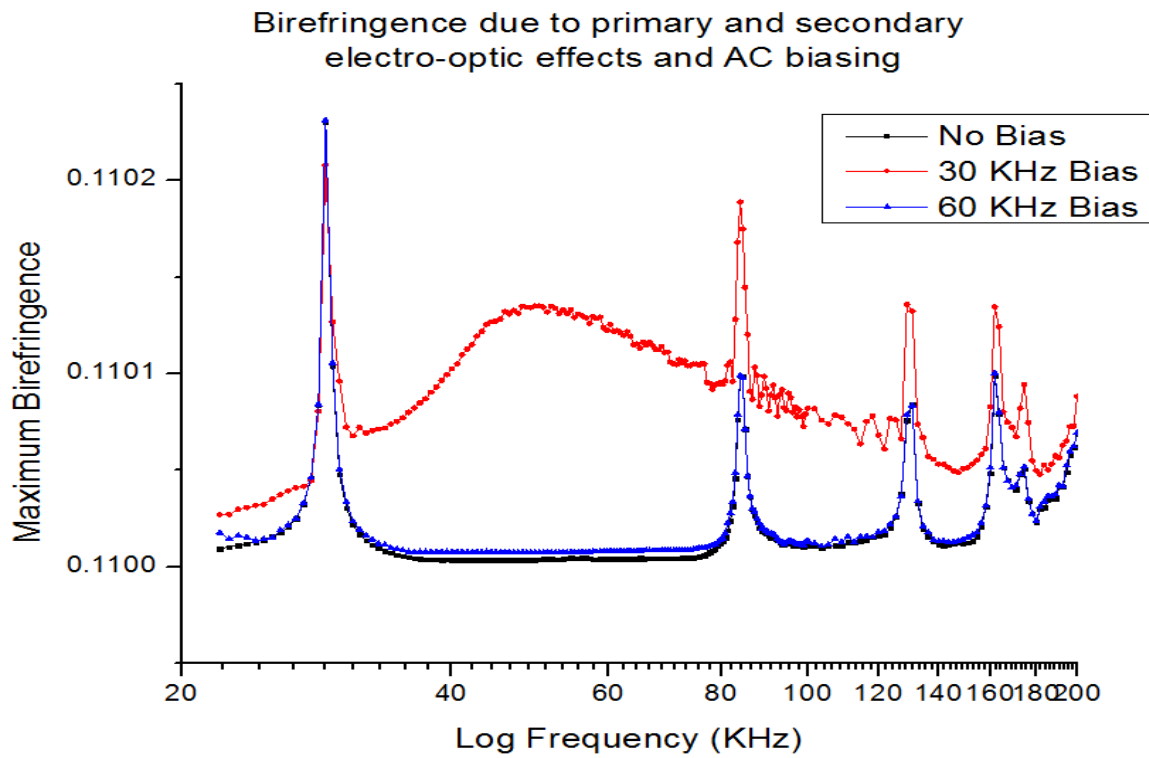


Figure 4.16 Effect of piezo-resonant ac signal biasing on Birefringence of electro-optic modulator

The near the resonant frequency of the sample a beat frequency is often apparent and in the form of an additional amplitude modulation. The frequency of the beat is a function of the modulation voltage and the resonant frequency of the sample.

$$|f_{beat}| = |f_{modulation} - f_{resonance}| \quad (4.17)$$

Because of f_{beat} there is no steady-state response but there is a constant envelope steady-state response (CESS). This CESS refers to the fact that the amplitude of the envelope is sinusoidal and predictable and it is only necessary to simulate to the point where the envelope is maximum in order to find the full response. Furthermore because as the modulation gets close to the resonance frequency the beat frequency becomes smaller thus more cycles are required to reach the CESS. When modulating at the exact frequency the real CESS would actually take an infinite amount of time to determine but can still be accurately estimated.

$$\lim_{f_{mod} \rightarrow f_{res}} CESS = \infty \quad (4.18)$$

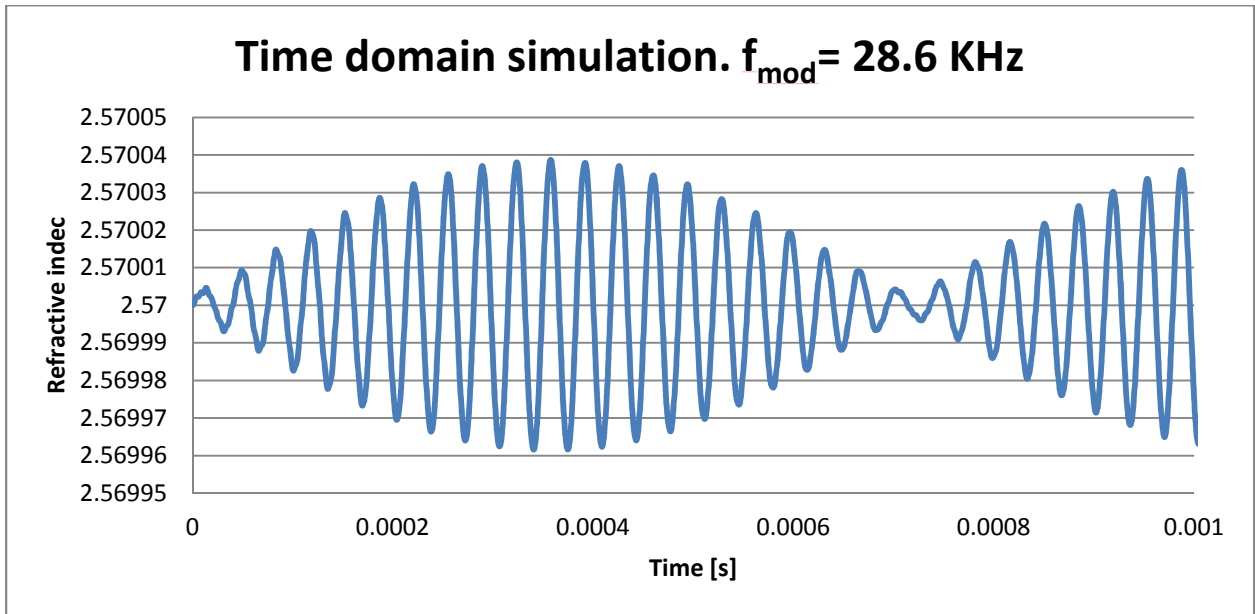


Figure 4.17 FEA time domain simulation of electro-optic modulator showing additional modulation near resonance

This extra amplitude modulation on top of the phase modulated signal is a well-known disadvantage of using modulation near the natural piezoelectric resonance. This effect however

could possibly be compensated for through either real time processing or an alternative optical configuration. Assuming a posteriori knowledge of the device resonant modes it real time FPGA processing of the signal could be done to correct the modulation amplitude. Clearly the unwanted modulation corresponds to the resonant frequency as demonstrated above thus a foreknowledge of the resonant modes could be used to amplitude correct using high speed electronics. Alternatively this correction could also be using two identical crystals as shown in Figure 4.18. A common light source is incident upon both crystals and the driving modulation signal is directly connect6ed to one crystal while the other is delayed by $\pi/2$ before reaching the seconds crystal. When the modulated signals are again combined into a common light signal the resultant signal will be the addition of the signals giving a corrected output.

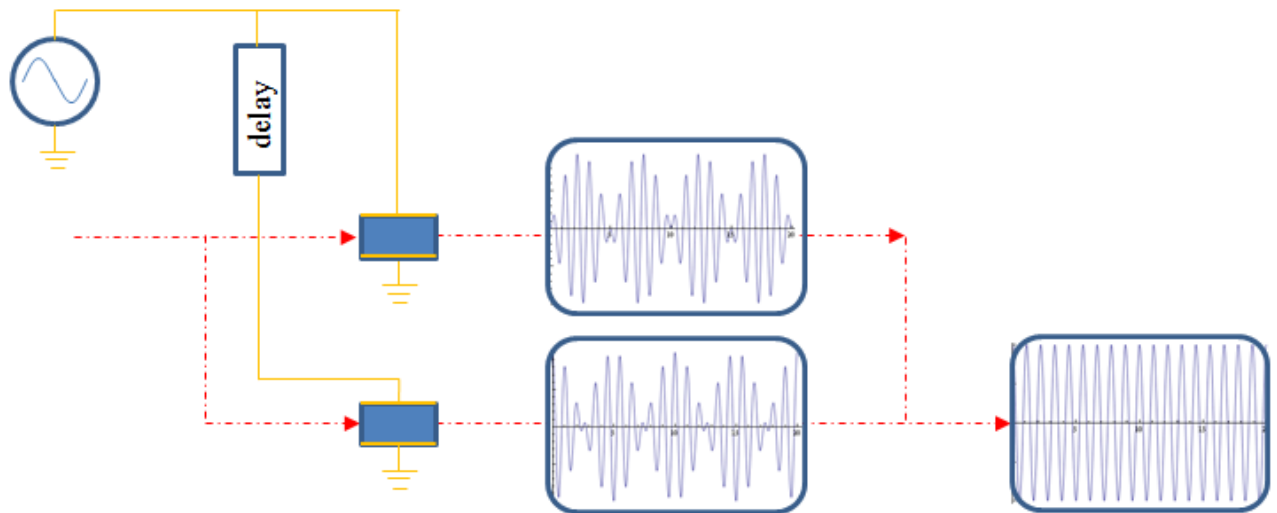


Figure 4.18 Proposed method of correction for unintended amplitude modulation near sample resonance

4.6 Comparison of Bulk EOM's

There are many types of electro-optic modulators configured for modulation of amplitude, phase, frequency, etc. and each can also be configured as a non-resonant or resonant modulator. Resonant modulators typically use an inductor in series with the mostly capacitive parallel plate configuration of the EO device. The addition of this component allows for a higher voltage than that applied by the frequency source at one specific resonant frequency, effectively lowering the half wave voltage of the device. Typically these devices (both resonant and non-resonant) are operated far from the natural mechanical resonance so as to avoid

A distinction must be made here between the electrically resonant modulators and the mechanically resonant modulator discussed in this thesis. Electrically resonant modulators use additional electrical components to form an electrical tank circuit resulting in a low half wave voltage at one frequency over a very small bandwidth of operation (high Q). Mechanically resonant modulators use high strains resultant from the natural acoustic vibration mode of the material to give higher phase changes effectively lowering the half wave voltage. The drawback of these devices is an often unwanted amplitude modulation (in addition to the desired phase modulation). The addition of AC biasing allows for broadening the effective usually bandwidth of these devices.

Table 4.5 Qualitative comparison of half-wave voltage and bandwidth of common electro-optic modulator types

Type	V_{π}	Bandwidth	comments
Non-resonant	high	high	
Electrically resonant	low	low	
Mechanically resonant (no AC bias)	low	low	Unwanted amplitude modulation
Mechanically resonant (with AC bias)	low	high	

The series resonant circuit depicted in Figure 4.19 consists of a voltage driver (V1), a resistor R1 which represent the transmission line, a resistor R2 which is a terminator designed to minimize reflections, an inductor L1 and a capacitor C1 which models the actual EOM parallel plate configuration.

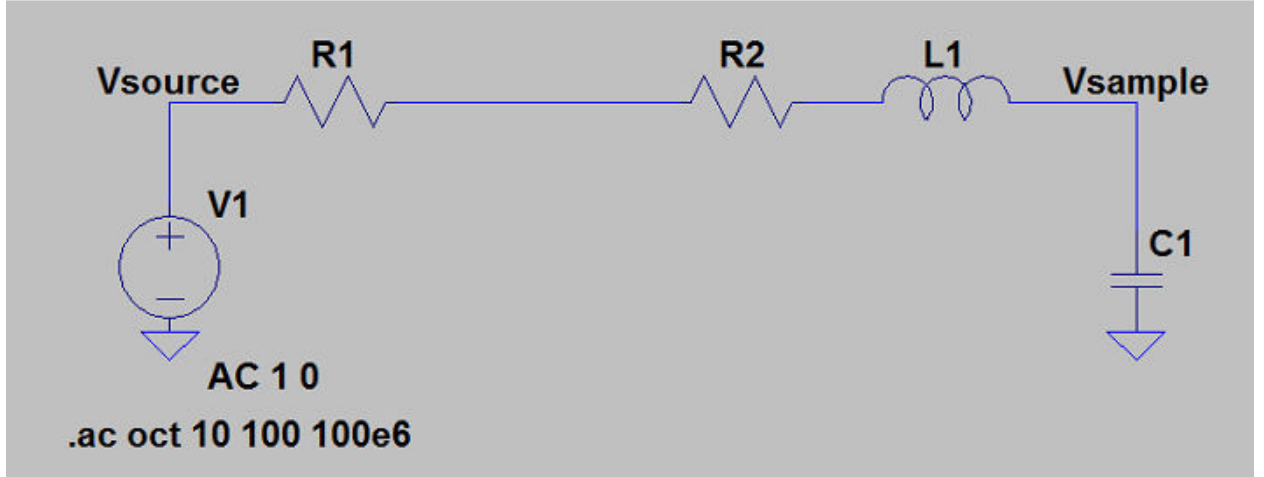


Figure 4.19 Series resonant electro-optic modulator circuit

The capacitance of the device is $C1=(\epsilon_0*\epsilon_r*A_s)/d$ and the inductance of L1 is chosen to give equal but opposite reactance at a specific resonant frequency.

$$f_r = \frac{1}{2\pi\sqrt{L1 C1}} \quad (4.19)$$

$$Z_l = j 2\pi f L \quad (4.20)$$

$$Z_c = \frac{1}{j 2\pi f C} \quad (4.21)$$

$$V_{Sample} = abs \left(\frac{V_{source}}{R1 + R2 + (j 2\pi f L) + \left(\frac{1}{j 2\pi f C} \right)} \left(\frac{1}{j 2\pi f C} \right) \right) \quad (4.22)$$

Assuming an EOM of thickness $d=10[\text{mm}]$ and length= $25[\text{mm}]$ the area $A_s=2.25 \times 10^{-4} \text{ m}^2$ and $\epsilon_r=29.16$ gives $C1=6.45\text{pF}$. For a resonate frequency at 250 KHz, $L1=62.83 \text{ mH}$. Using these parameters a 1 volt source voltage can easily give 841 volts at the sample. The figure below shows the response of the circuit in Decibels; clearly there is a very large signal at resonance over a very narrow band.

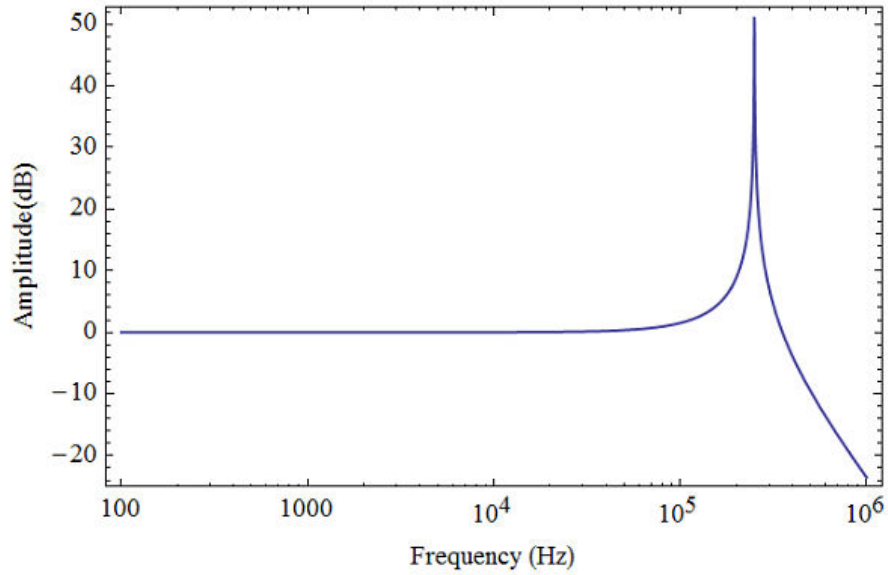


Figure 4.20 Voltage at Sample (in dB) resultant from series resonant circuit

4.6.1 Finite Element Model Comparing Modulator Types

To compare these modulator types a finite element model was made for each. Starting with the formulas for calculating the Pockels effect for 3m symmetry materials as derived in Chapter 3.

As derived in chapter 1 for 3m Symmetry and assuming $E_1 = E_2 = 0$

$$\begin{aligned} n'_x &\approx n_o - \frac{1}{2} n_o^3 r_{13}^x E_z \\ n'_y &\approx n_o - \frac{1}{2} n_o^3 r_{13}^x E_z \\ n'_z &\approx n_e - \frac{1}{2} n_e^3 r_{33}^x E_z \end{aligned} \quad (4.23)$$

The Birefringence is

$$\Delta n \approx n'_z - n'_x \approx n_e - \frac{1}{2}n_e^3 r_{33}^x E_z - n_o + \frac{1}{2}n_o^3 r_{13}^x E_z \quad (4.24)$$

The phase for a transverse modulator of thickness t and Optical propagation length L :

$$\varphi = \frac{2\pi L}{\lambda} (n'_z - n'_x) \quad (4.25)$$

$$\varphi = \frac{2\pi L}{\lambda} (n_e - \frac{1}{2}n_e^3 r_{33}^x E_z - n_o + \frac{1}{2}n_o^3 r_{13}^x E_z) \quad (4.26)$$

$$\varphi = \underbrace{\frac{2\pi L}{\lambda} (n_e - n_o)}_{\text{From natural Birefringence}} - \underbrace{\frac{2\pi L E_z}{\lambda} \left(\frac{n_o^3 r_{13}^x - n_e^3 r_{33}^x}{2} \right)}_{\text{From induced Birefringence}} \quad (4.27)$$

The half wave voltage is the point when induced phase change = π

$$\pi = \frac{2\pi L E_z}{\lambda} \left(\frac{n_o^3 r_{13}^x - n_e^3 r_{33}^x}{2} \right) \quad (4.28)$$

$$E_z = \frac{\lambda}{n_o^3 r_{13}^x - n_e^3 r_{33}^x} \frac{1}{L} \quad (4.29)$$

$$E_z = \frac{V}{t} \quad (4.30)$$

$$V_\pi = \frac{\lambda}{n_o^3 r_{13}^x - n_e^3 r_{33}^x} \frac{t}{L} \quad (4.31)$$

To induce photoelastic effects the constant strain coefficient r_{ij}^x can be replaced by the constant stress coefficient r_{ij}^X which include the constant strain coefficient, elasto-optic and piezoelectric coefficients.

$$r_{13}^X = r_{13}^x + d_{31}p_{11} + d_{31}p_{12} + d_{33}p_{13} \quad (4.32)$$

$$r_{33}^X = r_{33}^x + 2d_{31}p_{31} + d_{33}p_{33} \quad (4.33)$$

$$V_{\pi} = \frac{\lambda}{n_o^3 r_{13}^X - n_e^3 r_{33}^X} \frac{t}{L} \quad (4.34)$$

Alternatively when forming the equations for the FEA model slightly less simplified method can be used. For 3m Symmetry and assuming $E_1 = E_2 = 0$

$$\begin{aligned} n'_{11} &= 1 / \sqrt{\frac{1}{n_{11}^2} + r_{13} E_3 + p_{11} x_{11} + p_{12} x_{22} + p_{13} x_{33} + p_{14} x_{23}} \\ n'_{22} &= 1 / \sqrt{\frac{1}{n_{22}^2} + r_{13} E_3 + p_{12} x_{11} + p_{11} x_{22} + p_{13} x_{33} - p_{14} x_{23}} \\ n'_{33} &= 1 / \sqrt{\frac{1}{n_{33}^2} + r_{33} E_3 + p_{31} x_{11} + p_{31} x_{22} + p_{33} x_{33}} \\ n'_{23} &= 1 / \sqrt{p_{41} x_{11} - p_{41} x_{22} + p_{44} x_{23}} \\ n'_{31} &= 1 / \sqrt{p_{44} x_{31} + p_{41} x_{12}} \\ n'_{12} &= 1 / \sqrt{p_{14} x_{31} + p_{66} x_{12}} \end{aligned} \quad (4.35)$$

The total phase shift

$$\varphi = \frac{2\pi L}{\lambda} (n'_z [\lambda] - n'_x [\lambda]) \quad (4.36)$$

The induced phase shift can be found by subtracting out the natural Birefringence

$$\Delta\varphi = \frac{2\pi L}{\lambda} ((n'_z [\lambda] - n'_x [\lambda]) - (n_e [\lambda] - n_o [\lambda])) \quad (4.37)$$

$$\text{At } V_{\pi} \quad \Delta\varphi = \pi \quad (4.38)$$

$$V_{\pi} = \frac{\pi V_{\text{applied}}}{\Delta\varphi} \quad (4.39)$$

The perturbed refractive index n' can be found in the model by taking the average refractive index through the center of the sample in the Y direction. The refractive index with no electric field applied ($n[\lambda]$) is a function of the wavelength, the data used is from the handbook of

Optical materials [9]. This particular geometry has a piezoelectric resonance at about 72 KHz but no resonant effects at 60 KHz so a non-resonant modulator and mechanically resonant modulator can be easily compared simply by modulating on and off resonance. The linear electro-optic coefficient can be assumed to be constant because it changes little with wavelength [9].

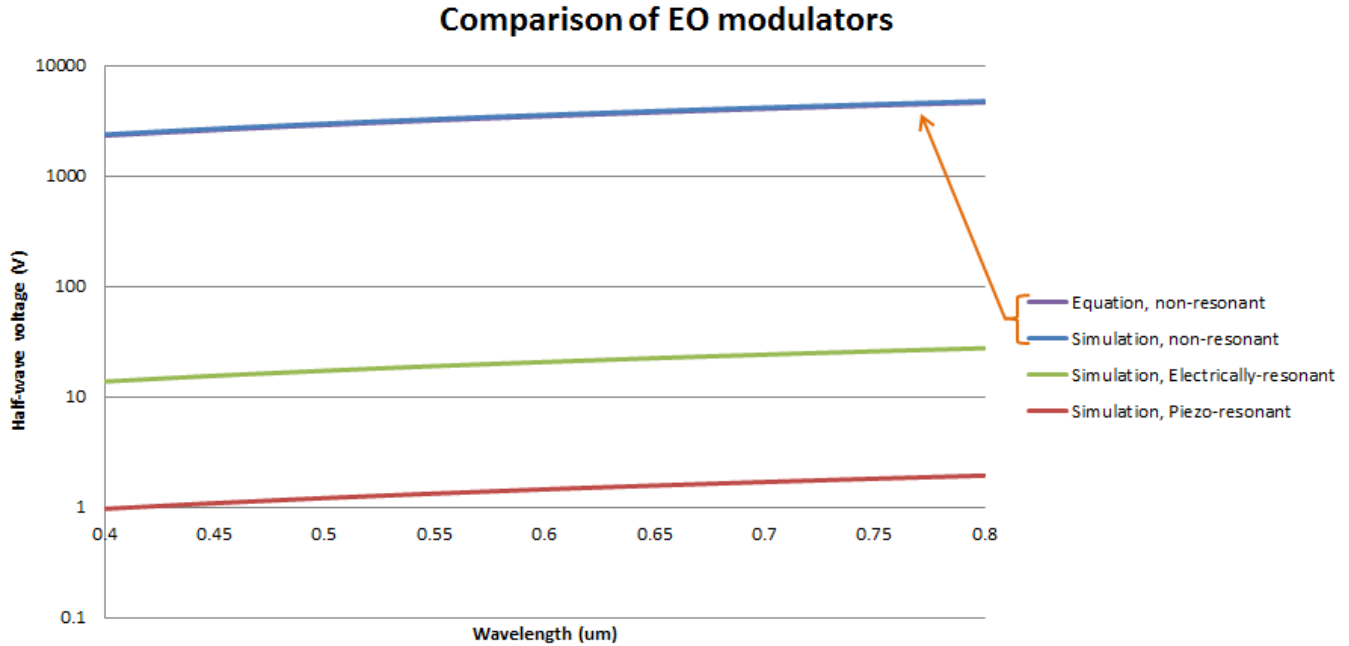


Figure 4.21 Comparison of the half-wave voltage of non-resonant, electrically-resonant, and piezo-resonant electro-optic phase modulators

These results show that the COMSOL simulation matches equation very well confirming the validity of the model. The model accurately calculates phase modulator half wave voltage. The two resonant EOMs give significantly improved V_{π} . In this case Piezo-resonant performs better than the electrically resonant modulator, however it is possible to observe the opposite and the results are largely dependent on the chosen piezoelectric resonant mode used and the piezoelectric coefficient. These results demonstrate improvement in half wave voltage for Piezo-resonant modulators and significant advantage over electrically resonant modulators. It is also possible to combine mechanically and electrically resonant to get very low half wave voltage,

this would over limit the wide bandwidth potential of the device. It may be that this sensitivity will one day allow for modulation directly from wireless signals without the need for active electrical components.

4.7 Summary

Several Finite Element models were constructed to study electro-optic enhancement, to more fully understand experimental observations and to examine methods that would be difficult to realize experimentally. The model of the combined interaction of a piezoelectric sample with optical plane wave propagation has been shown to give results consistent with experimental observations of piezoelectric induced enhancement. The model in section 4.5 used to compare electro-optic modulator types produces a response that matches the electro-optic equations. Additionally this model clearly demonstrates the usefulness of piezo-resonant enhancement in terms of low half wave voltage. The time domain model of dual signal ac biased configuration was able to show wide bandwidth enhancement when biased at the resonant frequency and matches well with experimental observations from [6]. Microwave transmission in periodically poled structures was modeled in section 4.2. Poling can have a significant effect on transmission particularly when the poling direction is transverse to the wave propagation. The transmission spectrum can be tuned by adjusting the number of polled elements in a structure.

CHAPTER 5: MECHANICAL VIBRATION MEASUREMENTS

5.1 Laser Vibrometry

Laser vibrometers are used to make single point physical displacement measurements and can sense these movements at high frequencies. They can also sense velocity and acceleration. The two main principles involved are the Doppler Effect and interferometry. The Doppler Effect is the observed shift in frequency of a reflected wave due to the velocity of the sensed object.

Vibrometers measure velocity of the object by determining the frequency shift with interferometry. The PolyTec UHF-120 vibrometer used for the research in this dissertation uses a heterodyne interferometer (See Figure 5.1).

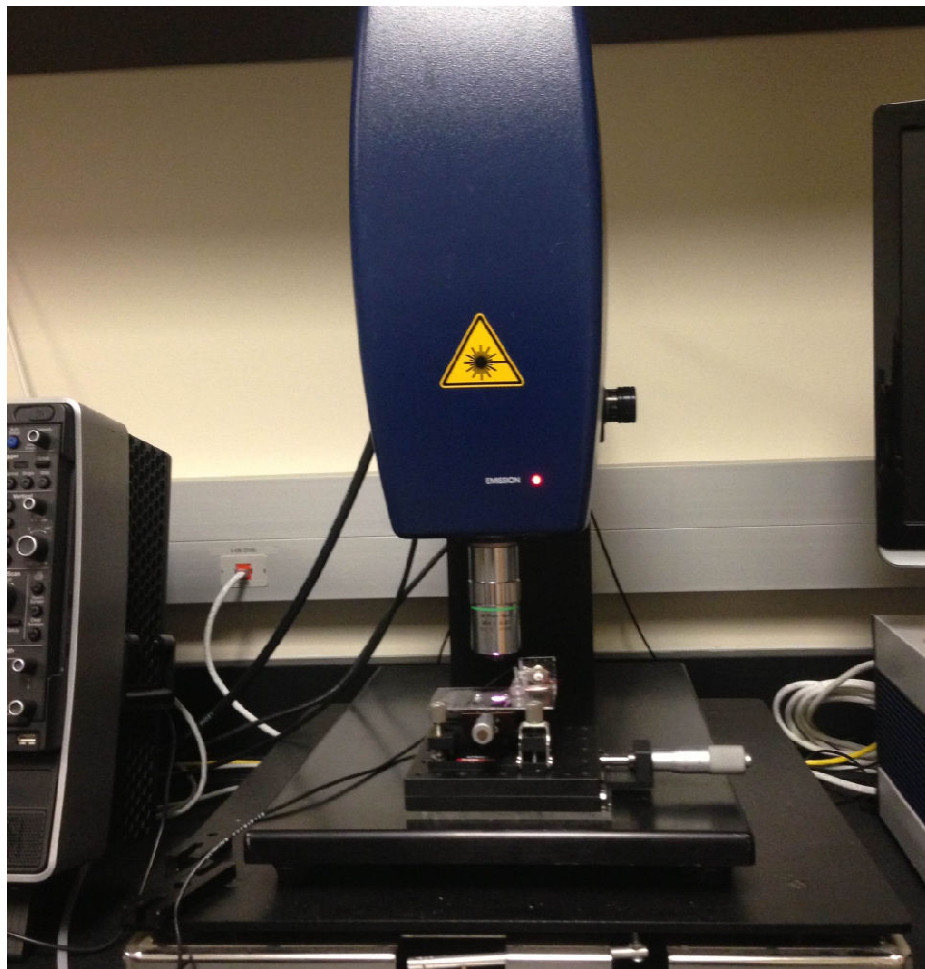


Figure 5.1 Photo of PolyTec UHF-120 Vibrometer and measurement fixture

Heterodyne interferometry uses two laser frequencies as opposed to Homodyne which uses one. As illustrated in Figure 5.2 both laser signals start from the same location; they are both linearly polarized with polarization orthogonal to each other [21]. Both signals reach a polarizing beam splitter which directs the F_2 signal over to a set of mirrors that steer the beam back left to the splitter to the direction of the source. The F_1 signal passes straight through the beam splitter and is incident on the sample being tested. After experiencing a Doppler shift from the sample vibration the signal is frequency becomes $F_1 \pm \delta F$ and is reflected back towards the direction of the source. The detector and control electronics are used to measure the beat frequency that results from the F_2 reference signal and Doppler adjusted $F_1 \pm \delta F$ to find the velocity and the direction of displacement.

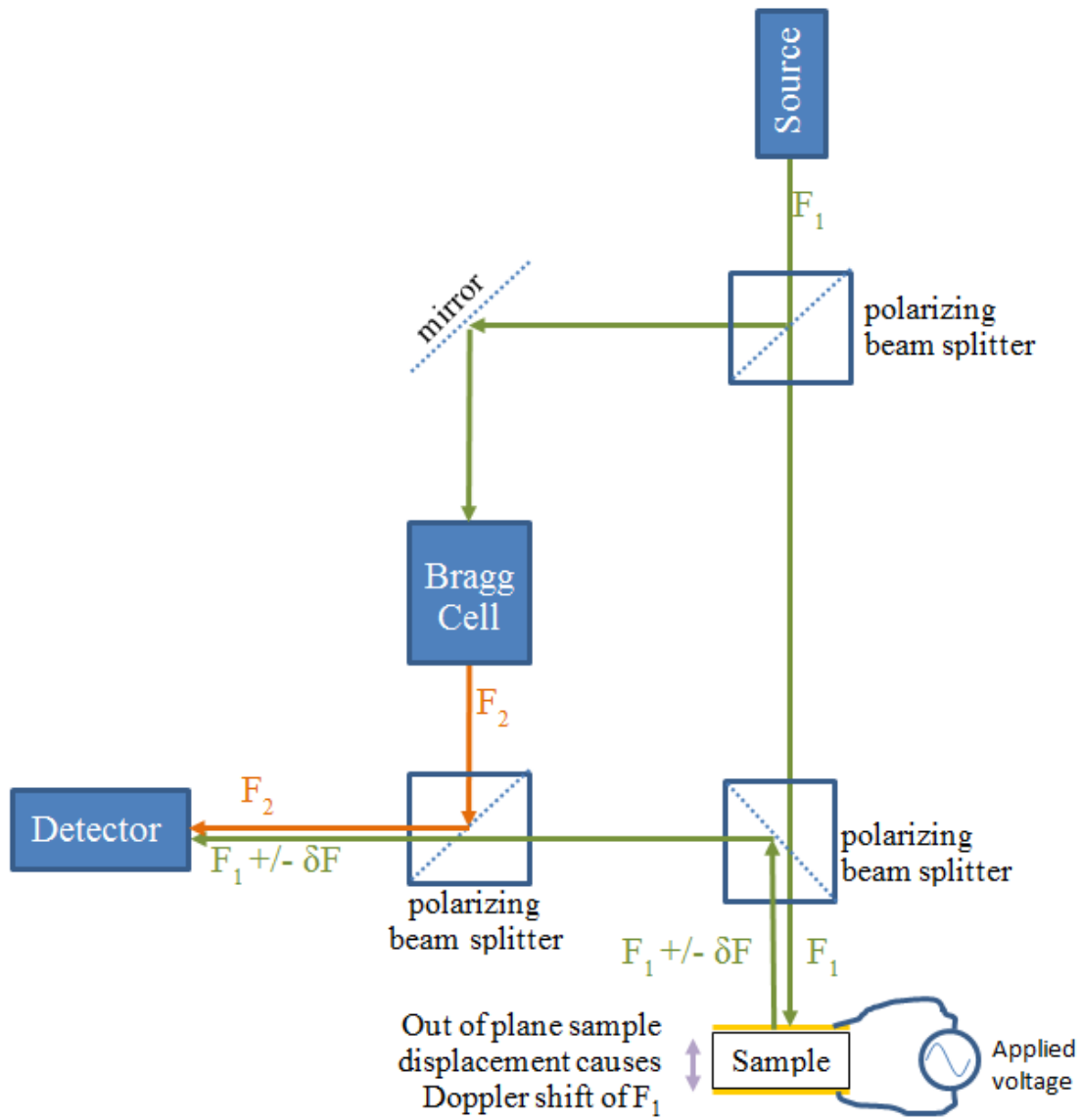


Figure 5.2 Heterodyne Interferometry configuration

The measured frequency shift f_D is twice the velocity v divided by the wavelength of the emitted wave λ .

$$f_D = \frac{2v}{\lambda} \quad (5.1)$$

The phase shift of the interfering waves $\Delta\phi$ is determined by the path length difference between the waves and is proportional to the number of interference fringes N . This is how the displacement is determined.

$$\Delta\phi = \frac{4\pi d}{\lambda} = 2\pi N \quad (5.2)$$

The total intensity at the photodetector is determined by the intensity of the two individual beams I_1 and I_2 the wavelength and the path difference between the beams $r_1 - r_2$. The total intensity may vary from zero to four times one single intensity.

$$I_{tot} = I_1 + I_2 + 2\sqrt{I_1 I_2} \cos(2\pi(r_1 - r_2)/\lambda) \quad (5.3)$$

A photodetector is used to pick up the optical signal from the interferometer. The current from the detector is shown in Equation (5.4) and has a DC component i_{DC} and AC component \hat{i} [22]. The AC component is governed by the Bragg frequency f_B , the modulation phase angle φ_m and the zero-phase angle θ_0 . The displacement of the sample $s(t)$ will determine the modulated phase angle as in Equation (5.5). The derivative of both sides of this equation using the relationships in Equations (5.6) and (5.7) and the results is Equation (5.8). This represents the Doppler frequency

$$i_{det}(t) = i_{DC} + \hat{i} \cos(2\pi f_B t + \varphi_m + \theta_0) \quad (5.4)$$

$$\varphi_m(t) = \frac{4\pi s(t)}{\lambda} \quad (5.5)$$

$$\frac{d\varphi}{dt} = 2\pi f \quad (5.6)$$

$$\frac{ds}{dt} = v \quad (5.7)$$

$$\Delta f(t) = \frac{2v(t)}{\lambda} \quad (5.8)$$

The Vibrometer can handle a range of scanned input frequencies. The device records the signal from the source and measurement head in the time domain for a time period determined by the user. This time period must be long enough to capture all of the scan frequencies. The vibrometer software then does a transformation of the signal to the frequency domain. Because of the leakage effects of the transformation used the resulting amplitude of the spectrum may not represent the actual signal. The software uses the Fast Fourier Transform (FFT) for converting to the frequency domain. The FFT uses a discrete spectrum meaning that if a time signal frequency does not match the FFT line it will be distributed over several lines. There are various windowing techniques used to reduce these affects. A window function is multiplied by the time domain signal; most window functions start and stop at zero in order to reduce jumps in the signal near the time window edge [23]. For this reason the ratio of the source and vibrometer signals are used in this dissertation. Thus for example instead of displacement in meters, the ratio meters/volt is used.

The enhancement of the electro-optic signal is in part results of the high strains inside the sample during resonance. These strains, physical displacement, velocity and acceleration can all be examined and understood more fully by use of laser vibrometry. A high frequency vibrometer, the Polytec UHF-Vibrometer was used to test the mechanical deformation of several electro-optic materials under sinusoidal agitation. This vibrometer offers only single point measurements but can scan the response of the crystal over a range of frequencies. In order to give a full view of the sample surface the measurement was repeated over each sample in a grid patterned layout.

5.2 Measurement Setup

The vibrometer measurement setup is shown in Figure 5.3 below. The vibrometer signal is digitized by an oscilloscope that is controlled by a computer. The sample is excited by an arbitrary function generator, the output of the source is split by an RF splitter, one end goes to the sample and the other to one channel of the scope. This allows the software to measure the actual signal applied to the sample and the resulting vibration signal from the sample vibration. The Sync output of the source which is a TTL level signal corresponding to the frequency at the Source output is feed into the scope so that the excitation frequency can be measured. The Polytec VibroSoft software is used to analyze the source and vibrometer signals. A custom Visual Basic for Applications (VBA) program was written to control the entire vibrometer system. The program accepts the user input for the grid to be measured and the automatically prompts the user for where to move the positioning stage and then controls the vibrometer software and then saves the displacement data to a common file. Additionally a link is made to MatLab for simultaneous plotting of the sample surface. Alternatively a program was also written to sweep through a range of frequencies and collect time domain data at a single measuring point. The program does this by setting the Source frequency through GPIB control.

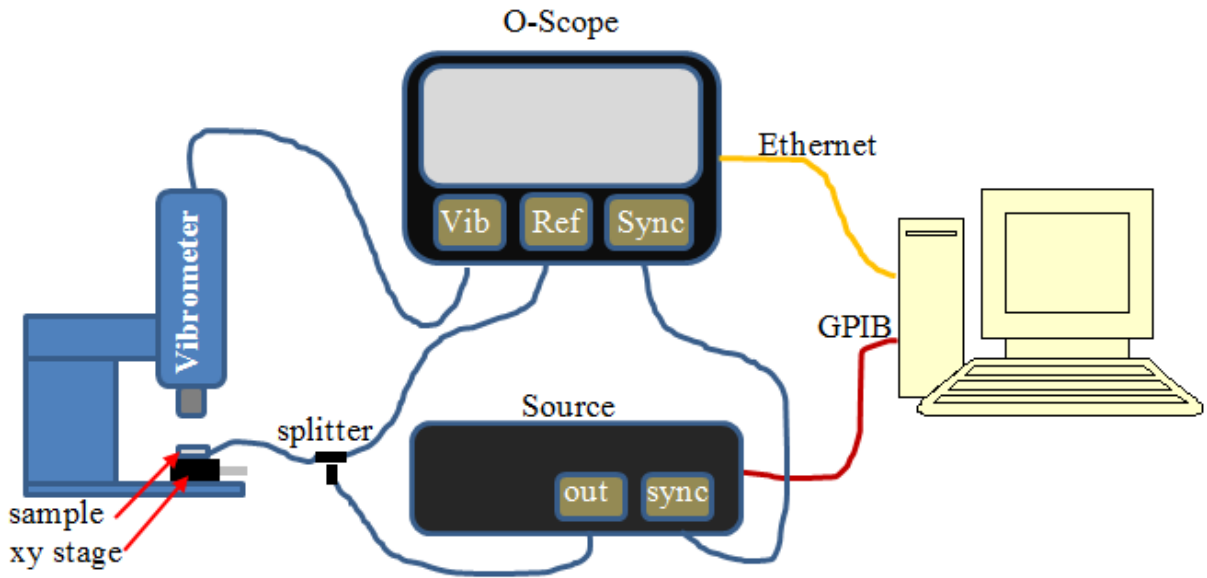


Figure 5.3 Vibrometer measurement configuration

5.3 Samples and Configuration

To build up a representation of the sample surface a 2D raster scan of the surface is made. The figure below shows a representation of the Quartz and PMN-PT samples that were measured. The samples were both constrained on the same surfaces where they are electroded, using a special fixture to hold them from one end to allow for overall vibration of the sample. The quartz sample was measured over a total of 116 points and the PMN-PT sample which is smaller was measured over 30 points. The vibrometer is able to measure and analyze surface vibration in a variety of ways. Typically the source generator makes a scan over a range of frequencies and the resulting signal from the device is converted to the frequency domain with a Fast Fourier Transform (FFT). When a cyclic signal source is used the sample deformation naturally changes from expansion to contraction at some constant offset phase from the source. Given this response the FFT takes the maximum absolute value of this displacement thus on any surface plot of the

displacement is not a true plot of the displacement at a given point in time but of the maximum displacement at over the whole time cycle. This is illustrated Figure 5.5 in A where is it shown that the sample surface is not constant but changes with time; part B shows that the vibrometer displacement data would record this vibration as the envelope of the shift.

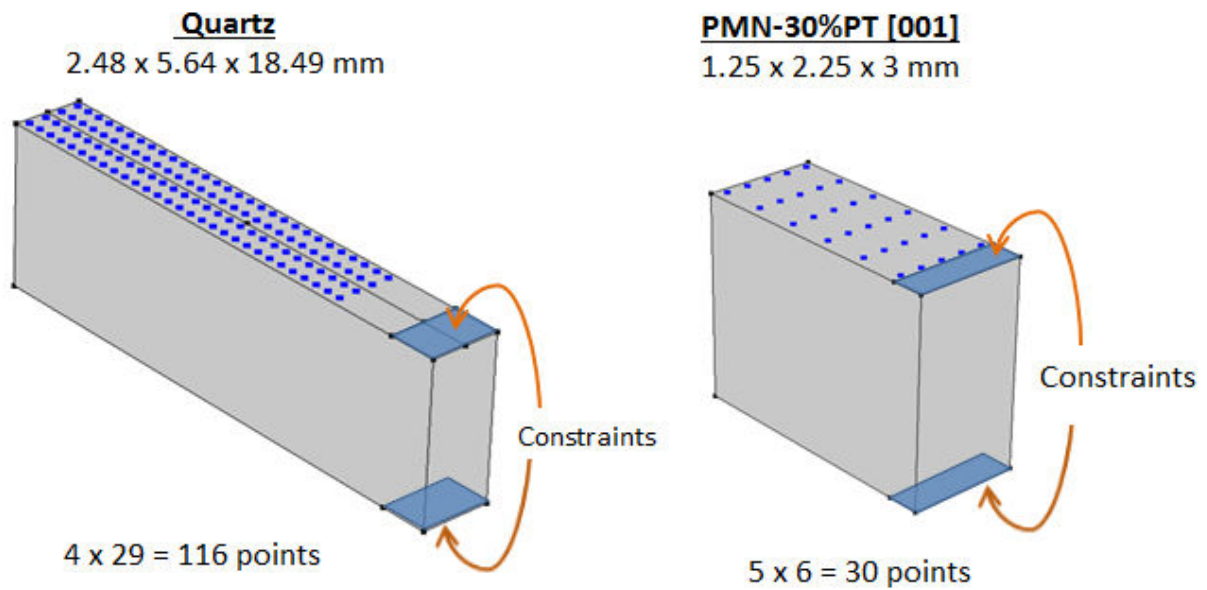


Figure 5.4 Multipoint measurement for two dimensional representation of sample surface using vibrometer test data

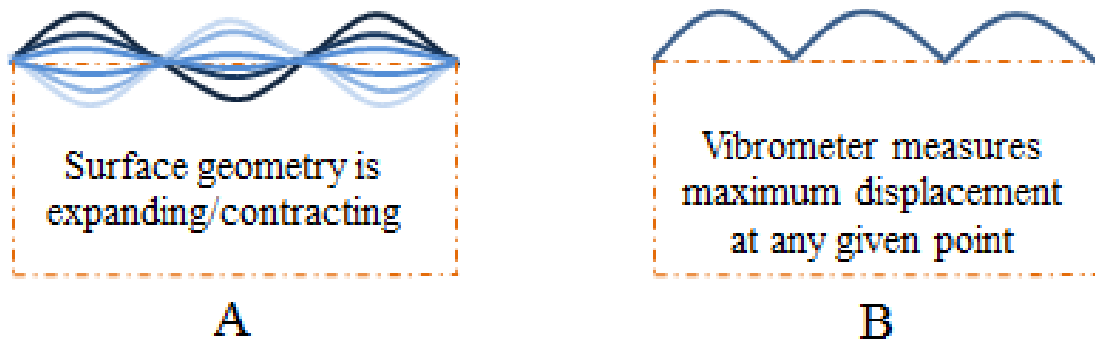


Figure 5.5 Surface displacement measurement by vibrometer gives amplitude of displacement while actual sample is periodically changing as per the applied sinusoidal field

5.4 Surface Plot Results

The surface displacement of Quart and PMN-30%PT were measured over a range of frequencies. The displacement of these samples was also simulated under identical conditions using Finite Element Modeling. In the plots below the yellow section indicates the measured area with displacement at zero. The black section is the clamped portion of the sample and the brown is both unmeasured and unclamped. The Figure below indicates the Quartz surface displacement at the strongest resonance indicating good agreement between simulation and experiment.

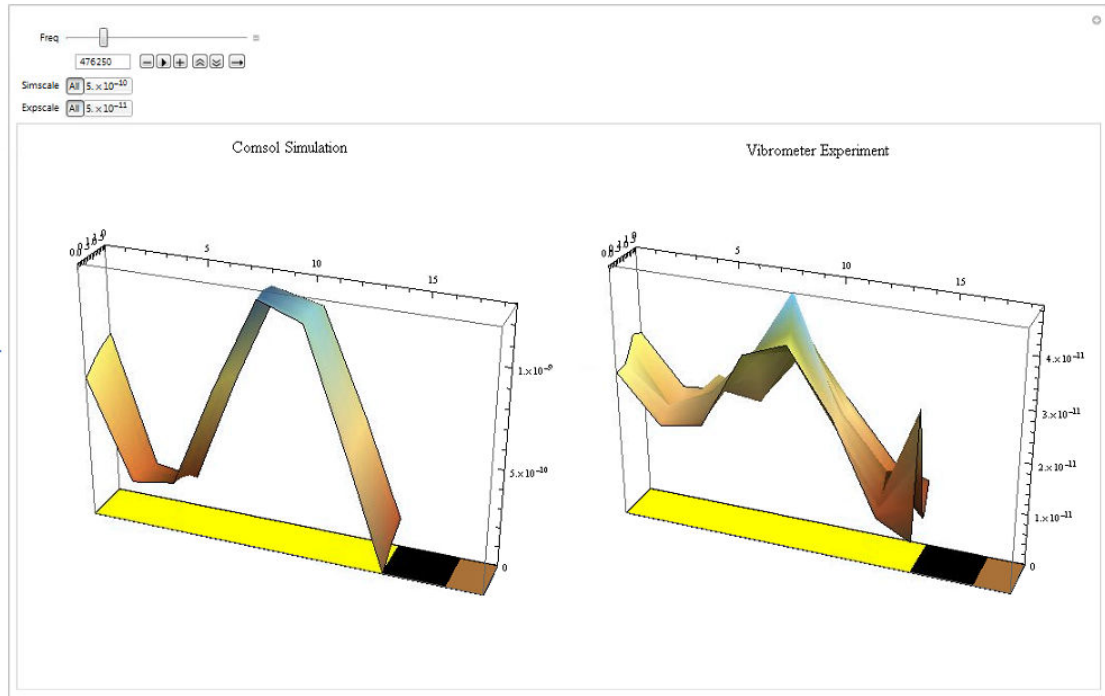


Figure 5.6 Quartz (sample #2) comparison of COMSOL Simulation and vibrometer surface displacement

The PMN-30%PT sample was measured both in the time domain and frequency domain. The frequency domain results are shown in the next section. The time domain results are shown here at 329 KHz and the displacement is given at one specific time. The displacement has two main factors, a purely up and down z direction motion and partly a twisting. The measurement results match well with the COMSOL eigenfrequency solver at 368 KHz that demonstrates the good agreement for the resonate mode.

PMN-30%PT Simulation vs. Experiment

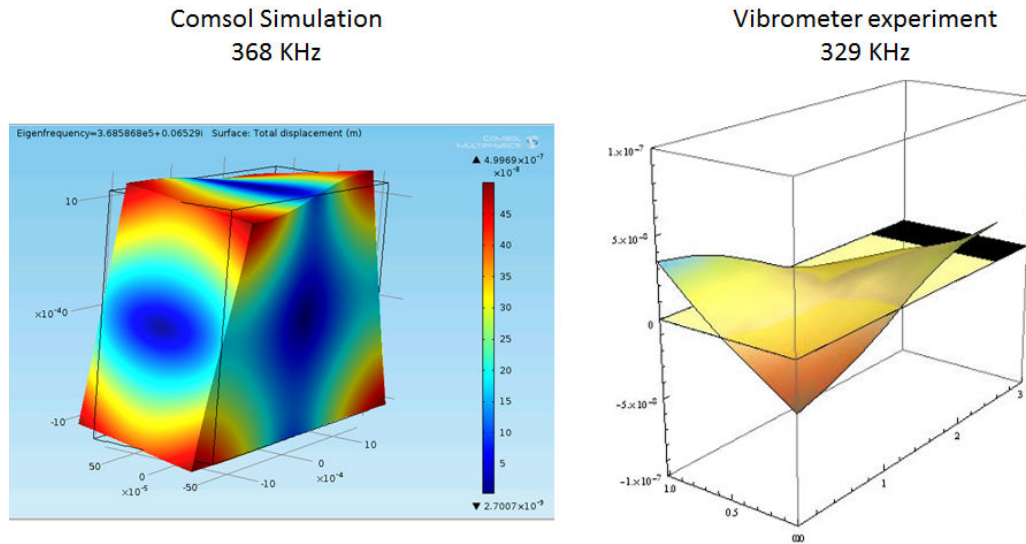


Figure 5.7 PMN-30%PT (sample #1) COMSOL simulation and vibrometer surface displacement

In Figure 5.8 the PMN-PT sample plots are shown at the major resonant frequencies, all plots are on the same scale. Also included in the figure for comparison are the admittance and electro-optic measurement results. It is clear from the results that the largest sample displacement does not always match the largest electro-optic response. The excitation frequency of 328750 Hz has a EO response of about 10.4 μV_{rms} while the relatively small displacement at 891875 Hz gives the largest EO response.

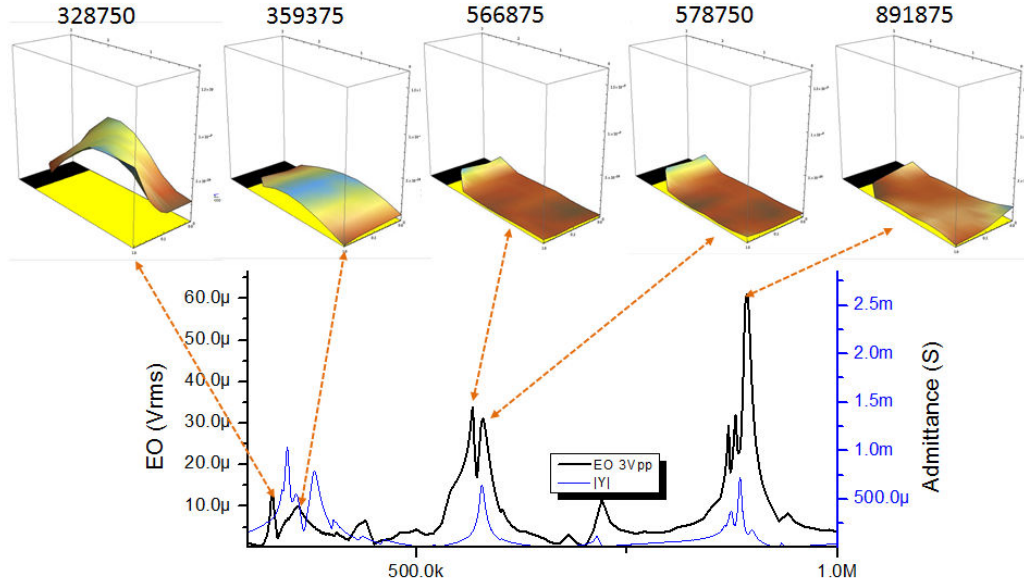


Figure 5.8 PMN-30%PT displacement plots at major resonant frequencies

5.5 High Frequency Displacement

Typically photoelastic effects are only apparent up to the low MHz region however because it is believed that piezoresonant displacement currents can couple with transverse optical phonons (which can exist up to GHz) it may be the enhancement can be much higher than previously measured. Thus vibrometer experiments have been performed in to the high MHz region to find the typical surface vibrations of crystals in this range and how this response may effect enhancement.

$$\text{PMN-30\%PT } d_{33}=1981 \text{ [C/N]}, d_{31}=d_{32}=-921 \text{ [C/N]} \quad (5.4)$$

$$[\text{C/N}] = [\text{m/V}] \quad (5.3)$$

The PMN-30%PT sample was tested both for its electro-optic response and for its vibration. The vibration was tested along its major X, Y, Z axis directions. Figure 5.9 shows the testing configurations; silver paste electrodes were used on the XY surfaces allowing for electric

field in the Z direction (also the poling direction). The sample was rotated in three different directions to measure the d_{31} , d_{32} and d_{33} piezoelectric coupling. The vibrometer is suited to high frequency vibration measurements while piezoelectric coefficients are typically measured at very low frequencies. Piezoelectric coefficients are reported in terms of Coulombs per Newton (C/N) or meters per Volt (m/V) which are equivalent units. PMN-30%PT has an identical d_{31} and d_{32} coefficient of -0.921 [nm/V] and a d_{33} of 1.981 [nm/V] [19]. The coefficients cannot be expected to be exactly the same when measured at high frequencies but it is clear from the results of Figure 5.10 that the measurement is very consistent with reported values. Note that this particular vibrometer test only considers the magnitude of the response, not the phase, thus it is the absolute value to the piezoelectric coefficient that is measured.

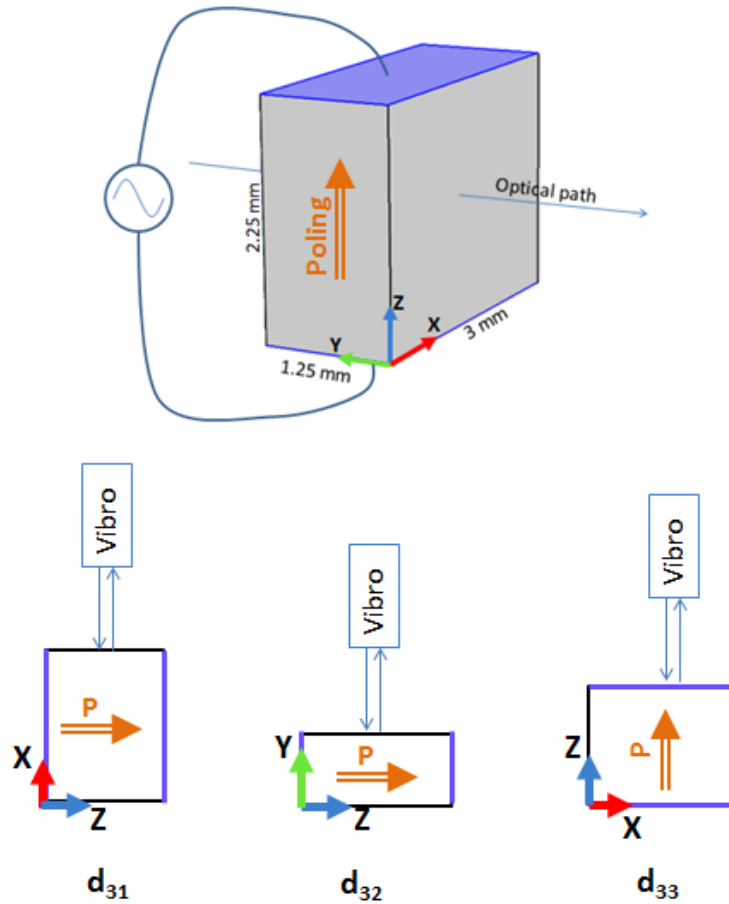


Figure 5.9 Configuration for PMN-30%PT sample for electro-optic and vibrometer tests

The results of this test are shown in Figure 5.9 and there is clearly a large increase in the electro-optic signal near the resonant frequencies as indicated by the vibrometer results. This correlation is particularly true for the fundamental modes below 1MHz and is expected due to the high strain coupled to the refractive index through the photoelastic effect. Above 1MHz the crystal becomes more clamped meaning there is less displacement however at the same time there is still a rather high spike in the electro-optic response. This coupling seems to be due to more than just the photoelastic and electro-optic response and is perhaps a result of the induced polarization in the material. This induced polarization has less of frequency limitation as compared to

photoelasticity but can still result in the sample type of resonant induced improvement of the signal.

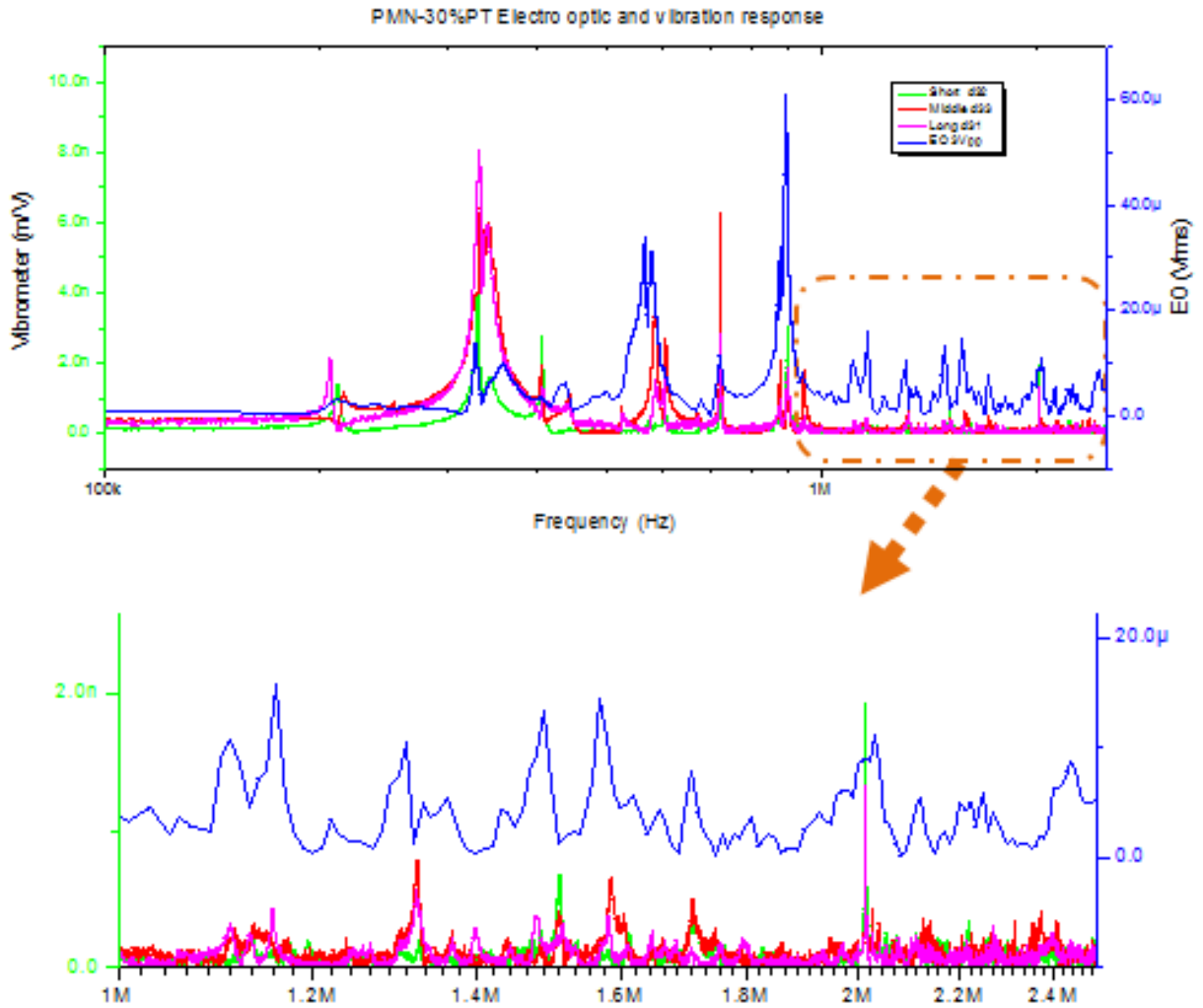


Figure 5.10 PMN-30%PT electro-optic and vibrometer tests indicating that electro-optic enhancement persists in to the MHz region where sample strain is minimal

In addition to the single point measurements a full view of the surface displacement for PMN-30%PT is presented in Figure 5.11. In the figure the red block represent the sample at rest with no displacement, the blue dots are the actual measurement points on the sample and the other

area is the interpolation grid between the test points. Three scan tests were done to test out-of-plane displacement in the x, y, and z directions and each was combined into one figure for primary resonance at 324375 Hz. The actual displacement was multiplied by 10^8 to give an agitated view of the sinusoidally agitated geometry. The results show that the largest change in sample dimension is in the z direction (same as the applied field).

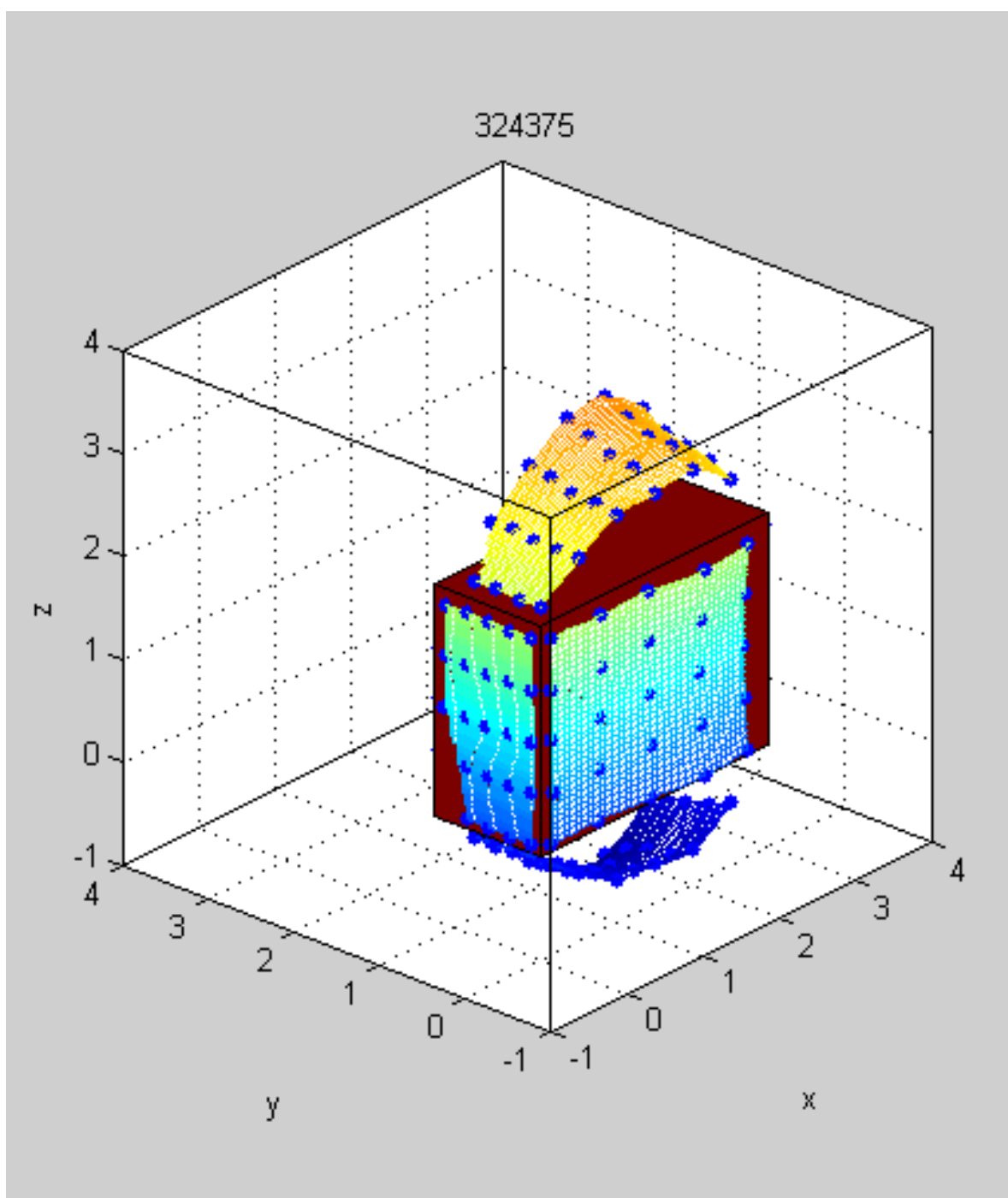


Figure 5.11 Full view of PMN-30%PT sample surface displacement

5.6 Velocity and Acceleration

The enhanced optical signal is due to more than just the static strain in the sample but rather the dynamic nature of the sample under resonance. Because of this relationship it may be interesting to determine the association of the surface velocity and acceleration under applied field and association with the optical signal enhancement. A single point measurement was performed on the PMN-30%PT sample and the displacement, velocity and acceleration were recorded (See Figure 5.12). The electric field was applied in the z direction and the measured parameter was in the same direction. The actual measurement point was near the center of the sample on the surface. The all three measurements display peak near the resonant frequencies particularly near 330, 570 and 880 KHz; all three measurements also have lower amplitude at each of these successive frequencies. The acceleration results however do stand out, in that they not decrease nearly as much as the displacement results do.

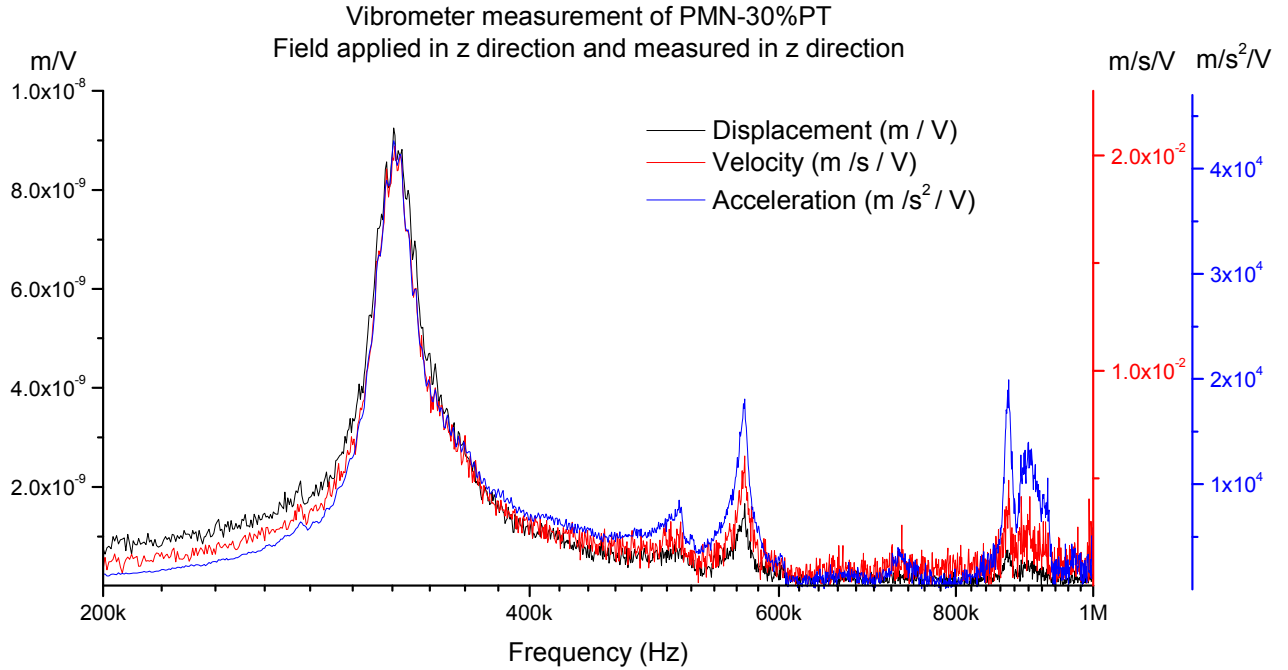


Figure 5.12 Vibrometer measurement of displacement, velocity, and acceleration of a PMN-30%PT sample

5.7 Summary

The physical dimension change of the piezoelectric samples was studied with an ultra-frequency vibrometer. Point-by-point out-of-plane data was reconstructed and interpolated to give a representation of the sample surface under sinusoidal agitation. The ratio of applied signal divided by the displacement in the measured direction was recorded effectively determining the high frequency piezoelectric coefficient. The piezoelectric coefficient measured is in general smaller than that reported in literature because the crystal cannot respond fast enough to the field however at resonance the coupling is much higher and comparable to the low frequency values. The velocity and acceleration of the sample surface was also examined and it was observed that the acceleration of the surface does not decrease as much as the displacement when compared at

major resonate frequencies. These results suggest that the acceleration have a role in high frequency enhancement given the both the acceleration and electro-optic signal may show significant peaks when evaluated at higher frequencies.

CHAPTER 6: ACOUSTO-OPTIC FIGURE OF MERIT OPTIMIZATION

Section 6 McIntosh, R., A. S. Bhalla, et al. (2012). "Finite element modeling of acousto-optic effect and optimization of the figure of merit." 849703-849703.

6.1 Introduction

A study of the acousto-optic (AO) effect in a family of oxide crystals (including e.g., TiO₂, ZnO, LiNbO₃, and ferroelectric perovskites) as well as semiconductors has been conducted by finite element analysis method. In addition, the acousto-optic figure of merit (FOM) as a function of material's refractive index, density, effective AO coefficient and the velocity of the acoustic wave in the material, is also investigated. By examining the directional dependent velocity, acousto-optic coefficients, and refractive index, the acousto-optic FOM can be calculated and plotted in all directions revealing the optimal crystal orientation to maximize coupling between the optical and acoustic waves. A finite element model was developed to corroborate the improved interaction. The model examines the diffraction that occurs on the optical wave as it travels through an acousto-optic medium. The combined information gained from Mathematica and COMSOL Multiphysics-based modeling is shown to be an effective means of predicating acousto-optic device functionality.

There are two types of photoelasticity, the piezo-optic effect and the elasto-optic effect. Pressure can change the refractive index of a material both through the density and through the polarizability. When a material is compressed the atoms move closer together and the refractive index increases but at the same time the electrons are bound more tightly which reduces polarizability and reduces the refractive index. For this reason and because the two effects are on the same order of magnitude, pressure can increase or decrease the refractive index depending on the material[24].

$$\text{Piezo-optic } \Delta B_{ij} = \pi_{ijkl} X_{kl} \quad (6.1)$$

$$\text{Elasto-optic } \Delta B_{ij} = p_{ijkl} x_{kl} \quad (6.2)$$

Where π_{ijkl} is known as piezo-optic coefficient that is defined by stress (X_{kl}) induced changes in optical indicatrix ΔB_{ij} . Similarly p_{ijkl} is known as elasto-optic coefficient that is defined by strain (x_{kl}) induced changes in optical indicatrix ΔB_{ij} . The acousto-optic figure of merit (FOM) is a measure of the suitability of a material to modulate the diffraction intensity. The refractive index, elasto-optic coefficient, density and acoustic wave velocity are all used in this calculation but it is the refractive index and acoustic wave velocity that are the dominant factors. The slower the acoustic and optical waves in the material the more interaction possible[24]. There are other figures of merit related to acousto-optic devices however the FOM used in Equa.(6.3) is used primarily for gauging the power efficiency of AO materials and is not for example used to determine the usable bandwidth of a the device[25].

$$M_2 = \frac{n^6 p^2}{\rho v^3} \quad (6.3)$$

6.2 Importance

The acousto-optic effect is used in many devices including modulators, frequency shifters, filters and beam deflectors. AO modulators are used in many nanosecond pulsed lasers for Q-switching. The modulator is used inside the laser cavity to remove the cavity feedback until a large population inversion is built up. Beam deflecting modulators can be used for laser graphics projectors, optical tweezers, and optical switching. Acoustic devices are also widely used for medical imaging due to the excellent penetration depth of acoustic waves.

6.3 Recent Status

Recent research in acousto-optics has included higher frequency acoustic interaction and metamaterials. Though there are many types of metamaterials the designation “meta” is typically used to refer to a material with negative permittivity and permeability. This configuration is usually created by some type of resonance or periodic condition in the material and can result in the group velocity of a wave in the material being positive while the phase velocity is negative[26]. Current interest in acousto-optics encompasses a wide range of research for low power consumption, modeling techniques, biological applications, integration with photonic crystals, integrated optics, and MEMS, etc. It is highly desirable to give a comprehensive picture of all these property coefficients in relation to their point group symmetries and do so by demonstrating such capability in some important and well established materials.

6.4 Approach

The necessary parameters for calculating the figure of merit of several common materials are listed in Table 6.1 through

Table 6.6. Table 6.1 and Table 6.2 give the elasto-optic coefficients which have no units. To calculate the elastic wave velocity in linear elastic materials (such as TiO_2 and PbMoO_4) only the elastic stiffness coefficients c_{ij} and the density ρ are needed; however for piezoelectric materials consideration of the piezoelectric coupling coefficients e_{ij} , and the permittivities ϵ_{ij} are also required. The material coefficients listed are from sources [9, 24, 27-30].

Table 6.1 Elasto-optic coefficients – of unitless – Part A

	p_{11}	p_{12}	p_{13}	p_{14}	p_{16}	p_{31}
LiNbO_3	-0.026	0.09	0.133	-0.075	-	0.179
TiO_2	-0.001	0.113	-0.167	-	-	0.106
ZnO	0.222	0.0999	-0.111	-	-	0.0888
PbMoO_4	0.24	0.24	0.225	-	0.017	0.175
GaAs	-0.165	-0.14	-	-	-	-
GaP	-0.151	-0.082	-	-	-	-
Ge	0.27	0.235	-	-	-	-

Table 6.2 Elasto-optic coefficients – of unitless – Part B

	p_{33}	p_{41}	p_{44}	p_{45}	p_{61}	p_{66}	Ref.
LiNbO ₃	0.0171	-0.151	0.146	-	-	-	[24]
TiO ₂	-0.064	-	0.0095	-	-	-0.066	[24]
ZnO	-0.235	-	0.0585	-	-	-	[31]
PbMoO ₄	0.3	-	0.067	-0.01	0.013	0.05	[32]
GaAs	-	-	-0.072	-	-	-	[24]
GaP	-	-	-0.074	-	-	-	[24]
Ge	-	-	0.125	-	-	-	[30]

Table 6.3 Elastic coefficients –of units of 10^{11} [N/m²]

	c_{11}	c_{12}	c_{13}	c_{14}	c_{16}	c_{33}	c_{44}	c_{66}	Ref.
LiNbO ₃	2.03	0.53	0.75	0.09	-	2.45	0.6	-	[33]
TiO ₂	2.7143	1.7796	1.4957	-	-	4.8395	1.2443	1.9477	[34]
ZnO	2.097	1.211	1.051	-	-	2.109	0.4247	-	[35]
PbMoO ₄	1.09	0.68	0.53	-	-0.14	0.92	0.267	0.335	[36]
GaAs	1.1877	0.5372	-	-	-	-	0.5944	-	[37]
GaP	1.412	0.6253	-	-	-	-	0.7047	-	[38]
Ge	1.2835	0.4823	-	-	-	-	0.6666	-	[39]

Table 6.4 Piezoelectric coupling coefficients – of units of [C/m²]

	e_{11}	e_{14}	e_{15}	e_{22}	e_{31}	e_{33}	Ref.
LiNbO ₃	-	-	4.1607	2.442	0.8661	3.7	[24]
ZnO	-	-	-0.352501	-	-0.35706	1.56416	[24]
GaAs	-	0.154544	-	-	-	-	[24]
GaP	-	0.1	-	-	-	-	[29]

Table 6.5 Relative dielectric permittivity coefficients – of unitless

	ϵ_{11}	ϵ_{33}	Ref.
LiNbO ₃	43.6	29.16	[28]
ZnO	8.5446	10.204	[28]
GaAs	12.459	-	[28]
GaP	11.1	-	[28]

Table 6.6 Refractive index coefficients and density – density of units of $[\text{kg/m}^3]$

	n_{11}	n_{33}	Ref.	ρ $[\text{kg/m}^3]$	Ref.
LiNbO ₃	2.232	2.156	[9]	4644	[9]
TiO ₂	2.584	2.872	[9]	4260	[9]
ZnO	2.015	1.998	[9]	5606	[9]
PbMoO ₄	2.2584	2.3812	[9]	6920	[9]
GaAs	3.37	-	[9]	5340	[9]
GaP	3.35	-	[9]	4130	[9]
Ge	4.0	-	[30]	5330	[30]

Typically AO materials are chosen based on both their availability and their figure of merit. Some of the most commonly used materials are Lithium Niobate (LiNbO₃), Lithium Tantalate (LiTaO₃), Lead Molybdate (PbMoO₄), paratellurite (TeO₂), fused silica (SiO₂), Rutile (TiO₂), Zinc Oxide (ZnO), and Gallium Arsenide (GaAs). Many other materials are also used that have high figures of merit. This paper will consider Lithium niobate, Rutile, Zinc Oxide (Wurtzite), Lead Molybdate, Gallium Arsenide, Gallium Phosphide, and Germanium due to the availability of data. The developed capability can be readily extended to advanced materials upon the availability of needed physical parameters.

Plotting of the directionally dependent material properties is more readily done in the spherical coordinate system. Using spherical coordinates the direction (Z'_1) relative to the Cartesian system of Z_1 , Z_2 , and Z_3 is the angle φ from the Z_1 axis on the Z_1 - Z_2 plane and the angle theta θ from the Z_3 axis as depicted in Figure 6.1. Additionally the radius (i.e. length of the Z'_1 vector) represents the magnitude of the effect.

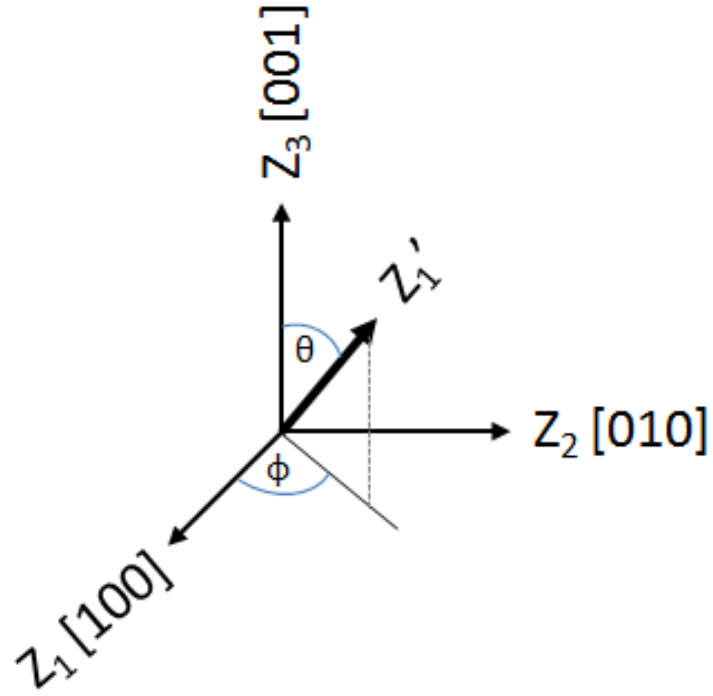


Figure 6.1 Conversion scheme of Cartesian coordinate system to spherical coordinates

The elasto-optic effect is a 4th rank tensor property that can be fully described with a 6x6 matrix using Voigt notation. To analyze longitudinal directional dependence of elasto-optic effect (p'_{iii}) about an arbitrary direction (i -direction), the 6x6 “ α -matrix” is used. Other effects such as the refractive index can be evaluated by way of the 3x3 transformation “ a -matrix”. Both the “ α ” and “ a ” matrices are made up of the directional cosine elements a_{ij} as seen in the equations below.

$$\begin{aligned}
 a_{11} &= \sin\theta \cos\phi \\
 a_{12} &= \sin\theta \sin\phi \\
 a_{13} &= \cos\theta \\
 a_{21} &= \cos\theta \cos\phi \\
 a_{22} &= \cos\theta \sin\phi \\
 a_{23} &= -\sin\theta \\
 a_{31} &= -\sin\phi \\
 a_{32} &= \cos\phi \\
 a_{33} &= 0
 \end{aligned} \tag{6.4}$$

$$a = \begin{pmatrix} a_{11} & a_{12} & a_{13} \\ a_{21} & a_{22} & a_{23} \\ a_{31} & a_{32} & a_{33} \end{pmatrix} \quad (6.5)$$

$$\alpha = \begin{pmatrix} a_{11}^2 & a_{12}^2 & a_{13}^2 & 2a_{12}a_{13} & 2a_{13}a_{11} & 2a_{11}a_{12} \\ a_{21}^2 & a_{22}^2 & a_{23}^2 & 2a_{22}a_{23} & 2a_{23}a_{21} & 2a_{21}a_{22} \\ a_{31}^2 & a_{32}^2 & a_{33}^2 & 2a_{32}a_{33} & 2a_{33}a_{31} & 2a_{31}a_{32} \\ a_{21}a_{31} & a_{22}a_{32} & a_{23}a_{33} & a_{22}a_{33} + a_{23}a_{32} & a_{21}a_{33} + a_{23}a_{31} & a_{22}a_{31} + a_{21}a_{32} \\ a_{31}a_{11} & a_{32}a_{12} & a_{33}a_{13} & a_{12}a_{33} + a_{13}a_{32} & a_{13}a_{31} + a_{11}a_{33} & a_{11}a_{32} + a_{12}a_{31} \\ a_{11}a_{21} & a_{12}a_{22} & a_{13}a_{23} & a_{12}a_{23} + a_{13}a_{22} & a_{13}a_{21} + a_{11}a_{23} & a_{11}a_{22} + a_{12}a_{21} \end{pmatrix} \quad (6.6)$$

The value of p'_{iii} can be calculated using Equa. (6.7), by multiplying α by the material matrix p (whose components are defined by its crystallographic axis) and again by the transpose of the α matrix and extracting the top left element (1,1).

$$p'_{iii}(\theta, \varphi) = \alpha p \alpha^T \llbracket 1,1 \rrbracket \quad (6.7)$$

In the following text the direction of tensile strain is designated as i - (1-) direction and the physical meaning of the p'_{1111} is the amplitude of longitudinal effective elastooptic effect. A plot of $p'_{iii}(\theta, \varphi)$ is a graphical representation of its directional dependence. p'_{iii} is plotted as a function of theta and phi, for θ from 0 to π and ϕ from 0 to 2π .

The refractive index (represented as a 3x3 matrix) is found in a similar manner as to the elasto-optic effect but now using the “a” matrix.

$$n'_{ii}(\theta, \varphi) = a n a^T \llbracket 1,1 \rrbracket \quad (6.8)$$

The sound velocity in a homogeneous anisotropic medium has multiple solutions for any given wave propagation orientation and thus requires a different method of evaluation as compared to the aforementioned elasto-optic and refractive index. Typically there is one longitudinal wave with vibration direction parallel to propagation and two transversal shear waves. In a non-center-symmetric material each of the wave components may be also accompanied by oscillating polarizations coupled through piezoelectric effect. Acousto-optic materials can be either linear elastic or piezoelectric. The velocity of linear elastic materials is determined by orientation,

density, and the elastic constants, piezoelectric materials however must also consider the piezoelectric coupling matrix and permittivity. Only in a few circumstances are the waves considered to be pure that is with polarization either perfectly parallel or perpendicular to the propagation directions and are more typically either quasi-longitudinal or quasi-transverse especially in materials of low symmetry.

The modified Christoffel equation used to find the wave velocities is shown below. The tensor C_{ik} represents the linear elastic portion and is a product of the inverse density $1/\rho$, the elastic tensor c_{ijkl} and the directional cosines $N_i N_j$. The C_i C_k tensors and constant C represent the velocity adjustment resultant from the piezoelectric contribution. e_{mij} is the piezoelectric coupling tensor and ε_{mj} the permittivity. It is important to note that ε here is not the relative permittivity but rather the absolute permittivity $\varepsilon = \varepsilon_0 \varepsilon_r$ in F/m, the velocity is v , δ_{ik} is the Kronecker delta ($\delta_{ik} = 1$ if $i = k$ and zero otherwise), and u_k is the amplitude of the lattice displacement in k -direction.

$$\left(C_{ik} + \frac{C_i C_k}{C} - v^2 \delta_{ik} \right) u_k = 0 \quad (6.9)$$

$$C = \rho N_m \varepsilon_{mj} N_j \quad (6.10)$$

$$C_{ik} = \frac{1}{\rho} c_{ijkl} N_j N_l \quad (6.11)$$

$$C_i = N_m e_{mij} N_l \quad (6.12)$$

$$N_1 = \sin \theta \cos \varphi \quad (6.13)$$

$$N_2 = \sin \theta \sin \varphi \quad (6.14)$$

$$N_3 = \cos \theta \quad (6.15)$$

For clarity these tensor components for the general (triclinic) case are written explicitly below

$$C_{11} = \frac{1}{\rho} (c_{11}N_1^2 + c_{66}N_2^2 + c_{55}N_3^2 + 2c_{56}N_2N_3 + 2c_{15}N_3N_1 + 2c_{16}N_1N_2) \quad (6.16)$$

$$C_{22} = \frac{1}{\rho} (c_{66}N_1^2 + c_{22}N_2^2 + c_{44}N_3^2 + 2c_{24}N_2N_3 + 2c_{46}N_3N_1 + 2c_{26}N_1N_2) \quad (6.17)$$

$$C_{33} = \frac{1}{\rho} (c_{55}N_1^2 + c_{44}N_2^2 + c_{33}N_3^2 + 2c_{34}N_2N_3 + 2c_{35}N_3N_1 + 2c_{45}N_1N_2) \quad (6.18)$$

$$C_{23} = \frac{1}{\rho} (c_{56}N_1^2 + c_{24}N_2^2 + c_{34}N_3^2 + (c_{23} + c_{44})N_2N_3 + (c_{36} + c_{45})N_3N_1 + (c_{25} + c_{46})N_1N_2) \quad (6.19)$$

$$C_{13} = \frac{1}{\rho} (c_{15}N_1^2 + c_{46}N_2^2 + c_{35}N_3^2 + (c_{36} + c_{45})N_2N_3 + (c_{13} + c_{55})N_3N_1 + (c_{14} + c_{56})N_1N_2) \quad (6.20)$$

$$C_{12} = \frac{1}{\rho} (c_{16}N_1^2 + c_{26}N_2^2 + c_{45}N_3^2 + (c_{25} + c_{46})N_2N_3 + (c_{14} + c_{56})N_3N_1 + (c_{12} + c_{66})N_1N_2) \quad (6.21)$$

$$C_1 = e_{11}N_1^2 + e_{26}N_2^2 + e_{35}N_3^2 + (e_{25} + e_{36})N_2N_3 + (e_{15} + e_{31})N_3N_1 + (e_{16} + e_{21})N_1N_2 \quad (6.22)$$

$$C_2 = e_{16}N_1^2 + e_{22}N_2^2 + e_{34}N_3^2 + (e_{24} + e_{32})N_2N_3 + (e_{14} + e_{36})N_3N_1 + (e_{12} + e_{26})N_1N_2 \quad (6.23)$$

$$C_3 = e_{15}N_1^2 + e_{24}N_2^2 + e_{33}N_3^2 + (e_{23} + e_{24})N_2N_3 + (e_{13} + e_{35})N_3N_1 + (e_{14} + e_{25})N_1N_2 \quad (6.24)$$

$$C = \rho(\varepsilon_{11}N_1^2 + \varepsilon_{22}N_2^2 + \varepsilon_{33}N_3^2 + 2\varepsilon_{23}N_2N_3 + 2\varepsilon_{13}N_3N_1 + 2\varepsilon_{12}N_1N_2) \quad (6.25)$$

The method of calculation is more easily seen by converting the Christoffel Equation to matrix form and inserting the above relations to form the matrix A below. The velocities are now simply the square root of the eigenvalues of the matrix A and the corresponding wave polarizations are from the eigenvectors of A. The eigenvalues of A always exist but the eigenvectors may not always be determinant for all directions.

$$A = \begin{bmatrix} C_{11} & C_{12} & C_{13} \\ C_{12} & C_{22} & C_{23} \\ C_{23} & C_{13} & C_{33} \end{bmatrix} + \begin{bmatrix} C_1^2 & C_1C_2 & C_3C_1 \\ C_1C_2 & C_2^2 & C_2C_3 \\ C_3C_1 & C_2C_3 & C_3^2 \end{bmatrix} \cdot \frac{1}{C} \quad (6.26)$$

6.5 Results and Discussion

Mathematica has been used to provide a three dimensional visualization of the elasto-optic effect for a crystal of any point group symmetry. One can select the point group and then from a library of material data associated with that group. The directionally dependent Figure of

Merit for four chosen materials is shown in Figure 6.2 below. All results in the figure are in terms of 10^{-15} [s³/kg]. Note that the negative Cartesian coordinates are for reference and do not indicate a negative figure of merit

$$M_2(\theta, \varphi) = \frac{n'_{ii}(\theta, \varphi)^6 p'_{iii}(\theta, \varphi)^2}{\rho v_L(\theta, \varphi)^3} \quad (6.27)$$

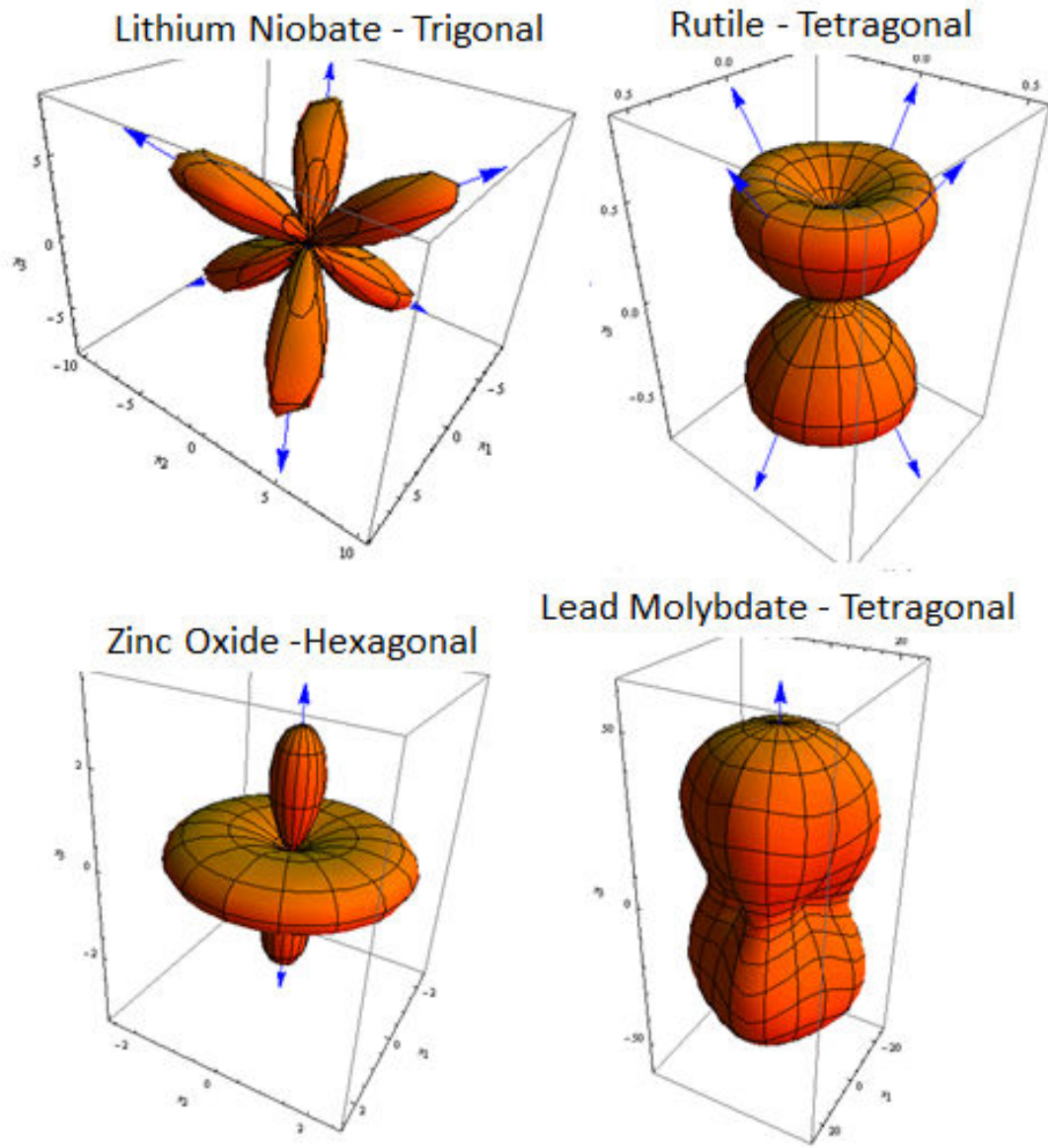


Figure 6.2 Directional dependence of elasto-optic figure of merit M_2 calculated for several example materials representing different crystal systems

Others have published on the directional dependence of the elasto-optic effect [40] and the piezo-optic effect [41] but only for a few materials and not all have considered the figure of merit directional dependence. Mathematica was used to calculate the figure of merit by

combining the effects of density elasto-optics, acoustic velocity and refractive index (Figure 6.2). It is typical for FOM calculations to show M_2 as divided by the FOM of isotopic fused silica ($M_2=1.51 \times 10^{-15} \text{ [s}^3/\text{kg}]$) thus giving a unitless relative value.

The figure of merit is typically used to compare or gauge the effectiveness of AO materials; however it can also be used to determine the ideal material orientation for maximum acoustic/optic coupling. The elasto-optic matrix is certainly the dominant factor in determining idea coupling; however as can be seen in the FOM calculation the refractive index and the velocity are directionally dependent they can also have a significant impact on coupling. The results of this evaluation are consistent with those from Chang [30] with relative M_2 of GaAs ($M_2=69$), GaP ($M_2=29.5$), Ge ($M_2=482$). Our results for GaAs, GaP and Ge are respectively 64.3, 30.5, and 510.3 demonstrating good agreement and verification of the methodology developed. Figure 6.3 shows the FOM of GaAs in the Z_1 - Z_2 plane and a close match to the literature value reported for the [110] direction. Furthermore, this work permits a full view of the directional dependence in any direction interested, a powerful feature not previously available.

The three dimensional representations (Figure 6.2) can be used to effectively determine the maximum coupling orientation. Using this information the ideal material orientations have been determined for each of the materials and summarized in Table 6.7. The values are listed for $0 \leq \theta < \pi/2$ and $0 \leq \varphi < 2\pi$; there are corresponding maximum orientations for $\theta > \pi/2$ only as additional directions can be easily generated based on given symmetry.

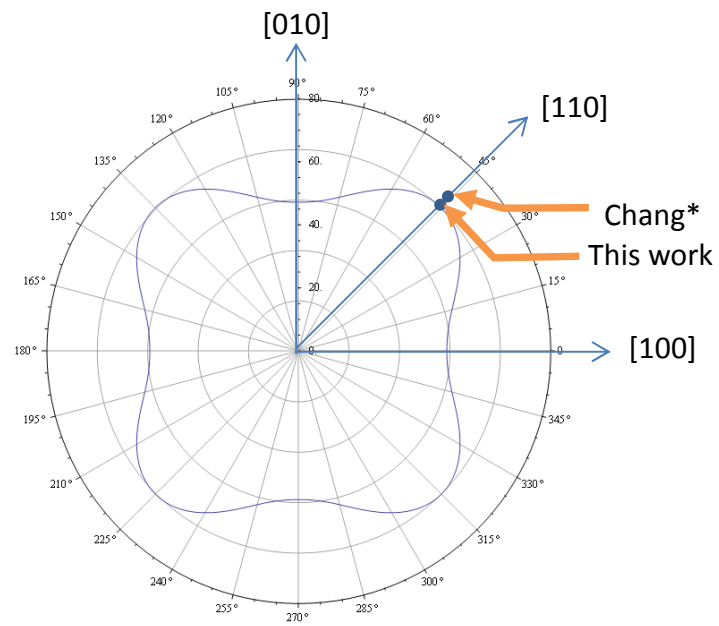


Figure 6.3 Relative acousto-optic figure of merit of Gallium Arsenide in Z_1 - Z_2 plane and comparison to the literature value reported in the $[110]$ direction

Table 6.7 Maxima of Figure of Merit for each material with associated property in the same direction. Theta and phi are in degrees

	p_{ii}	n	v [m/s]	ρ [kg/m ³]	M_2 [10^{-15} s ³ /kg]	M_2 relative	(θ, ϕ)
LiNbO ₃	0.340	2.203	6487.6	4644	10.418	6.899	(51.7,90.0) (51.7,210.0) (51.7,330.0)
TiO ₂	-0.081	2.782	10079.5	4260	0.694	0.46	(34.1,0) (34.1,90) (34.1,180) (34.1,270)
ZnO	-0.235	1.998	6133.5	5606	2.716	1.799	(0,0)
	0.222	2.015	6116.1	5606	2.572	1.703	(90,any)
PbMoO ₄	0.300	2.381	3646.2	6920	48.909	32.39	(0,0)
GaAs	-0.244	3.37	5381.6	5340	105.066	69.580	(54.7,45) (54.7,135) (54.7,225) (54.7,315)
GaP	-0.204	3.35	6651.4	4130	48.242	31.949	(54.7,45) (54.7,135) (54.7,225) (54.7,315)
Ge	0.413	4.0	5543.5	5330	770.526	510.282	(54.7,45) (54.7,135) (54.7,225) (54.7,315)

A COMSOL model was developed to examine the zero order diffraction in an acousto-optic modulator and the improved efficiency that can result from properly orienting the AO crystal accurately as designed. A typical configuration for an AO modulator is seen in Figure 6.4. The incident optical beam comes in from the top medium (air) at an angle α to the normal of the surface where reflection, refraction, and diffraction occur. A periodic strain change causes diffraction of the beam. The acousto-optic modulator can result in modulation of the amplitude, the deflection angle as well as frequency shifting or wavelength filtering [42]. The setup of the piezoelectric and electromagnetic domains for the COMSOL model is shown in Figure 6.5. This model uses an initial strain defined in the mechanical (piezoelectric) portion that is then coupled

to the optical model (RF) through the elasto-optic effect on the refractive indices. The simulation took Lithium Niobate as an example which has 3m trigonal symmetry. A periodically changing strain is defined in the AO material; the strain is oriented in the out-of-plane direction but changes spatially across the x dimension. Furthermore, the optical polarization is in the out-of-plane direction meaning that this is a configuration corresponds to the longitudinal calculations as evaluated in the previous sections where the optical and piezo-acoustic polarizations are parallel to each other. When evaluated using COMSOL model developed, one can calculate the resulting strain distribution in the AO material and the optical wave propagation in the periodically poled structure, as illustrated in Figure 6.6.

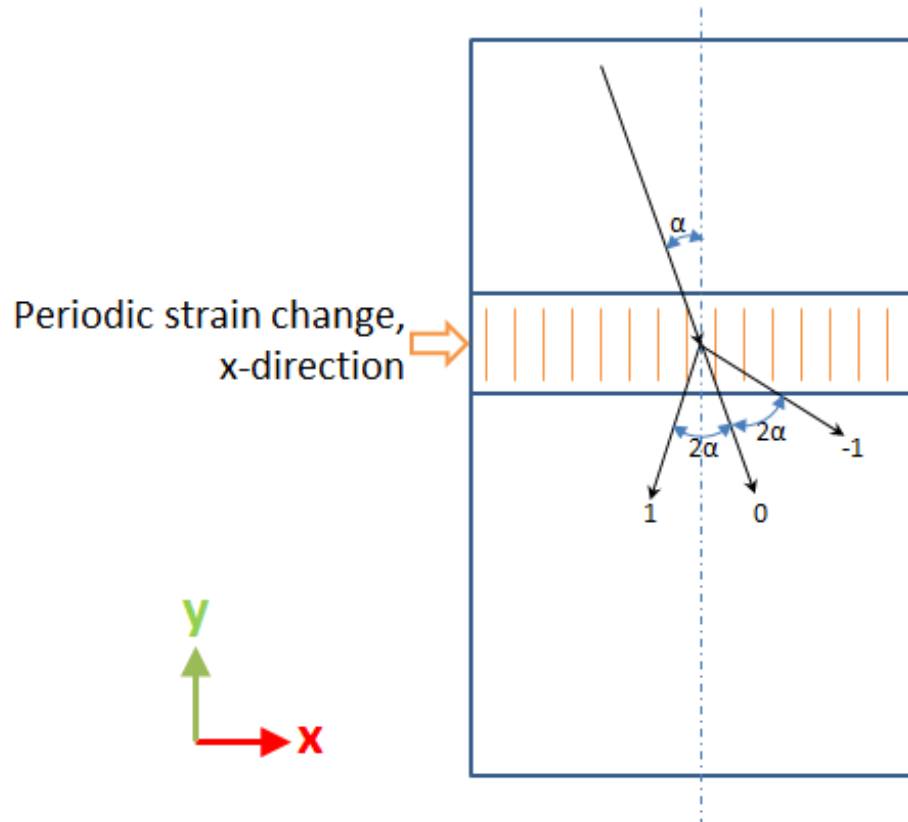


Figure 6.4 A typical example of an acousto-optic modulator configuration

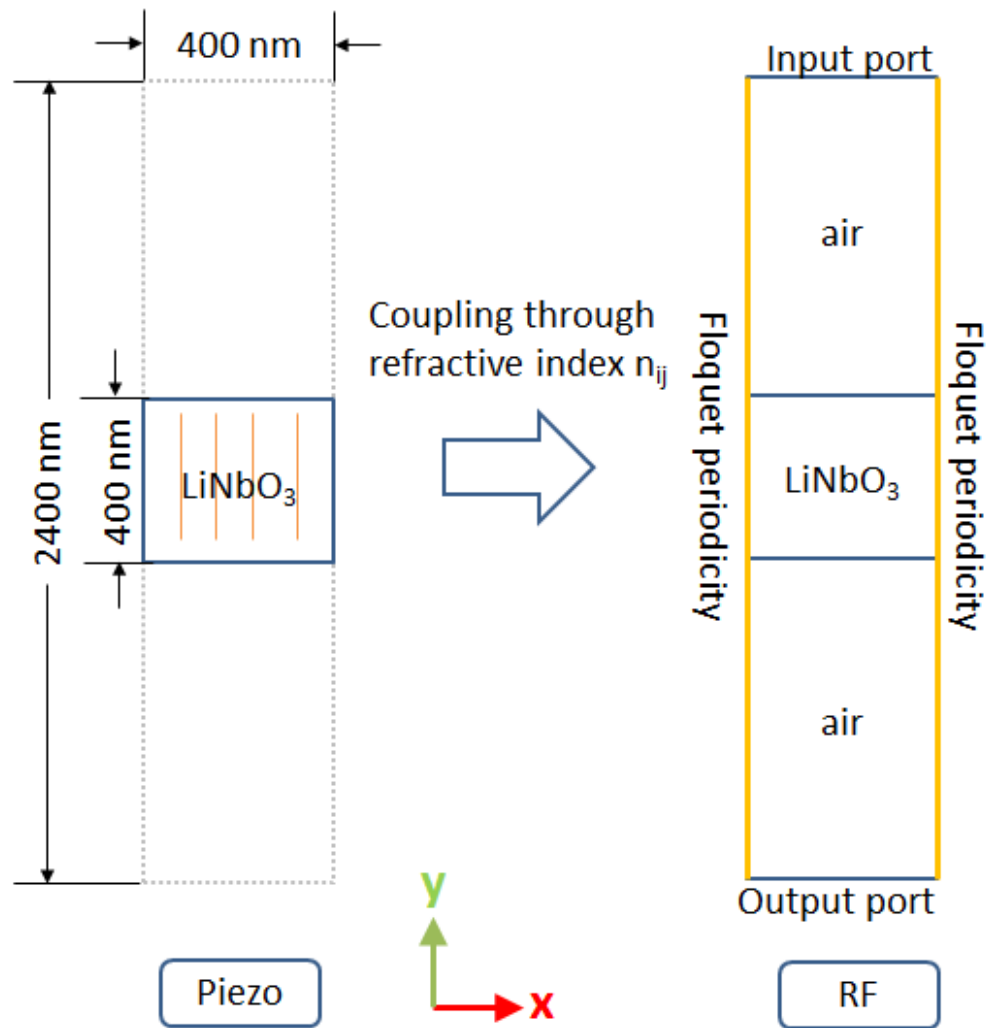


Figure 6.5 The setup of the piezoelectric and electromagnetic domains for the COMSOL FEA acousto-optic model

Notice that the incident signal is refracted at the top air:material interface and then again at the bottom and that the wavelength is smaller inside the AO material. The simulation results presented in Figure 6.6 is obtained using COMSOL model for zero order diffraction only considering only waves transmitting through the material. The z component (out of plane) of the electric field is plotted. The angle of incidence is $\alpha=0.7$ radians.

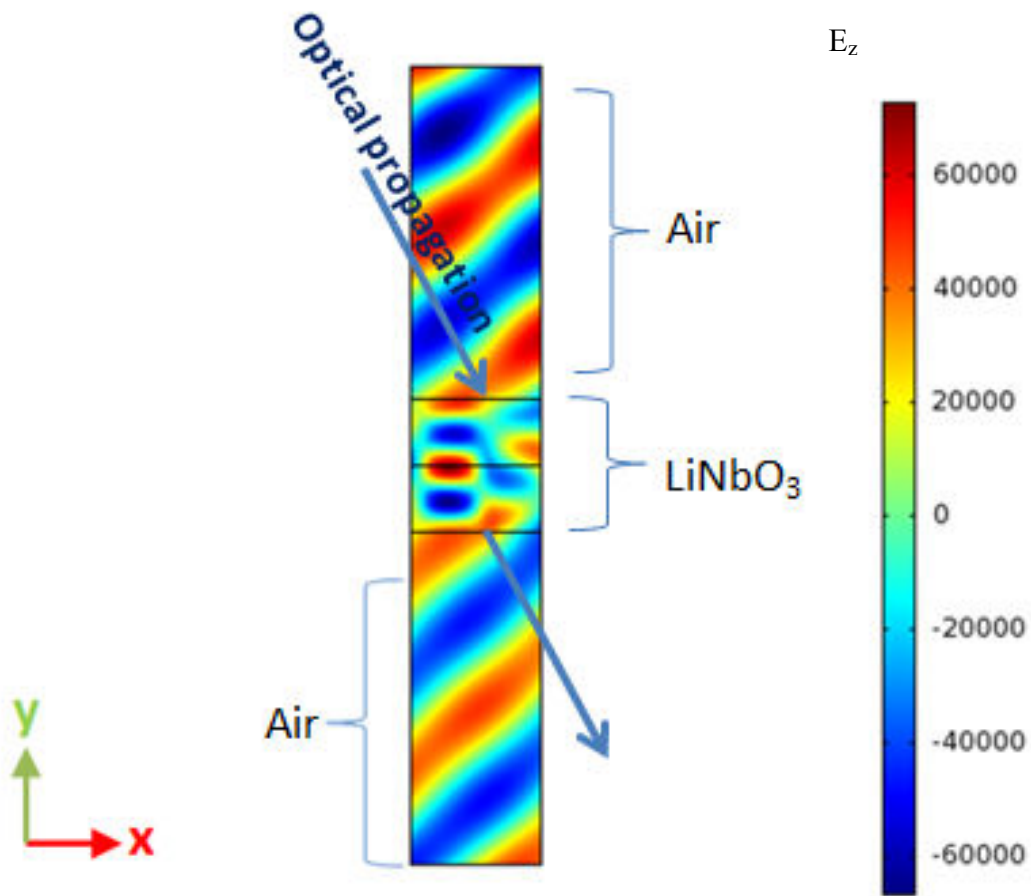


Figure 6.6 COMSOL simulation of the optical propagation from the top section (air) into the material and to the bottom port

6.6 Summary

This work demonstrates the usefulness of examination of the AO orientation dependence. The elasto-optic effects and figure of merit can be obtained for any crystal class, and the maximum directions of interaction can be inspected. Of the materials investigated only two showed maximum interaction along the principle Cartesian axes demonstrating the importance of a proper crystal cut for ideal interaction. Germanium gives the largest FOM among the crystals evaluated, while there are many other materials that give larger interaction are candidate to be evaluated using the method. The elasto-optic tensor itself does not always provide accurate view of the best direction for AO interaction, this modeling approach allows for a more reliable method of determining the best acousto-optical coupling. The COMSOL model provides verification of these results and the possibilities to tailor materials for improved performance.

CHAPTER 7: FUTURE WORK

7.1 Introduction

This work describes many ways of using and studying the enhanced electro-optic interaction available under piezo-resonance; yet there are still many other directions to which this subject can be extended.

There is certainly more work that could be done on resonance induced transmission enhancement as described in section 3.7. Using a high field signal generator will allow for a more complete study of the possible improved optical transparency that may result from proper modulation at certain resonant modes. Moving in to this area may show the potential of using this effect for optical shutters.

Due to the significant increase in coupling the sensitivity of these devices may be high enough to pick up radio frequency signals without active amplification. Such a configuration where an antenna and perhaps a few passive components are connected to the sample material may allow coupling of the radio wave to modulate the sample directly. This configuration would have a direct application for radio over fiber technology. Radio over fiber uses long optical fibers to connect local radio communication and currently require individually powered OEO conversion points. The development of passive nodes that directly impress the radio signal on to the fiber could be very advantageous.

Most work on resonance enhancement thus far has been concentrated below about 20 MHz and has been limited by the test equipment used; it would be interesting to investigate how high enhancement can go. To do this a different testing configuration will be needed. One possibility is to use a traveling wave electrode configuration such as those used in commercial RF fiber optic modulators. This configuration may work well because wide bandwidth

modulation is possible; however adapting this configuration to resonate the modulators has been found to be difficult. Another possibility is using a microwave cavity such as used in [43-45]. This method is discussed in detail in section 7.1.

There is also some significant potential for using this technology for developing a phonon-plasmon (defined in Section 7.3.1) metamaterial device. The resonant enhanced process can produce a periodic charge distribution analogous to the surface plasmon widely studied on metallic surfaces. This method is discussed in detail in section 7.2.

7.1 Resonance Enhanced Electro-Optic Coefficient by means of a Microwave Cavity

Here a rectangular cavity under measurement is set at transverse electric mode 103 (TE_{103}). The sample is typically placed in the location of most positive slope as shown in Figure 7.1. When the sample is placed at a point of monotonic slope change there is an induced refractive index change in the sample (Huang *et al.* [44]). Additionally a laser was used and coupled through a small hole at both ends of the waveguide, thus a microwave field is induced on the sample and the optical output can be measured. This refractive index change will cause the optical laser pulse to shift in frequency which is the same as a narrowing or widening the pulse in the time domain which is determined by measuring its full width at half max (FWHM) prior and after traversing the waveguide. By adjusting the power of the network analyzer and monitoring the photodetector voltage a linear relationship change be observed between optical transmission intensity squared (I^2) and the shifted pulse; the slope of which is proportional to the EO coefficient. This experiment could be modified by applying electrodes to the sample and modulating at the resonant frequency of the sample. This technique may allow for an observed increase in the coupling measurable in the microwave range which could have significant impact on microwave electro-optic communications systems. There are two drawbacks to this approach.

The first is that only a few frequencies can be tested, i.e. only the resonant frequencies of the waveguide. The second issue is that the use of a sample with parallel plate electrodes inside the waveguide may disturb field distributions that are difficult to predictor demand high field strength. There has been some work to model the waveguide with inserted sample using finite element analysis done by the author and it is included in the appendix of this dissertation. The appendix focuses on a method of determining the microwave anisotropic permittivities of samples. Determining microwave permittivity is key to an accurate modeling of the electroded electro-optic sample in the waveguide and to the characterization of the high frequency response of the sample.

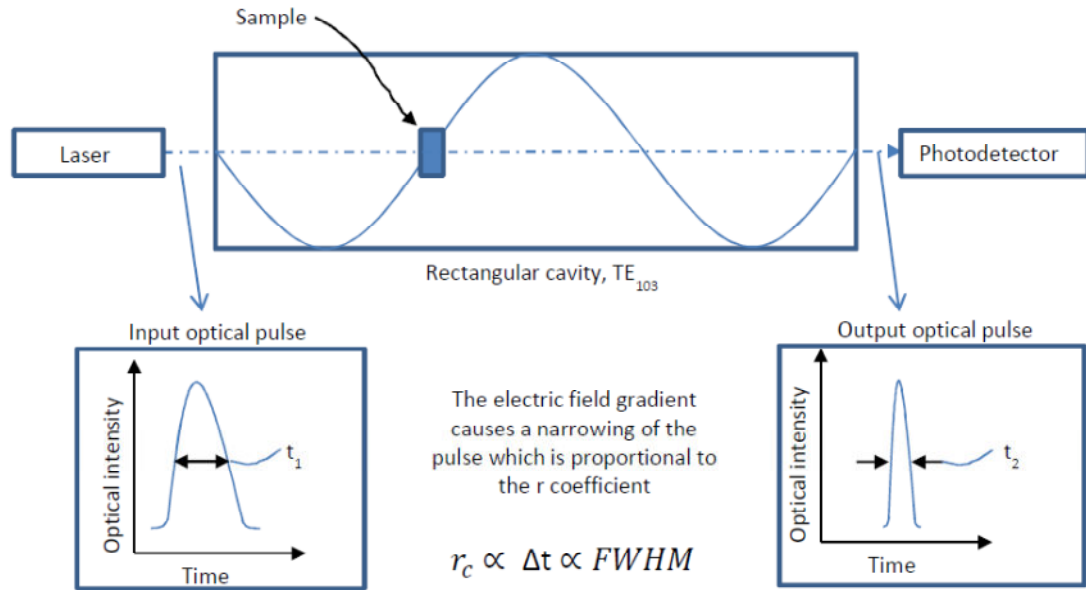


Figure 7.1 Microwave cavity electro-optic measurement technique [44]

7.3 Acousto-optic Metamaterials

7.3.1 Plasmonics

Plasmons are electron density waves and can be in the form of surface or bulk plasmons. Surface plasmons can exist on the interface between a metal and dielectric; this is a sufficient condition but not necessary. The wave must be on the interface of two materials with complex permittivity of opposite sign, the sum of their permittivity must be negative [46]. The plasmon frequency ω_p is the point where the electron gas of a plasmon has strong vibrations. Higher electron density results in this frequency also being high. The plasmon energy (in electron volts) is calculated from this frequency $E_p = \hbar\omega_p$ and at this energy the external field vibration is so fast that the electrons in the metal cannot follow and the metal stops being reflective.

7.3.2 Metamaterials and Cloaking

Metamaterials in the most general sense are manmade or engineered materials that are non-homogenous. Most commonly this term applies to negative index materials; however that is just one type of metamaterial. As described by Smith, D. R., J. B. Pendry, *et al.* [47] conventional materials have properties that derive from their constituent atoms while the properties of metamaterials are from their constituent units. Metamaterials are used to influence the wave interaction with a material, as long as the size and spacing is small compared to the wavelength such that the wave cannot tell the difference between an engineered group of objects or a homogeneous medium. Another class of these materials is known as transformative optics. These materials have an anisotropic refractive index that changes spatially in the material.

Metamaterial devices can be designed to create a “cloaking” effect, or obstructing the wave propagation altering the perception of the “normal” detection. The Electromagnetic wave is caused to bend around the object and render it invisible to a far away observer. The resonant

enhanced devices discussed in this dissertation are known to increase the transmission of the device and could potentially be used in a similar way to the aforementioned metamaterials to provide dynamically adjustable cloak. Typical cloaking device configurations [48, 49] disguise a dielectric cylinder with a larger cloaking material outside of the cylinder. When a plane wave hits the cloak the wave bends around and reforms on the other side as if the cylinder and cloak were never there. Were the cloak not in place the wave would scatter causing an observer on the opposite side to see a shadow. Alternatively the resonance enhanced technology may be able to achieve this type of interaction with the added benefit of dynamic control. As seen in the figure below the current configuration uses a vibrating crystal plus external optics to control transmission. Because the transmission is induced dynamically by the piezoelectric resonance it can be easily turned on and off causing the object to go from visible to invisible. The figure demonstrates the concept of the scattering of the incident wave. Turning the cloak on results in a minimum scattering cross section (SCS), when scattering is small an observer on the opposite side of the object (relative to the applied wave) would not see the shadow of the object.

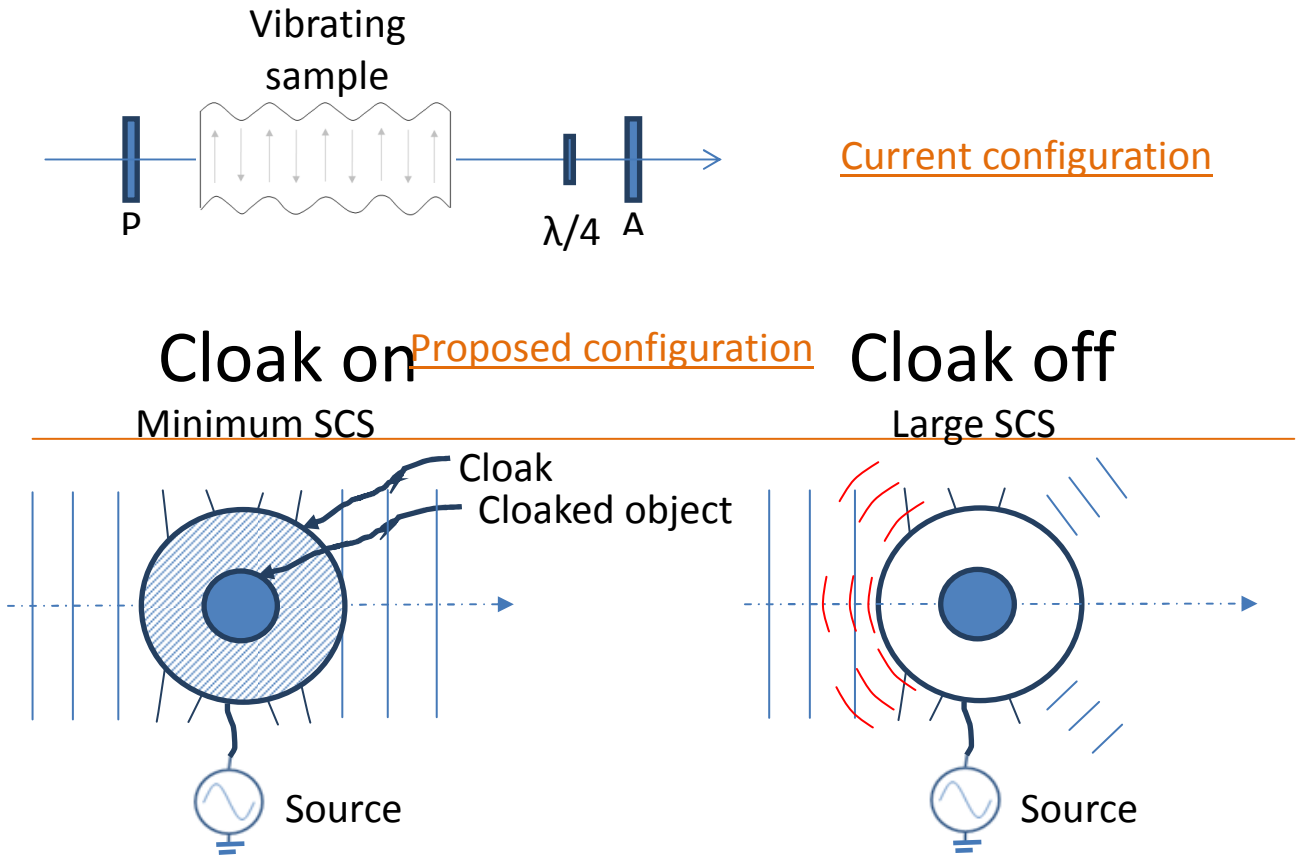


Figure 7.2 Proposed configuration for achieving piezo-resonance induced optical cloaking

7.3.3 Proposed Phonon-Plasmon Meta-Device

To study this effect and move the research in the direction of plasmonics and metamaterials a structure is proposed. This structure will make use of surface acoustic waves as seen in Figure 7.3. In this configuration coplanar interdigitized electrodes are used to induce a surface wave by way of the piezoelectric effect. A high frequency signal is applied to one set of electrodes and the other is grounded. The induced elastic wave will travel across the surface from left to right in the figure and a periodic strain will be induced. The periodic strain results in local stress through the fourth rank elastic stiffness tensor c_{ijkl} .

$$X_{ij} = c_{ijkl}x_{kl} \quad (7.1)$$

The stress is converted to a polarization by the direct piezoelectric effect (Equation (3.3)).

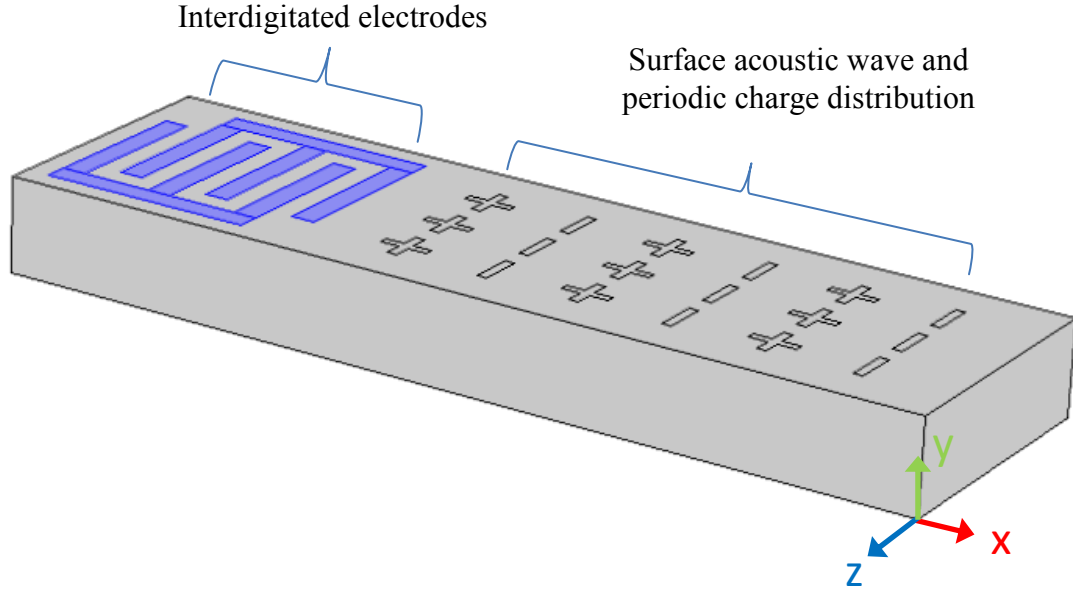


Figure 7.3 Proposed surface acoustic wave device to launch wave and induce a periodic polarization

The induced periodic charge distribution may be a vehicle to allow propagation and enhancement of the plasmon wave. This will require a surface charge of sufficient amplitude and proper periodicity. A proposed test scheme for experimentally verifying this interaction [50] is shown in Figure 7.4. A signal generator is used to control the SAW device and induce the periodic charges. A tunable laser is used to launch the plasmon on the device surface and a spectrometer picks up the signal. A vibrometer is also integrated in this experiment which can be used to verify the existence of the surface wave.

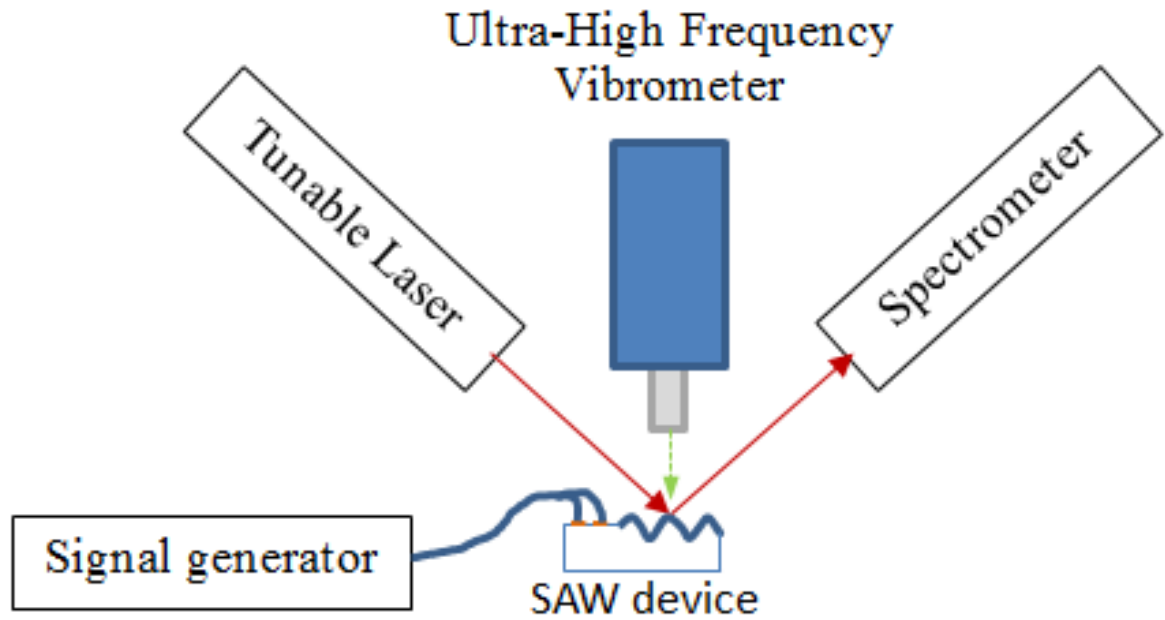


Figure 7.4 Proposed experiment setup for Phonon-Plasmon measurement

A preliminary simulation of this device has been developed to test the scenario for inducing a reliable periodic polarization. This model is based on a similar model in the COMSOL Multiphysics example library [51]. The simulation is done in two-dimensions on the xy plane (z dimension is out of plane) as seen in Figure 7.5. The sample used is PMN-30%PT using the same material properties as given in Table 4.3. Three sets of interdigitized electrodes are on the sample surface, the other area to the right of this is an 88 μm long section where the wave excitation will occur. It is assumed that this device is mounted on another material thus the bottom boundary is a fixed constraint.

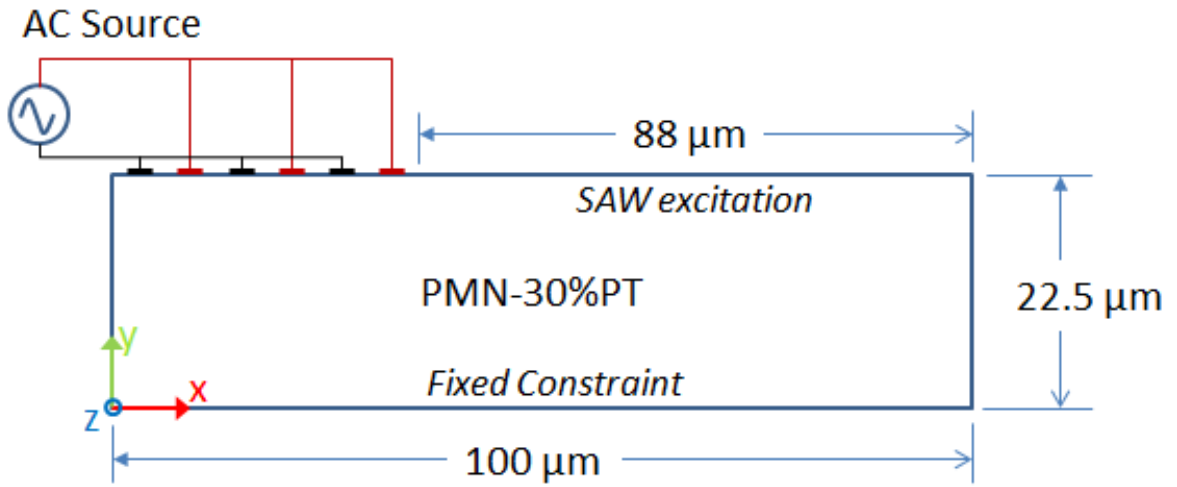


Figure 7.5 Finite Element Analysis setup for 2D SAW model

The device was excited with a 1Volf peak, 786 MHz signal and the results are shown in Figure 7.6. The physical displacement (in black) on the surface is sinusoidal as expected with maximum of about 20 micrometers. The polarization in the y dimension (in blue) is in phase with the displacement with a maximum of about 2 nC/m^2 (or 0.2 pC/cm^2) which is a relatively low level of polarization. The wavelength of the standing wave is approximately 5 μm .

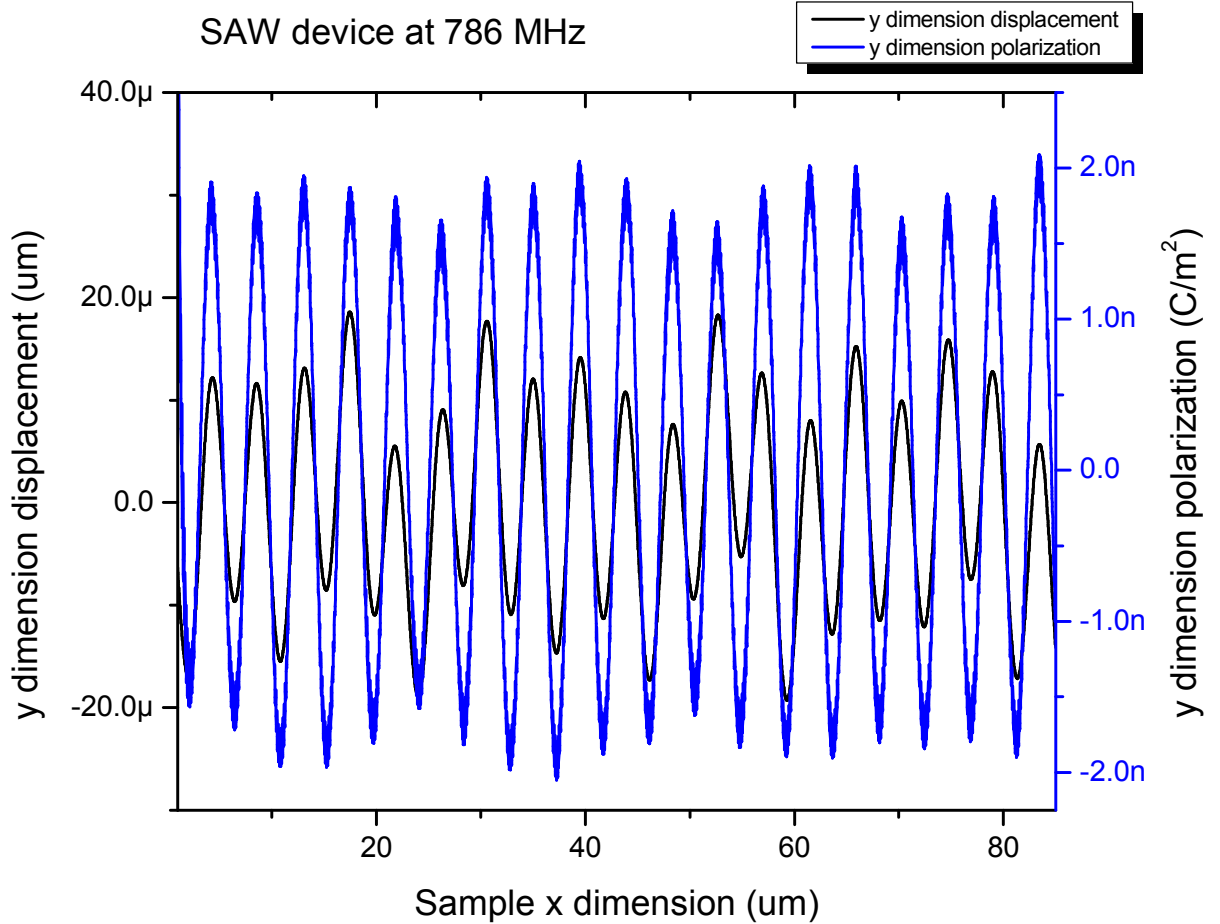


Figure 7.6 Simulation of the y dimension surface displacement and resulting polarization in a SAW device excited at 786 MHz

7.4 Summary

The results in the research involved in this dissertation have opened up many new possibilities for further study, of which a few have been discussed in this chapter. Enhancing the electro-optic interaction at microwave frequencies as discussed in section 7.2 is a very important area of research. Fiber optic communications is a vital area for transferring data which depends on electric modulation to transfer the information. It is this link between electronics and optics that is often the bottle neck in a system, which shows the need for electro-optic modulators that

can modulate at high frequencies. The electro-optic effect decreases significantly in the microwave range which results in lower EO coefficients and thus requiring larger devices that need more power to operate. Energy is one of the biggest issues being studied today and this includes energy efficiency. In this way the enhanced electro-optic effect may be able to make a significant impact on a major issue of our future digital communications.

Section 7.3 also discusses a very import issue as cloaking is a technology directly relatable to national defense. The study of plasmon-phonon coupling will likely play a critical role in greater understanding of resonance enhancement. Using this gained knowledge one is a step closer to acousto-optic metamaterials that offer greater control of the optical transmission necessary for optic (or acoustic) cloaking.

CHAPTER 8: CONCLUSION

This work has explored and integrated many areas of research toward the central goal of enhanced sensitivity for microwave optoelectronic devices. This enhanced sensitivity through piezoresonance coupling has implications for electro-optic modulators and other devices including metamaterial cloaking. The applications for this technology can easily range from commercial telecommunications and consumer electronics, to military defense. Electro-optic, mechanical vibration and admittance experiments have verified the high degree of coupling available as a result of synchronized crystal vibration. The addition of a high frequency vibrometer measurement has shown the ability of induced local field due to piezoelectric polarization in the sample to influence the optical signal propagation even after the crystal begins to become mechanically clamped. FEA models have been constructed and implemented for modeling the crystal vibration, admittance spectrum, linear electro-optic effect, photoelastic effect, and optical wave propagation. These models are consistent with observed experimental results and have provided new insights into the dynamic nature of the induced periodic displacive current in a resonating sample; this gives evidence for the proposed current distribution model proposed in [4]. Advanced time domain simulations have also given verification of the possibility of broad bandwidth enhancement resulting from AC resonance biasing, which was shown experimentally in [6]. Models have verified the influence of periodic ferroelectric domain structure on enhancement in microwave devices. Models have also been used to verify the potential of using piezoresonant enhancement in optical modulators and their advantages over normal and electrically resonant phase modulators of identical size, composition, and configuration.

The ultra-high frequency vibrometer measurements have also yielded interesting results. The longitudinal displacement values have helped to reveal the complex nature of the samples vibration. The high frequency displacement has been shown to decrease as the crystal becomes more constrained while the electro-optic signal remained relatively high. The acceleration of the sample surface gives a similar response showing strong peaks even when the displacement has decreased. This gives an interesting perspective suggesting that the surface acceleration may play a significant role in enhancement and may perhaps lead to an interesting investigation in the future.

In addition to resonant effects the acousto-optic interaction was studied to facilitate a novel solution to more efficient sensors. Optimizing AO devices is more than just the photo elastic relationship and this work has displayed the formation of pertinent material parameters and equations for identifying the maximum interaction directions for materials of any point group symmetry. The maximum interaction directions were shown to not always be along the Cartesian principle axes. These maximum directions typically occur where the acoustic velocity is minimized and the refractive index is maximized (yielding minimum light velocity), the longer the two waves take to co-propagate in the material the more they interact and couple. The Finite Element model of acousto-optic effect and maximum interaction directions found by the Figure of Merit model give consistent conclusions.

Overall this dissertation demonstrates a wide array of methods for enhancement/increased sensitivity in electro-optic devices. Piezoelectric resonance enhancement has implications far beyond the implementation of electro-optic modulators operated at low frequency vibration modes. Synchronization of acoustic phonons with optical photons can open significant potential for low voltage, high sensitivity devices with wide bandwidth operation.

APPENDIX

Appendix McIntosh, R., A. Bhalla, et al. (2010). Dielectric Anisotropy of Ferroelectric Single Crystals in Microwave C-Band by Cavity Vectorial Perturbation Method. Advances in Electroceramic Materials II, John Wiley & Sons, Inc.: 75-88.

A.1 Abstract

Integrating the numerical simulation of electromagnetic field in a perturbed cavity with the microwave measurement via swept frequency technique using a network analyzer, a numerically enhanced cavity vectorial perturbation (NECVP) method is developed and reported in this paper. The NECVP method is capable of resolving anisotropic dielectric properties of various dielectric and ferroelectric single crystals (ϵ_r value in a wide range from 10^0 to 10^3 has been measured). The configuration used in the present study is designed to measure properties in microwave 3-6 GHz (part of the IEEE C-band). Continued signal monitoring and automatic calculation of complex permittivity are made via a LabVIEW interface which aids the data collection process. Numerical simulation of the cavity field is carried out using a finite element analysis software package (COMSOL). The reliability of the deduced dielectric permittivity (and to a lesser extend the dielectric loss) by the NECVP method is found to be quite high limited only by the resolution of the numerical simulation conducted, which becomes more demanding when perturbation of the microwave field is significant. Additionally the directional dependence of dielectric permittivity of a given sample with arbitrary shape can be obtained using a sample rotation technique.

A.2 Introduction

Cavity perturbation method has been widely used to study the dielectric and magnetic parameters in the microwave frequency region. The dispersive and dissipative terms of the

materials are directly related to the change in the resonant frequency and the quality factor of the cavity from the respective empty cavity values [52]. Conventional microwave cavity perturbation techniques have been known as fast and convenient methods for evaluating gigahertz dielectric permittivities of materials that are typically isotropic, of low ϵ_r , and small (compared to the wavelength) in size. However, a cavity perturbation technique that accurately evaluates anisotropic dielectric properties especially of those highly polarizable materials (e.g., ferroelectric materials $\epsilon_r \gg 20$) at GHz frequencies has not been available.

The resonant frequency f_r and the quality factor Q of a rectangular cavity waveguide, for a given standing wave TE_{10N} mode in the microwave region, are expressed by the following equations:

$$f_r = \frac{1}{2\sqrt{\epsilon_0\mu_0}} \sqrt{\left(\frac{1}{a}\right)^2 + \left(\frac{N}{d}\right)^2} \quad (A.1)$$

$$Q = \frac{\eta\pi bd^3}{2R_s(2N^2a^3b + 2bd^3 + N^2a^3d + ad^3)} \quad (A.2)$$

where a , d , ϵ_0 , μ_0 , N , R_s , and η are respectively the width of the waveguide, length of the waveguide, permittivity of free space, permeability of free space, mode number, surface resistance of the cavity, and intrinsic impedance. Inserting a sample into the cavity causes a shift in the resonant frequency f_r and a change in the quality factor Q of the waveguide. This perturbation is dependent on the relative volumes of the cavity V_C and of the sample within the cavity V_S , the permittivity ϵ_r of the sample and thus the electric field concentration in the cavity E_C and in the sample E_S as shown in the general perturbation equation below: [53]

$$2\left(\frac{f_c - f_s}{f_s}\right) - j\left(\frac{1}{Q_s} - \frac{1}{Q_c}\right) = (\epsilon_r - 1) \frac{\int_{V_s} E_c^* E_s dv}{\int_{V_c} |E_c|^2 dv} \quad (A.3)$$

A determination of the complex permittivity by the perturbation technique thus is dependent on both these changes and the integration of the electric field over the volumes of the sample within the cavity. For a sample with length parallel to the electric field direction, assuming a small perturbation of the field, the above relation can be easily simplified and used to find the complex permittivity [54]. Under these conditions the electric fields in the sample (E_s) and in the cavity (E_c) are approximately equal; one can then derive the following expressions for the real and the imaginary parts of the complex permittivity:

$$\epsilon_r' = \frac{f_c - f_s}{f_s} \frac{V_c}{2V_s} + 1 \quad (\text{A.4})$$

$$\epsilon_r'' = \frac{V_c}{4V_s} \left(\frac{1}{Q_s} - \frac{1}{Q_c} \right) \quad (\text{A.5})$$

Compared with the Hakki-Coleman post resonant method which requires typically centimeter diameter samples, [55] the cavity perturbation technique offers flexibility that permits measurement of mm size samples of essentially any shape.

Considerable errors however, using the conventional microwave perturbation method by Equations (A.4) and (A.5), may result in the values of complex dielectric permittivity when the assumption of small perturbation is invalid. Santra and Limaye [56] described an approach using finite element method to assist in evaluating complex permittivity of arbitrary shape and size and demonstrated the application of such method to measure isotropic dielectric materials with moderate permittivity ($\epsilon' \sim 22$). In the current study the integration of numerical finite element

analysis with microwave measurement is extended to account for directional dependence of samples and to ferroelectric materials with ϵ_r' up to 10^3 .

A.3 Experimental

A rectangular waveguide was used for all experiments reported in this paper. The dimensions (in centimeters) are $b=4.74$ in width, $a=2.21$ in height, and $d=18.2$ in length. All samples were measured at modes TE_{103} and TE_{105} with cavity resonant frequencies of 4.01GHz and 5.19 GHz at room temperature, respectively. Using this method samples are placed in the geometric center of the waveguide where the electric field strength is maximum for the odd modes. The waveguide also has custom holes in four of its faces to allow insertion of the sample and a hollow metal tube welded to each of the holes to prevent energy loss (See Figure A.1).

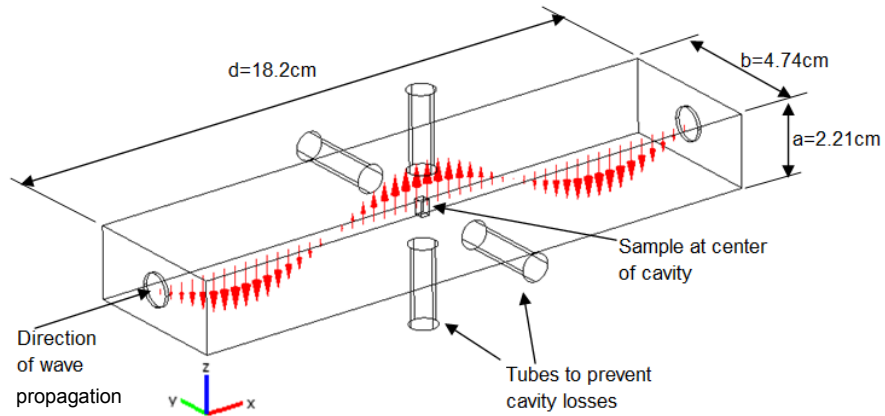


Figure A.1 Configuration and dimension of the microwave cavity used for the NECVP study

For a typical rectangular sample there are four orientations of interest illustrated in Figure A.2(a) through Figure A.2 (d), hereafter referred to as positions PE, PF, HE, and HF, where P and H designate whether length direction of the sample is parallel (P) or horizontal (H) to the electric field, E and F designate whether the sample's edge (E) or face (F) is inline with the

direction of propagating EM wave. The designations are as follows: (a) Position PE: Length parallel to E field, Edge inline with wave propagation, (b) Position PF: Length parallel to E field, Face inline to wave propagation, (c) Position HE: length horizontal to E-field, Edge inline with wave propagation, (d) Position HF: Length horizontal to E-field, Face in line with wave propagation. Additionally using this method a sample oriented with its longest axis perpendicular to the electric field (as in Positions HE & HF) can be rotated to investigate the permittivity at different angles.

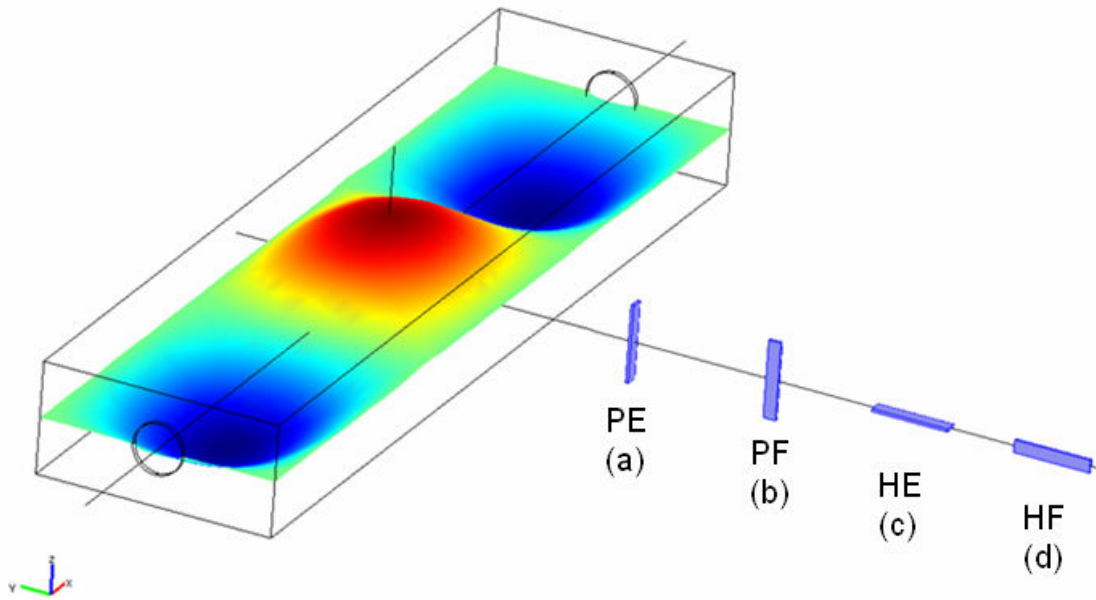


Figure A.2 Orientation of samples relative to microwave resonant cavity

Both low permittivity and high permittivity samples were studied in the work, some were chosen for their well known dielectric properties at microwave frequency, some were studied to demonstrate the capability of the method. The types of the samples and their dimensions are summarized in Table A.1.

Table A.1 Summary of sample dimensions used in microwave measurement

Sample	Shape	Dimensions (mm)
Alumina Ceramic Substrate (99.6% Al_2O_3)	Bar	$L=0.63$, $W=2.64$, $H=16.25$
Corning 0080 glass	Bar	$L=1.19$, $W=1.21$, $H=10.26$
Fused Silica	Tube	$D_{\text{out}}=7.97$, $D_{\text{in}}=5.96$, $L=206$
Pyrex Glass	Rod	$D=3.92$, $L=125$
Teflon (PTFE)	Rod	$D=4.8$, $L=50$
PMN-PT single crystal, Bridgman method	Bar	$L=2.7$, $W=2.96$, $H=4.69/[110]$
PZT-5 ceramic, commercial	Rod	$D=3.36$, $L=3.74$

A multiphysics software package (COMSOL) was used for the finite element simulation of the waveguide and the samples. All simulations were done for the TE_{103} and TE_{105} modes. The conductivity of the walls of waveguide was given in accordance with that of copper and the four round ports were included in the modeling. In this report all the samples were modeled using their actual physical dimensions but considered as having isotropic permittivity (anisotropic modeling will be the content of an upcoming report). A plot of the perturbed cavity electric field (V/m) with inserted sample of assumed dielectric permittivity $\epsilon_r=10$ is shown in Figure A.3. The sample has dimensions $2.7 \times 2.96 \times 4.69 \text{ mm}^3$ and is positioned in the center of the waveguide in PE position.

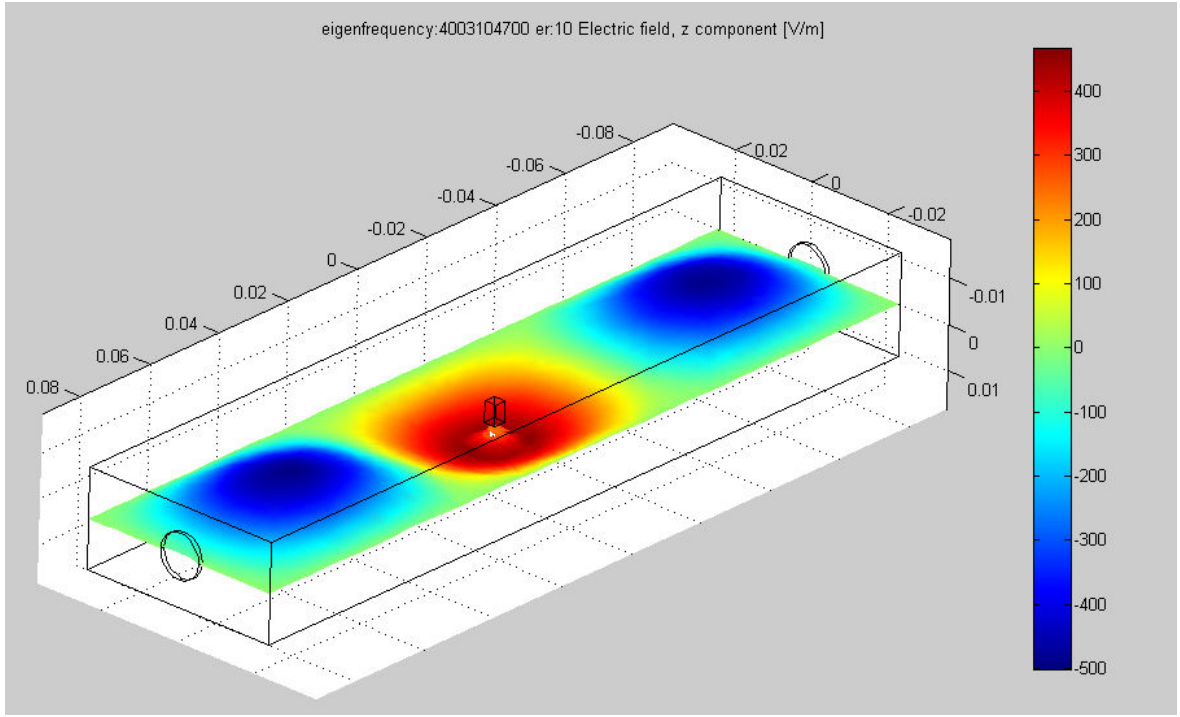


Figure A.3 Finite element simulation of the perturbed cavity electric field (V/m), for TE₁₀₃ mode near $f_c=4.003\text{GHz}$

By placing a sample in the center of the waveguide where $|E_C|$ is at the maximum and by assigning permittivity of the sample as a variable, a parametric sweep was performed to calculate the f_s as one of the outputs of the finite element analysis. For a given sample and sample dimension the normalized resonance frequency shift $(f_c-f_s)/f_s$ can be matched to the experimental shift and thus to determine the real permittivity. Once the real permittivity is known then the imaginary part is resolved by an additional parametric sweep to match the normalized change in Q , in form of $(1/Q_s)-(1/Q_c)$. For the given waveguide the computation time is less than an hour using a HP workstation (HP Z80 22 GB RAM), depending on the spatial resolution desired.

A.4 Results and Discussion

A.4.1 Limitations of the Conventional Perturbation Method

Figure A.4 shows a plot of normalized frequency shift vs. real part of the relative permittivity for a sample of rectangular shape in PE position. The length of the sample is such that its ends touch both sides of the walls of the cavity. The plot is presented to compare the results of ϵ_r' by FEA simulation and by the calculation from the conventional perturbation equations (Equations (A.4) and (A.5)). The two methods are in reasonable agreement for low shifts; however they start to diverge when the normalized resonance frequency shift $(f_c - f_s)/f_s > 0.11$ where their discrepancy becomes $>20\%$ and the conventional evaluation becomes invalid as ϵ_r' approaches 100.

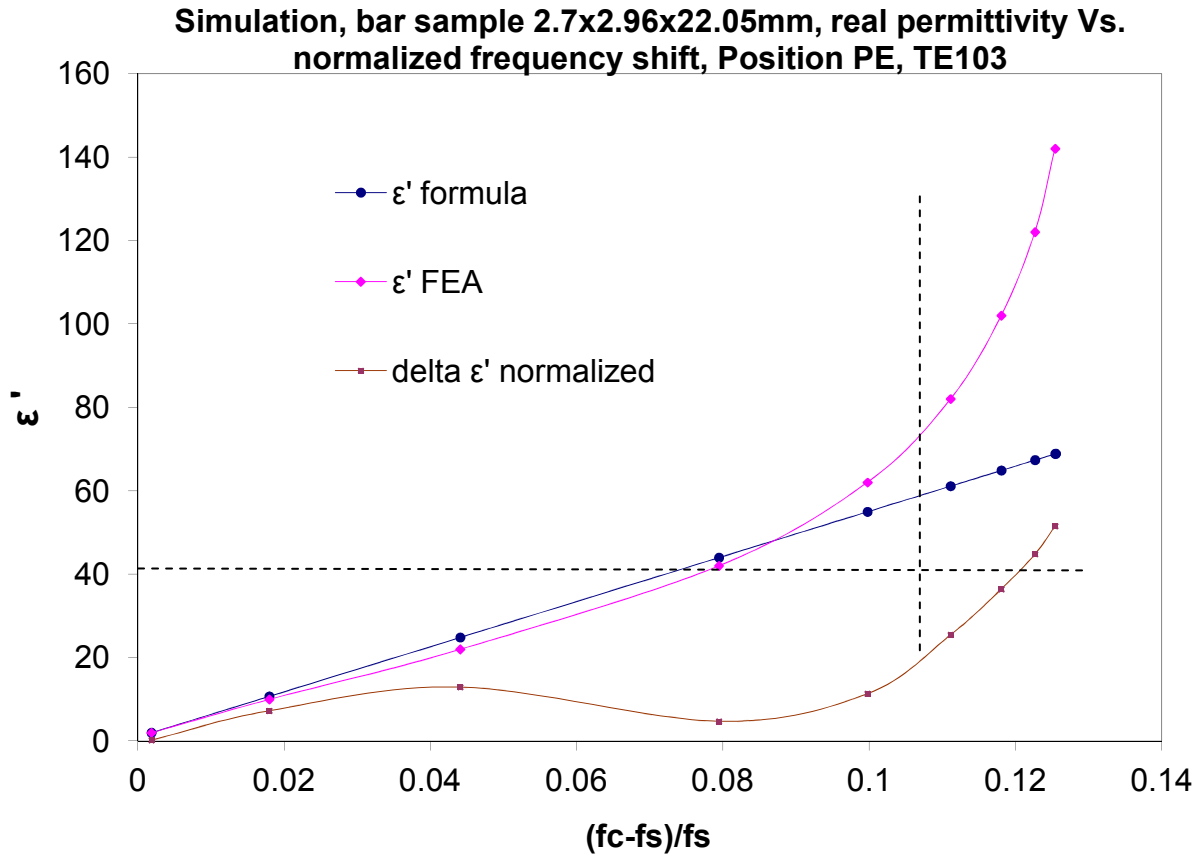


Figure A.4 Comparison of calculated resonance frequency shift as function of dielectric permittivity, by FEA and by Equations (4) and (5)

Another comparison using a shorter sample ($L=4.69\text{mm}$) is shown in Figure A.5. The percent difference becomes greater than 20% when the real part of the permittivity is above 4. The comparison demonstrates the limitations of the simplified conventional perturbation formula used for samples shorter than the height of the cavity. The conventional method in such a case underestimates the permittivity of a sample and is essentially invalid for $\epsilon_r' > 10$. The reason for these large errors at higher permittivity becomes clear when we observe the electric field profile upon increasing permittivities of the sample inside the cavity (

Figure A.6). For permittivity of 1 the cavity field is well defined and is sinusoidal; however as the permittivity increases the perturbation to the electric field intensifies. Furthermore as the permittivity increases the electric field will start to bend around the sample and will have less

effect on the frequency shift causing a decrease in measurement sensitivity. To increase the sensitivity for samples of high permittivity, longer sample dimension (// to the electric field direction) and/or higher signal level should be considered.

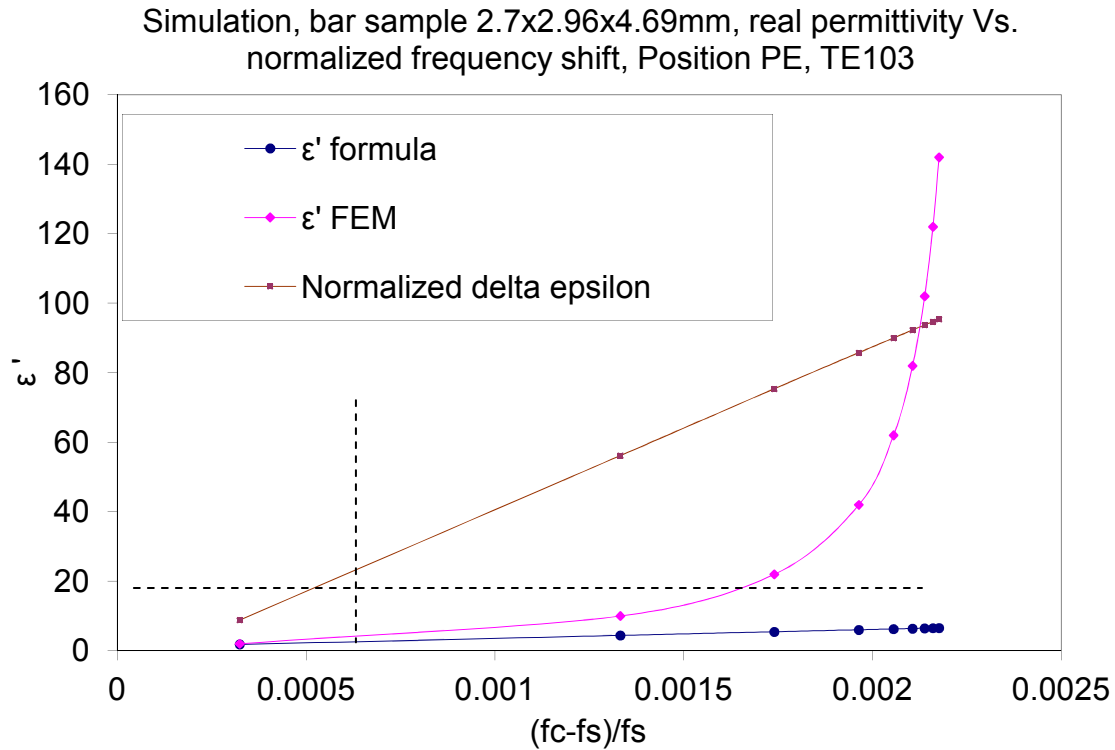


Figure A.5 Comparison of calculated resonance frequency shift as a function of dielectric permittivity, by FEA and by Equ. (9.4) and (9.5). The bar-shaped sample (2.7x2.96x4.69 mm³) is PE positioned and with dimension shorter than the height of the cavity

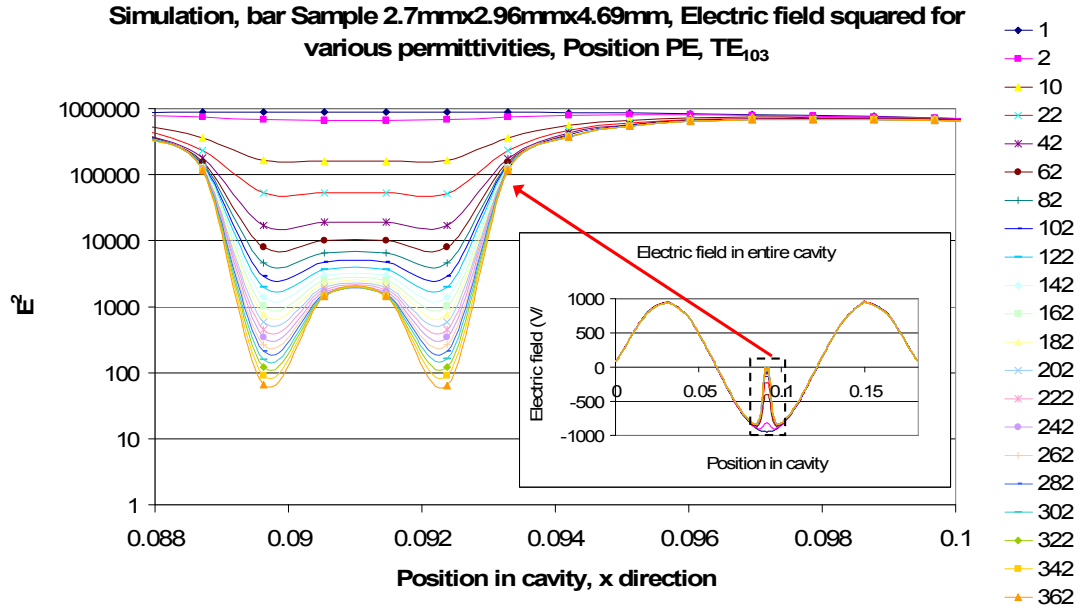


Figure A.6 Perturbed electric field intensity profile in the microwave cavity of TE_{103} mode as a function of the real part of the permittivity for a PE center positioned sample ($2.7 \times 2.96 \times 4.69 \text{ mm}^3$)

In general, there are several methods [53] for calculating the electric field concentration in the sample; These methods are useful but only for certain sample types and orientations. The electric field concentration in a cylindrical sample where the ends terminate at the waveguide walls is fairly easy to determine however the problem becomes far more difficult for a sample that does not terminate at the waveguide walls. Furthermore it becomes difficult to measure high permittivity dielectrics in the microwave region due to the skin effect. The electric field becomes less concentrated in the sample and thus sensitivity decreases.

A.4.2 Verification of NECVP Using Low Permittivity Materials

Table A.2 summarizes the complex permittivity (expressed in terms of ϵ_r' , ϵ_r'' , and $\tan\delta$) obtained using the procedure described earlier (the NECVP method) for alumina ceramic sample of thin rectangular shape, measured in all four standard positions. The table shows that the real

permittivity of the sample is about 8.4 at ~4GHz which is in close agreement of reported values (about 9 at 1MHz) [57]. The signal levels for positions HE and HF were too low to measure which is sometimes a problem for low loss materials with length dimension positioned perpendicular to the electric field. The imaginary permittivity is about 5×10^{-3} and the $\tan \delta$ loss factor is 6×10^{-4} for positions PE and PF at ~4GHz. The reported [57] values are $\epsilon_r'' = 0.003-0.02$ and $\tan \delta = 0.0003-0.002$ (at 1MHz).

Table A.2 Alumina complex permittivity measured by NECVP method near 4.01GHz (TE₁₀₃) and 5.19 (TE₁₀₅) GHz

Alumina Ceramic Substrate (99.6% Al ₂ O ₃) - Bar							
Position	Mode	ϵ_r'	+/-	ϵ_r''	+/-	$\tan \delta$	+/-
PE	TE ₁₀₃	8.452	0.009	0.005	0.007	0.0006	0.0008
	TE ₁₀₅	8.382	0.008	0.015	0.016	0.0018	0.0019
PF	TE ₁₀₃	8.452	0.009	0.005	0.007	0.0006	0.0008
	TE ₁₀₅	8.359	0.015	0.007	0.0086	0.0008	0.0010
HE	TE ₁₀₃	8.376	0.046	-	-	-	-
	TE ₁₀₅	7.900	0.281	-	-	-	-
HF	TE ₁₀₃	7.736	0.047	-	-	-	-
	TE ₁₀₅	7.521	0.105	-	-	-	-

Table A.3 summarizes the complex permittivity obtained using NECVP method for a rectangular sample of Corning 0080 glass. The same material of larger disk shape was also tested with the post resonant technique (See Table A.4) and the results using both methods agree reasonably well.

Table A.5 shows the results obtained using NECVP method for a fused silica in tubular form. The complex permittivity for bulk fused silica at 5 GHz was reported [58] to be ~3.8 and the $\tan \delta$ of the value between 0.2 to 0.4×10^{-4} . The results obtained show somewhat higher real part of the permittivity and also higher $\tan \delta$; however in the same time both PE and HE positions yield consistent results. Thus the results are likely to be reliable taking into consideration that

surface treatment is often applied onto fused-silica tubing to decrease surface activity or inhibit UV absorption, which may account to an increase in the dielectric loss.

Table A.3 Corning 0080 glass complex permittivity measured by NECVP method near 4.01GHz (TE₁₀₃) and 5.19 (TE₁₀₅) GHz

Corning 0080 - Bar							
Position	Mode	ϵ_r'	+/-	ϵ_r''	+/-	$\tan \delta$	+/-
PE	TE ₁₀₃	6.151	0.012	0.088	0.010	0.0143	0.0016
	TE ₁₀₅	6.103	0.012	0.093	0.039	0.0153	0.0064
PF	TE ₁₀₃	6.170	0.014	0.063	-	0.0101	-
	TE ₁₀₅	6.100	0.030	0.051	0.0425	0.0084	0.0121
HE	TE ₁₀₃	5.923	0.021	0.125	-	0.0211	-
	TE ₁₀₅	5.780	0.054	0.098	0.152	0.0169	0.0216
HF	TE ₁₀₃	5.390	0.020	0.125	-	0.0232	-
	TE ₁₀₅	5.288	0.054	0.125	-	0.0236	-

Table A.4 Corning 0080 glass complex permittivity measured by post resonant technique

	ϵ_r'	ϵ_r''	$\tan \delta$
3 GHz	6.715	0.1477	0.0220
6 GHz	6.750	0.1256	0.0186

Table A.5 Fused silica tube complex permittivity measured by NECVP method near 4.01GHz (TE₁₀₃) and 5.19 (TE₁₀₅) GHz

Fused Silica - Tube							
Position	Mode	ϵ_r'	+/-	ϵ_r''	+/-	$\tan \delta$	+/-
PE	TE ₁₀₃	4.248	0.001	0.0332	0.0003	0.0078	0.0001
	TE ₁₀₅	4.213	0.001	0.0319	0.0010	0.0076	0.0002
HE	TE ₁₀₃	4.244	0.001	0.0327	0.0005	0.0077	0.0001
	TE ₁₀₅	4.197	0.004	0.0314	0.0024	0.0075	0.0006

Table A.6 and Table A.7 summarize the results for a Pyrex glass rod and a Teflon rod. For the Corning Pyrex 7740 glass, the measurement results are consistent with the reported dielectric constant ($\epsilon_r=4.6$) and loss tangent ($\tan\delta= 0.004$) at 20 °C and 1 MHz, respectively [59]. For PTFE Teflon rod the real part of dielectric permittivity measured at room temperature

compares well with those previously reported ($\epsilon_r' = 2.055$ at 300K and 9.93 GHz) [60]. Although the NECVP technique is highly sensitive, no further interpretation on the physical meanings of the differences on measured results between the PE and the HE positions for the presumably isotropic Pyrex and the Teflon rods can be given without rigorous calibration of the 3D field distribution of the cavity, other than noting here that certain uncertainties exist caused by reasons in addition to dimensional variations.

Table A.6 Complex permittivity of Pyrex glass rod measured by NECVP method near 4.01GHz (TE₁₀₃) and 5.19 (TE₁₀₅) GHz

Glass - Rod							
Position	Mode	ϵ_r'	+/-	ϵ_r''	+/-	$\tan \delta$	+/-
PE	TE ₁₀₃	3.9561	0.0006	0.0294	0.0010	0.0074	0.0002
	TE ₁₀₅	3.9248	0.0012	0.0271	0.0019	0.0069	0.0004
HE	TE ₁₀₃	4.6386	0.0022	0.0291	0.0028	0.0062	0.0006
	TE ₁₀₅	4.5704	0.0108	0.0291	0.0028	0.0063	0.0006

Table A.7 Permittivity of Teflon rod measured by NECVP method near 4.01GHz (TE₁₀₃) and 5.19 (TE₁₀₅) GHz

Teflon (PTFE) - Rod			
Position	Mode	ϵ_r'	+/-
HE	TE ₁₀₃	2.0557	0.0002
	TE ₁₀₅	2.0465	0.0019
PE	TE ₁₀₃	1.8876	0.0001
	TE ₁₀₅	1.8788	0.0006

A.4.3 Anisotropic Dielectric Property Evaluation

One of the challenges of the NECVP method is orienting the sample in the cavity in a reproducible manner. A jig was constructed to allow simple manipulation of the sample. Two pieces of string were strung through the middle axis of the waveguide (perpendicular to E field) and secured on either side (See Figure A.7 and Figure A.8). The sample under test is pinched between the two strings. When the strings are given tension the sample is secure and by

simultaneously rotating the top and bottom ends of the string the sample is rotated inside the waveguide. This setup ensures that the sample stays centered and the string has only a very small effect on the perturbation. The empty cavity gives a resonant frequency of 3.9877519 GHz \pm 880Hz while the two pieces of thread give 3.9877002 GHz \pm 510 Hz. This gives a normalized shift of only 0.0000129 \pm 0.0000003 and is fairly negligible compared to typical shifts for samples which are at least an order of magnitude higher (0.0001).

A rectangular bar shaped sample of alumina (isotropic dielectric properties) was placed in the waveguide in position HE and rotated about its long axis such that at 0 degrees it is at position HE and at 90 degrees at position HF. The sample was rotated counter clockwise in 15 degree intervals. Figure A.9 shows the results of this test of normalized frequency shift verse rotation. The top view of the cross section of the sample is illustrated for rotation angles at 0, 45, and 90° positions.

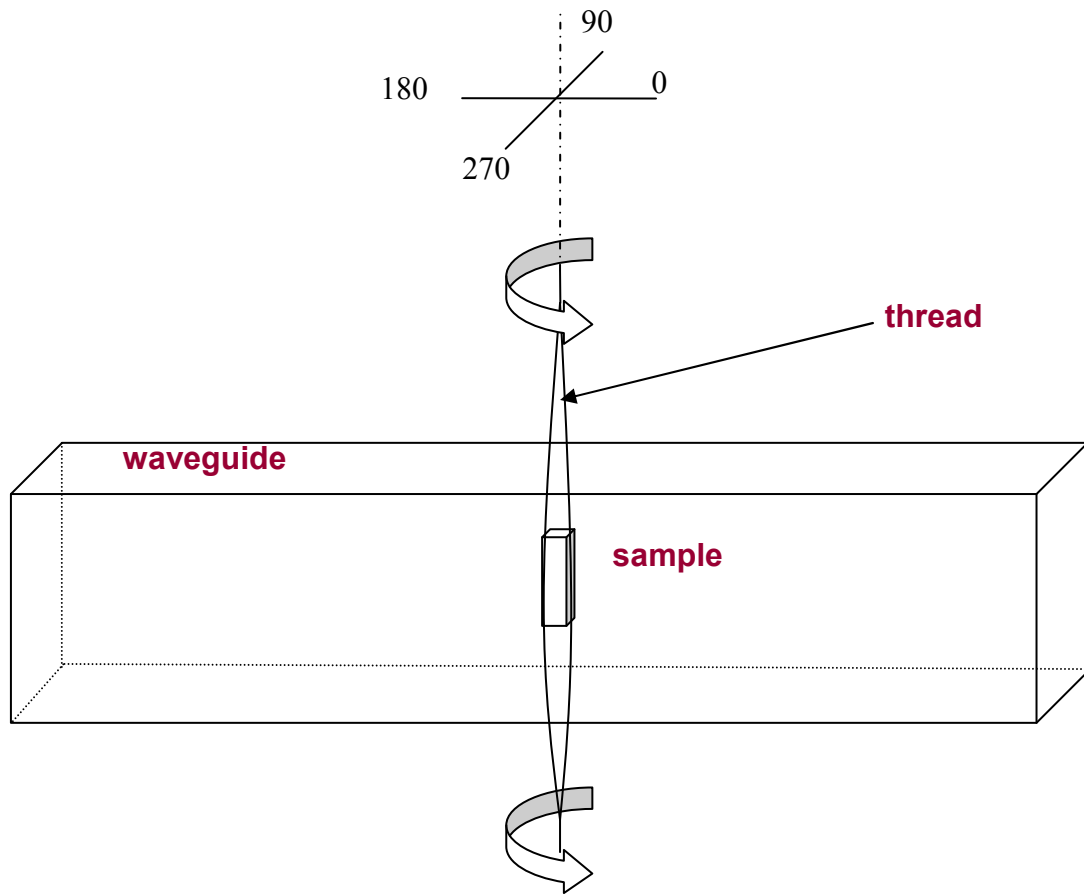


Figure A.7 Schematics of the rotation fixture

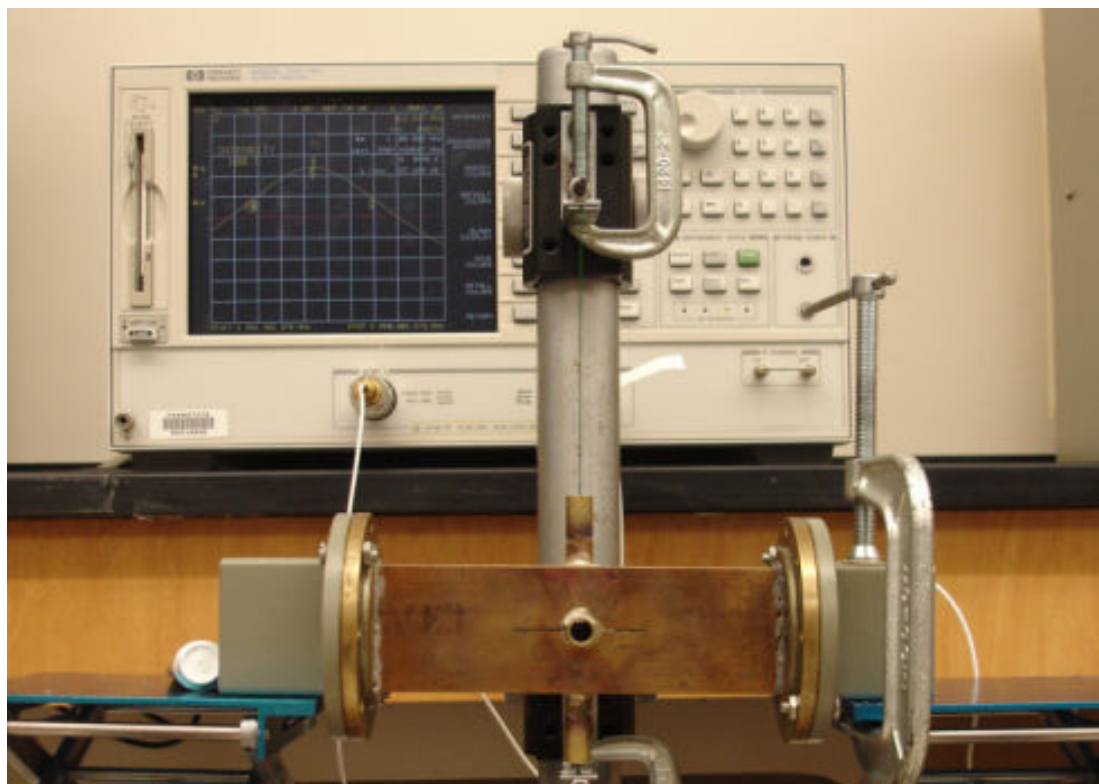


Figure A.8 Actual configuration of the cavity perturbation setup with sample rotation

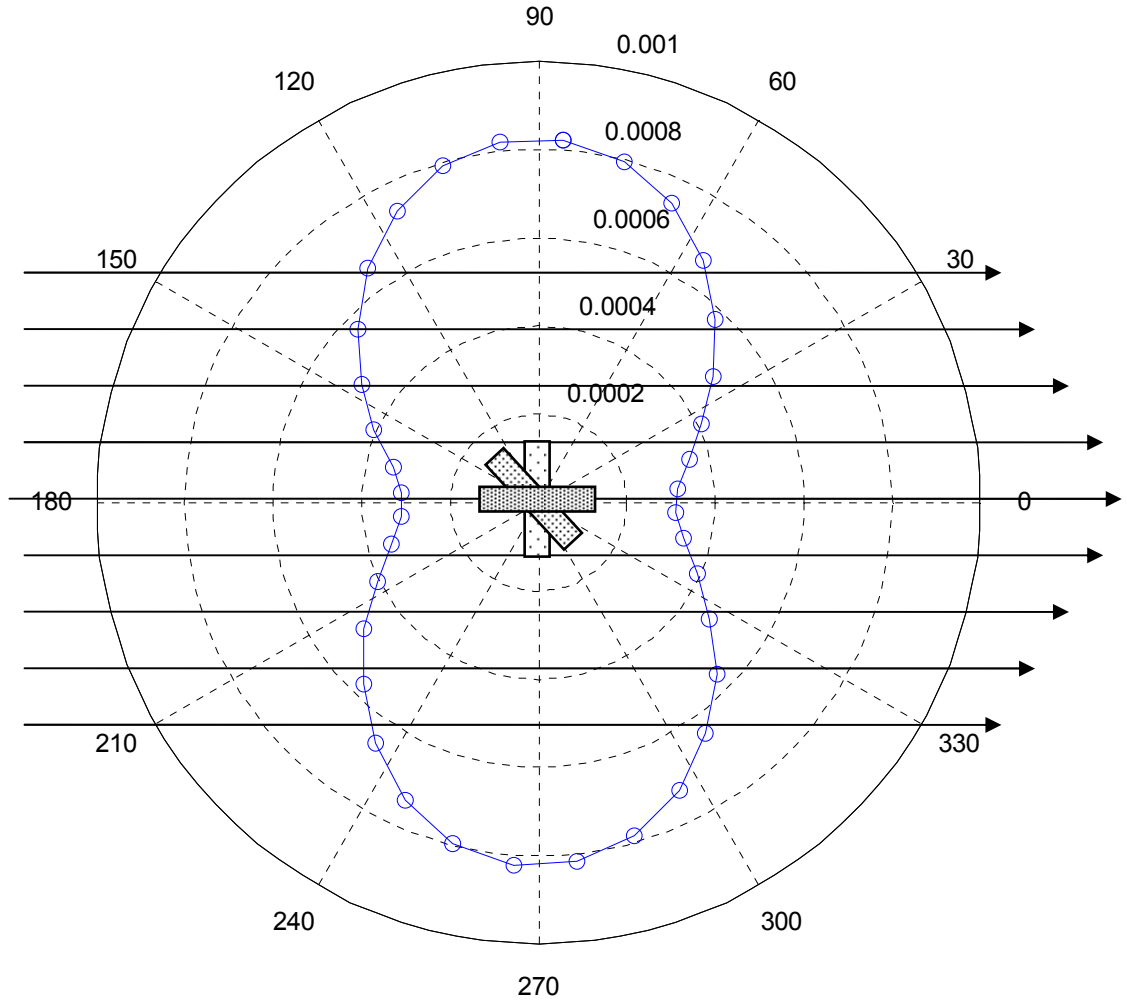


Figure A.9 Resonance frequency shift $(f_c - f_s)/f_s$ as function of rotation angle for a rectangular shaped alumina ceramic sample. Arrows indicate electric field directions

Ideally the above experiment can be used as a means of calibration for the NECVP method to account for any additional disturbances due to the insertion of rotation mechanisms, the existence of surface imperfection of the given cavity, as well as the openings present on the cavity. In the current report however the simulation was performed over a range of permittivities at each rotation angle taking into consideration of sample dimension variations only, thus is not regarded as a full calibration. Figure A.10 shows the derived permittivity ϵ_r' of the rotated

alumina sample, corrected for dimensional difference, that varies from 8.71 to 9.44, adjusted based on the standard deviation of the measured values.

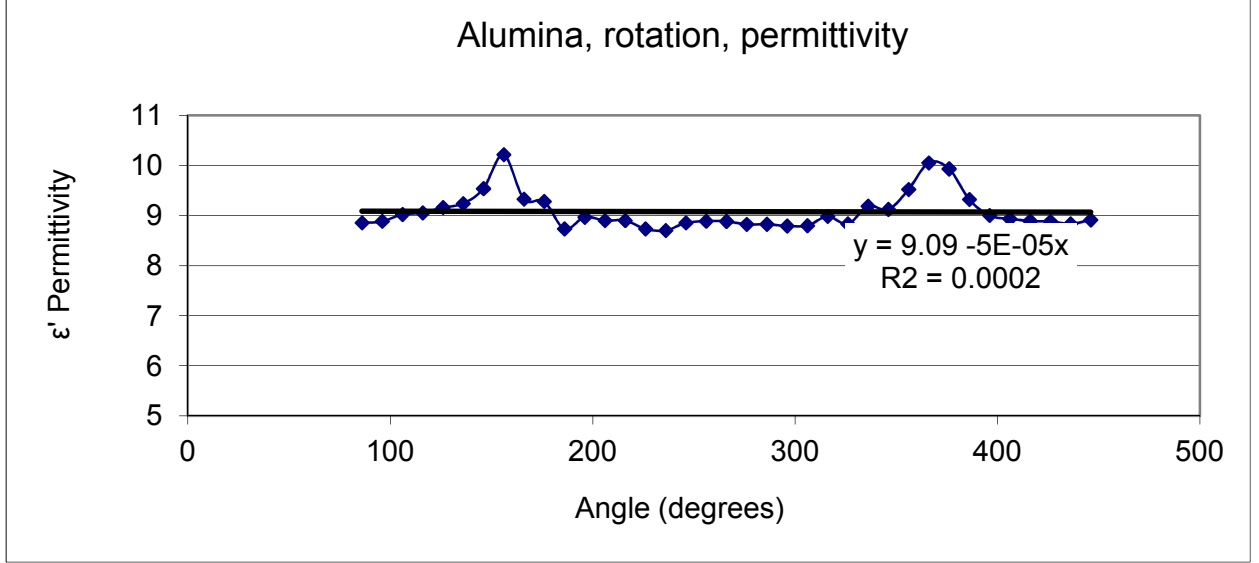


Figure A.10 Derived permittivity as a function of rotation angle for a rectangular shaped alumina ceramic bar, after correction of the dimensional variation

A.4.4 NECVP Method for High Permittivity Ferroelectric Materials

Microwave electric field strength inside a sample is inversely proportional to the dielectric permittivity of the sample thus as permittivity increases the signal level and the sensitivity of the measurement decrease. Shown in Figure A.11 is a simulation of a ferroelectric relaxor $(1-x)\text{Pb}(\text{Mg}_{1/3}\text{Nb}_{2/3})\text{O}_3-x\text{PbTiO}_3$ (PMN- x PT, $x=0.30$) sample over a range of resonance frequency shift $(f_c-f_s)/f_s$. The experimental results obtained gave a normalized frequency shift of 0.00222 that corresponds to a derived permittivity $\epsilon_r'_{//[110]} \sim 250$. The sample was pre-poled along the $[110]$ direction. In comparison, $\epsilon_r'_{//[001]}$ in the range of 400 on a PMN-PT crystal by a transmission line method at 10 GHz was reported [61].

Figure A.12 shows results for a PZT-5H sample for which experimental results gave 0.00149 for the frequency shift and resulting permittivity of about 300. The permittivity of PZT

in the microwave region has been reported with values between 300 and 700 depending on the composition [62].

A.4.5 Effect of Meshing on NECVP Measurement Results

Size and level of meshing during FEA process can often be a significant factor impacting resolution and thus accuracy of results from a simulation. The finite element analysis method is used as a probing tool to depict the actual three-dimensional EM field distribution in a cavity and the sample within. The quality of this estimation is a direct result of a proper meshing. Typical mesh used in this paper gave 100,000 degrees of freedom which is sufficient for most of the low permittivity samples. However due to the lower sensitivity and steep change in field distribution for samples of high permittivity it can often be necessary to have up to 500,000 degrees of freedom. Figure A.13 illustrates the importance of meshing on results where we see a different converging curve for each meshing freedom. In COMSOL free meshing parameters are designated 1 through 9 where 1 is the finest mesh. Mesh 9 has about 2,000 degrees of freedom and mesh 1 about 500,000 degrees of freedom. Time per solution for mesh 9 is only 3.5 seconds but 20 minutes are typically needed for mesh 1. The necessary meshing size can be determined by refining until further refinement yields little change in the curve, i.e., achieved a prescribed accuracy. More effective meshing can also be achieved by using advanced or adaptive meshing strategy to have fine mesh in sub-domain containing the sample, to reach a balance between high resolution and low calculation power consumption.

PMN-PT, Normalized frequency shift Vs. real permittivity, Position PE, TE₁₀₃

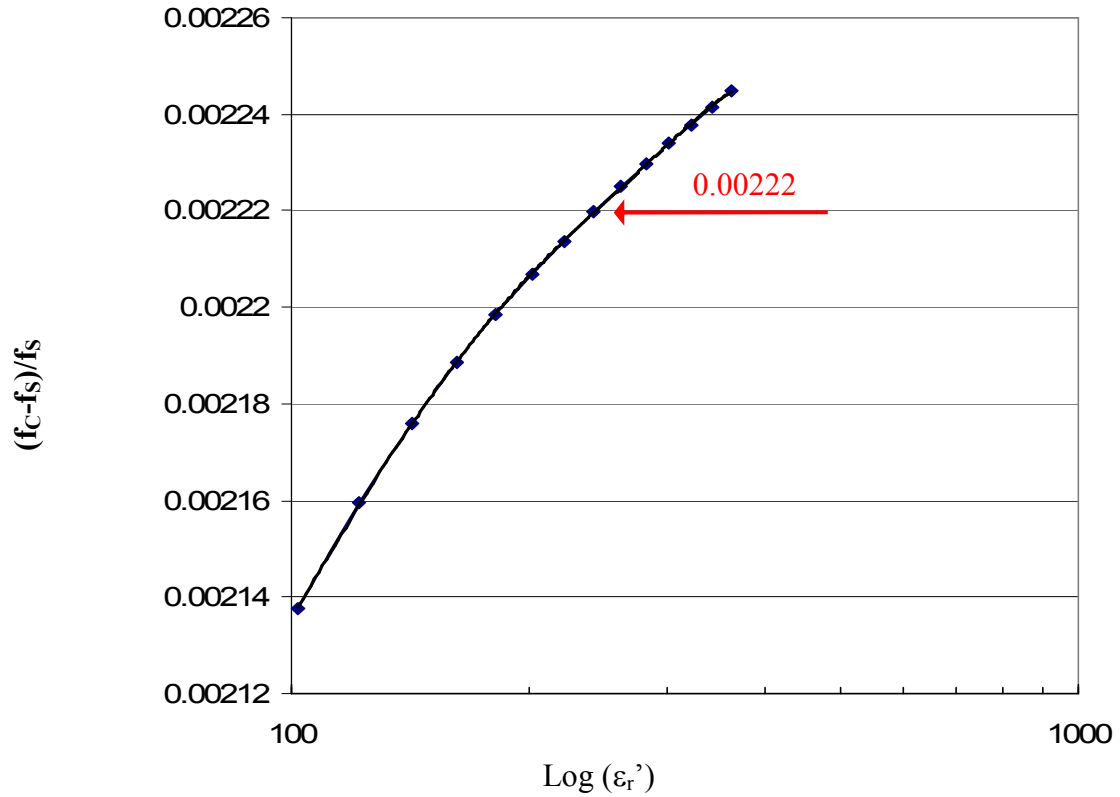


Figure A.11 Simulation result on the normalized shift of resonance frequency as function of $\log \epsilon_r'$. The relative permittivity of the prepoled PMN-30PT crystal in [110] direction was derived by comparing the measured value with the simulated frequency shift, using the NECVP method

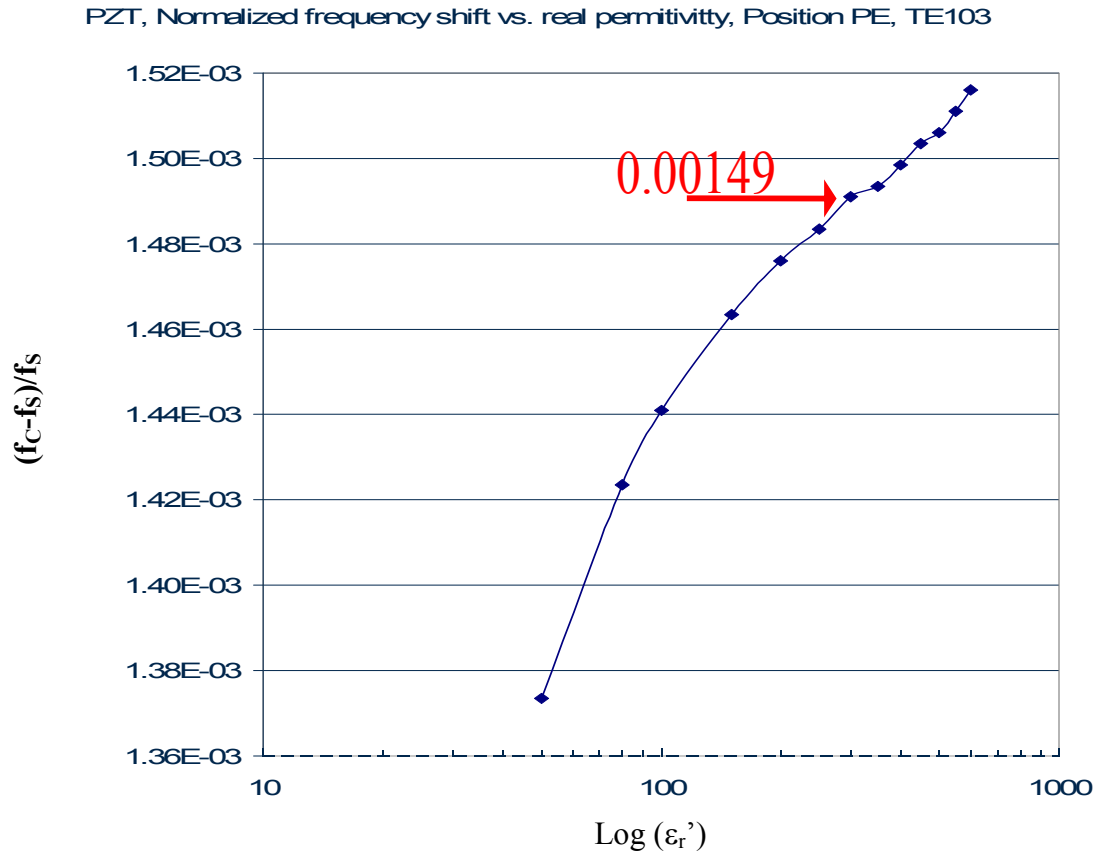


Figure A.12 Simulation result on the normalized shift of resonance frequency as function of $\log \epsilon_r'$. The relative permittivity of the PZT-5H ceramic was derived by comparing the measured value with the simulated frequency shift, using the NECVP method

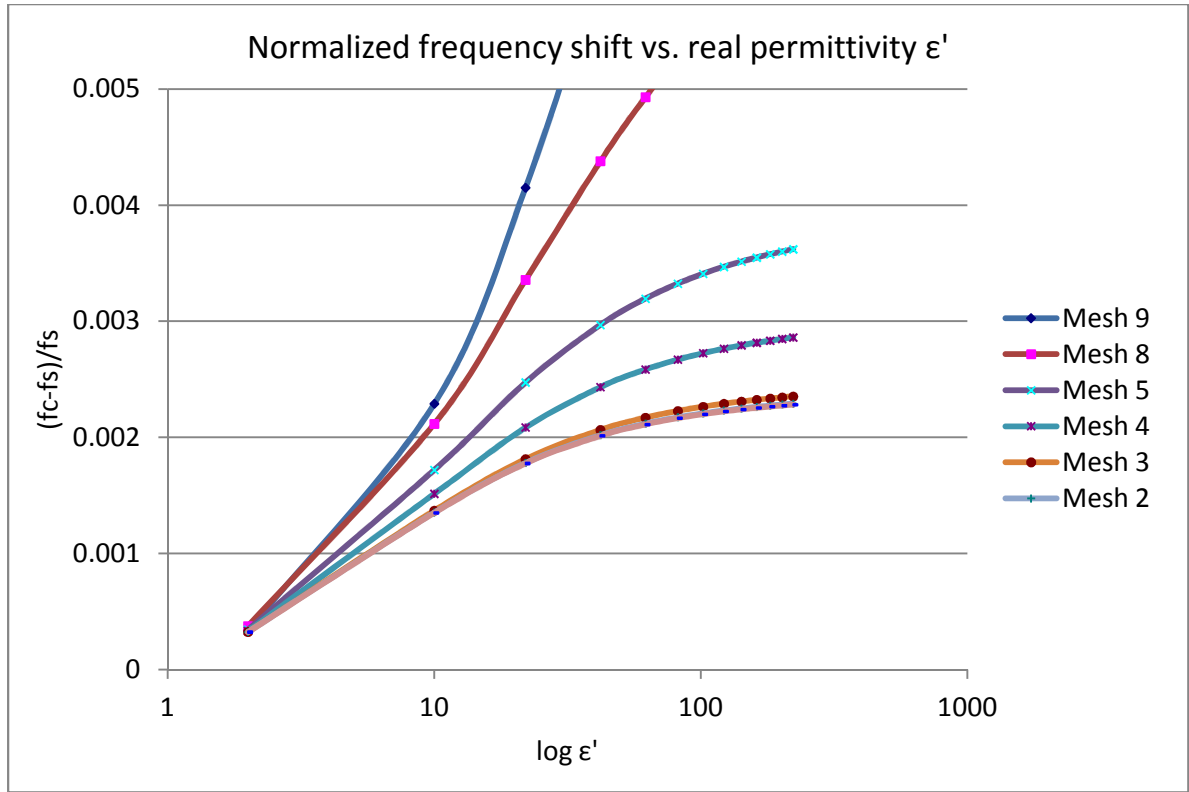


Figure A.13 Effect of Meshing, Mesh 1 being the finest

A.5 Summary

A numerically enhanced cavity vectorial perturbation (NECVP) microwave dielectric measurement method has been proposed, investigated, and demonstrated. In contrast to the conventional microwave cavity perturbation method that deals with the shift of cavity resonance frequency under the assumption of invariant cavity EM field, this study shows that three-dimensional EM field distribution resolved by using a finite element analysis method (e.g., COMSOL), is essential for an accurate evaluation of dielectric materials that are highly polarizable, anisotropic, and of arbitrary shape. This paper reports measurement results of microwave dielectric permittivity by NECVP method of a wide range of dielectric and ferroelectric materials including alumina, glass, fused silica, Teflon, PMN-PT crystal and PZT

ceramic samples. Microwave C-band dielectric permittivity ranging from 2 (for Teflon) to 300 for PZT ceramic are reported. This method is shown to have high resolution for the real part of dielectric permittivity ϵ' and good sensitivity to the imaginary permittivity ϵ'' . For the samples tested the results obtained compare well with existing dielectric properties reported using conventional microwave measurement techniques, without the restraints on specific form, shape and volume of a given sample. Preliminary results were also reported on the evaluation of anisotropic dielectric properties by sample rotation within the cavity. Optimization of desired resolution and reduced calculation time may be achieved by adaptive meshing during the finite element analysis process. The frequency range of the reported NECVP method can be extended and additional measurement parameters such as temperature and bias may be included in the future.

REFERENCES

- [1] R. Guo, H. Liu, G. Reyes, W. Jamieson, and A. Bhalla, "Piezoelectric resonance enhanced electrooptic transmission in PZN-8PT single crystal," 2008, p. 705616.
- [2] E. L. Wooten, K. M. Kissa, A. Yi-Yan, E. J. Murphy, D. A. Lafaw, P. F. Hallemeier, D. Maack, D. V. Attanasio, D. J. Fritz, G. J. McBrien, and D. E. Bossi, "A review of lithium niobate modulators for fiber-optic communications systems," *Selected Topics in Quantum Electronics, IEEE Journal of*, vol. 6, pp. 69-82, 2000.
- [3] A. Garzarella, S. B. Qadri, T. J. Wieting, and D. H. Wu, "Piezo-induced sensitivity enhancements in electro-optic field sensors," *Journal of Applied Physics*, vol. 98, p. 043113, 2005.
- [4] S. Johnson, K. Reichard, and R. Guo, "Dynamic linear electrooptic property influenced by piezoelectric resonance in PMN-PT crystals," in *106th Annual Meeting of the American Ceramic Society, April 18, 2004 - April 21, 2004*, Indianapolis, IN, United states, 2005, pp. 277-287.
- [5] Y. Pisarevski and G. Tregubov, "The Electro-Optical Properties of $\text{NH}_4\text{H}_2\text{PO}_4$, KH_2PO_4 , and $\text{NC}(\text{CH}_2)_6$ Crystals in UHF Fields," *Soviet Physics-Solid State*, vol. 7, 1965.
- [6] S. T. Johnson, "Dynamic Linear Electro-Optic Frequency Dependence in PMN-32%PT and PZN-8%PT for RF Microwave Photonics," The Pennsylvania State University, 2005.
- [7] A. Garzarella, S. B. Qadri, T. J. Wieting, W. Dong Ho, and R. J. Hinton, "Dielectrically induced sensitivity enhancements in electro-optic field sensors," *Optics Letters*, vol. 32, pp. 964-6, 2007.
- [8] N. A. P. A. L. Kholkin, A. V. Goltsev, "Piezoelectricity and crystal symmetry," in *Piezoelectric and Acoustic Materials for Transducer Applications*, A. E. K. Safari Ahmad, Ed., ed: Springer, 2008, pp. 17-38.
- [9] M. J. Weber, *Handbook of Optical Materials, Crystalline Materials*: CRC Press, 2002.
- [10] Comsol. (2012). Available: <http://www.comsol.com/>
- [11] A. Yariv and P. Yeh, *Optical waves in crystals : propagation and control of laser radiation*. New Jersey: Wiley, 2003.
- [12] A. Rogers, *Essentials of Optoelectronics With Applications* vol. 4. New York: Chapman & Hall, 1997.
- [13] A. Yariv, *Introduction to Optical Electronics*: CBS College Publishing, 1985.
- [14] "IEEE Standard on Piezoelectricity," *ANSI/IEEE Std 176-1987*, p. 0_1, 1988.

- [15] Y. Lu, Z. Y. Cheng, Y. Barad, and Q. M. Zhang, "Photoelastic effects in tetragonal $\text{Pb}(\text{Zn}_{1/3}\text{Nb}_{2/3})\text{O}_3\text{-PbTiO}_3$ single crystals near the morphotropic phase boundary," *Journal of Applied Physics*, vol. 89, pp. 5075-8, 2001.
- [16] Y. Lu, C. Zhong-Yang, P. Seung-Eek, L. Shi-Fang, and Z. Qiming, "Linear electro-optic effect of $0.88\text{Pb}(\text{Zn}_{1/3}\text{Nb}_{2/3})\text{O}_3\text{-}0.12\text{PbTiO}_3$ single crystal," *Japanese Journal of Applied Physics, Part 1 (Regular Papers, Short Notes & Review Papers)*, vol. 39, pp. 141-5, 2000.
- [17] Y. Shizhuo, W. Juntao, Z. Chun, and C. Luo, "Giant electro-optic effect of PMN-33%PT single crystals under proper AC electric field bias," in *Photorefractive Fiber and Crystal Devices: Materials, Optical Properties, and Applications IX, 3-4 Aug. 2003, USA, 2003*, pp. 280-9.
- [18] P. D. Lopath, P. Seung-Eek, K. K. Shung, and T. R. Shrout, "Single crystal $\text{Pb}(\text{Zn}_{1/3}\text{Nb}_{2/3})\text{O}_3/\text{PbTiO}_3$ (PZN/PT) in medical ultrasonic transducers," in *Ultrasonics Symposium, 1997. Proceedings., 1997 IEEE*, 1997, pp. 1643-1646 vol.2.
- [19] R. Zhang, W. Jiang, B. Jiang, and W. Cao, "Elastic, dielectric and piezoelectric coefficients domain engineered $0.70\text{Pb}(\text{Mg}_{1/3}\text{Nb}_{2/3})\text{O}_3\text{-}0.30\text{PbTiO}_3$ single crystal," *AIP Conference Proceedings*, pp. 188-97, 2002.
- [20] H. Cao, V. H. Schmidt, R. Zhang, W. Cao, and H. Luo, "Elastic, piezoelectric, and dielectric properties of $0.58\text{Pb}(\text{Mg}_{1/3}\text{Nb}_{2/3})\text{O}_3\text{-}0.42\text{PbTiO}_3$ single crystal," *Journal of Applied Physics*, vol. 96, pp. 549-554, 2004.
- [21] M. Chapman. (2002). *Heterodyne and homodyne interferometry*. Available: <http://www.olympus-controls.com/documents/GEN-NEW-0117.pdf>
- [22] E. M. Lawrence, K. E. Speller, and D. Yu, "MEMS characterization using Laser Doppler Vibrometry," pp. 51-62, 2003.
- [23] Polytec, "Theory Manual," in *Polytec VibSoft Software*, ed, 2012.
- [24] R. E. Newnham, *Properties of materials*. New York: Oxford University Press 2005.
- [25] W. Reeder, M. Mark, and G. Milton, "Acousto-Optic Scanners and Modulators," in *Handbook of Optical and Laser Scanning*, ed: CRC Press, 2004, pp. 599-663.
- [26] P. P. Banerjee, "Meta-acousto-optics: the interaction of light and sound in an acoustic negative index medium," San Diego, California, USA, 2010, pp. 77540R-7.
- [27] *Electronic archive: New Semiconductor Materials. Characteristics and Properties, GaP - Gallium Phosphide*. Available: <http://www.ioffe.rssi.ru/SVA/NSM/Semicond/GaP/basic.html>
- [28] "Comsol Multiphysics, Materials Database v4.3," in *Materials Database*, 4.3 ed, 2012.

- [29] S. Adachi, *Properties of Semiconductor Alloys: Group-IV, III-V and II-VI Semiconductors*: Wiley, 2009.
- [30] I. C. Chang, "I. Acoustooptic Devices and Applications," *Sonics and Ultrasonics, IEEE Transactions on*, vol. 23, pp. 2-21, 1976.
- [31] H. Sasaki, K. Tsubouchi, N. Chubachi, and N. Mikoshiba, "Photoelastic effect in piezoelectric semiconductor: ZnO," *Journal of Applied Physics*, vol. 47, pp. 2046-2049, 1976.
- [32] G. A. Coquin, D. A. Pinnow, and A. W. Warner, "Physical Properties of Lead Molybdate Relevant to Acousto-Optic Device Applications," *Journal of Applied Physics*, vol. 42, pp. 2162-2168, 1971.
- [33] A. W. Warner, M. Onoe, and G. A. Coquin, "Determination of Elastic and Piezoelectric Constants for Crystals in Class (3m)," *The Journal of the Acoustical Society of America*, vol. 42, pp. 1223-1231, 1967.
- [34] M. H. Manghnani, "Elastic Constants of Single-Crystal Rutile under Pressures to 7.5 Kilobars," *J. Geophys. Res.*, vol. 74, pp. 4317-4328, 1969.
- [35] T. B. Bateman, "Elastic Moduli of Single-Crystal Zinc Oxide," *Journal of Applied Physics*, vol. 33, pp. 3309-3312, 1962.
- [36] J. M. Farley, G. A. Saunders, and D. Y. Chung, "Elastic properties of scheelite structure molybdates and tungstates," *Journal of Physics C: Solid State Physics*, vol. 8, p. 780, 1975.
- [37] H. J. McSkimin, A. Jayaraman, and J. P. Andreatch, "Elastic Moduli of GaAs at Moderate Pressures and the Evaluation of Compression to 250 kbar," *Journal of Applied Physics*, vol. 38, pp. 2362-2364, 1967.
- [38] R. Weil and W. O. Groves, "The Elastic Constants of Gallium Phosphide," *Journal of Applied Physics*, vol. 39, pp. 4049-4051, 1968.
- [39] E. H. Bogardus, "Third-Order Elastic Constants of Ge, MgO, and Fused SiO₂," *Journal of Applied Physics*, vol. 36, pp. 2504-2513, 1965.
- [40] A. S. Andrushchak, Y. V. Bobitski, M. V. Kaidan, B. V. Tybinka, A. V. Kityk, and W. Schranz, "Spatial anisotropy of photoelastic and acoustooptic properties in β -BaB₂O₄ crystals," *Optical Materials*, vol. 27, pp. 619-624, 2004.
- [41] B. Mytsyk and N. Dem'yanyshyn, "Piezo-optic surfaces of lithium niobate crystals," *Crystallography Reports*, vol. 51, pp. 653-660, 2006.
- [42] *Acousto-Optic Physical Principles - Main Equations*. Available: <http://www.acoustooptic.com/>

- [43] H. Chuanyong, J. Taylor, L. Hongbo, A. Bhalla, and G. Ruyan, "Microwave electrooptic coefficient and modulation applications using ferroelectric single-crystal fibers," in *Photorefractive Fiber and Crystal Devices: Materials, Optical Properties, and Applications XII*, 16 Aug. 2006, USA, 2006, pp. 63140-1.
- [44] C. Huang, "Ferroelectric Single Crystal Fiber in High Frequency Electrooptic Modulation and Optical Frequency Shift," The Pennsylvania State University, 2006.
- [45] C. Huang, A. S. Bhalla, and R. Guo, "Measurement of microwave electro-optic coefficient in $\text{Sr}_{0.61}\text{Ba}_{0.39}\text{Nb}_2\text{O}_6$ crystal fiber," *Applied Physics Letters*, vol. 86, p. 211907, 2005.
- [46] C. o. N. Accessibility, Applicability, and N. R. Council, *Nanophotonics: Accessibility and Applicability*: The National Academies Press, 2008.
- [47] D. R. Smith, J. B. Pendry, and M. C. K. Wiltshire, "Metamaterials and Negative Refractive Index," *Science*, vol. 305, pp. 788-792, August 6, 2004 2004.
- [48] D. Rainwater, A. Kerkhoff, K. Melin, J. C. Soric, G. Moreno, and A. Alù, "Experimental verification of three-dimensional plasmonic cloaking in free-space," *New Journal of Physics*, vol. 14, p. 013054, 2012.
- [49] D. Schurig, J. J. Mock, B. J. Justice, S. A. Cummer, J. B. Pendry, A. F. Starr, and D. R. Smith, "Metamaterial Electromagnetic Cloak at Microwave Frequencies," *Science*, vol. 314, pp. 977-980, November 10, 2006 2006.
- [50] M. Miller and R. Guo, "Coupling Surface Plasmon Polaritons with Opto-Acoustics," R. McIntosh, Ed., ed, 2012.
- [51] Comsol. (2012). *SAW Gas Sensor*. Available: <http://www.comsol.com/showroom/gallery/2129/>
- [52] V. R. K. Murthy, *Methods of Measurement of Dielectric Constant and Loss in the Microwave frequency Region*: Springer-Verlag, 1994.
- [53] H. M. Altschuler, *Handbook of microwave measurements* vol. 2. Brooklyn, NY: Polytechnic Press, 1963.
- [54] S. Tomko, S. Agrawal, and A. S. Bhalla, "Loss & Dielectric Permittivity of Small Samples of Materials in the C Band of Microwave Frequencies" *NSF EE REU Penn State Annual Research Journal*, vol. III, pp. 151-166, 2005.
- [55] B. W. Hakki and P. D. Coleman, "A Dielectric Resonator Method of Measuring Inductive Capacities in the Millimeter Range," *Microwave Theory and Techniques, IRE Transactions on*, vol. 8, pp. 402-410, 1960.

- [56] M. Santra and K. U. Limaye, "Estimation of complex permittivity of arbitrary shape and size dielectric samples using cavity measurement technique at microwave frequencies," *Microwave Theory and Techniques, IEEE Transactions on*, vol. 53, pp. 718-722, 2005.
- [57] *Ceramic materials for electronics: processing, properties, and applications*: Marcel Dekker, Inc., 1986.
- [58] H. Nakai, Y. Kobayashi, and Z. Ma, "Wide-band measurements for frequency dependence of complex permittivity of a dielectric rod using multi-mode tm_{0m0} cavities," in *2008 Asia Pacific Microwave Conference, APMC 2008, December 16, 2008 - December 20, 2008*, Hong Kong, China, 2008.
- [59] C. L. Sciences. *Thermal Properties of Corning Glasses*. Available: <http://www.quartz.com/pxtherm.pdf>
- [60] R. G. Geyer and J. Krupka, "Microwave dielectric properties of anisotropic materials at cryogenic temperatures," *Instrumentation and Measurement, IEEE Transactions on*, vol. 44, pp. 329-331, 1995.
- [61] D. C. Dube, S. C. Mathur, S. J. Jang, and A. S. Bhalla, "Electrical behavior of diffused phase ferroelectrics in the microwave region," *Ferroelectrics*, vol. 102, pp. 151 - 154, 1990.
- [62] U. Bottger and G. Arlt, "Dielectric microwave dispersion in PZT ceramics," *Ferroelectrics*, vol. 127, pp. 95 - 100, 1992.

VITA

Robert McIntosh is originally from Lockport, NY. A graduate of Newfane High School in 2001, he went to The Pennsylvania College of Technology (a Penn State affiliate) and graduated in 2005 with a Minor in Mathematics, Associate degrees in Computer Automation Maintenance and Electrical Engineering Technology, and a Bachelors of Science in Electrical Engineering Technology. From 2005 through 2007 he worked as an Engineer on contract for Corning Incorporated in Corning, NY. While at Corning he was involved in several projects including research in non-contact ultrasound imaging, the design of laser control electronics for a synthetic green laser and several inspection systems for testing the modulus or rupture of ceramic filters and an optical image inspection system. In 2008 he started graduate work at The University of Texas at San Antonio and earned a Master's of Science in Electrical Engineering in 2012. He is currently a Graduate Research Assistant in Electrical Engineering with research interests in Optics, photonics, microwave testing, Finite Element modeling in the Multi-functional Electronic Materials and Devices Research Lab (MeMDRL). He is the author/coauthor of several technical papers and contributed in many international conferences.